3

# X-ray Absorption Near-Edge Structure (XANES) Spectroscopy

## Grant S. Henderson[1], Frank M.F. de Groot[2], Benjamin J.A. Moulton[1]

*[1]Department of Earth Sciences*
*University of Toronto*
*22 Russell St*
*Toronto, Ontario, M5S 3B1*
*Canada*

*henders@es.utoronto.ca*

*[2]Inorganic Chemistry and Catalysis Department of Chemistry*
*Utrecht University*
*Universiteitsweg 99, 3584 CG Utrecht, Netherlands*

*f.m.f.degroot@uu.nl*

## PREFACE

The previous *Reviews in Mineralogy* volume on spectroscopic methods (Vol. 18 *Spectroscopic Methods in Mineralogy and Geology*, Frank C. Hawthorne, ed. 1988), contained a single chapter on X-ray absorption spectroscopy which reviewed aspects of both EXAFS (Extended X-ray Absorption Fine Structure) and XANES (X-ray Absorption Near-Edge Structure) (Brown et al. 1988, Chapter 11) However, since publication of that review there have been considerable advances in our understanding of XANES theory and applications. Hence EXAFS and XANES have been separated into their own individual chapters in the current volume. In this chapter we endeavor to bring the reader up to date with regard to current XANES theories, as well as, introducing them to the common applications of the technique in mineralogy, geochemistry and materials science. There have been several reviews of XANES (cf., Brown et al. 1988, Brown and Parks 1989, Manceau et al. 2002, Brown and Sturchio 2002, Mottana 2004, Rehr and Ankudinov 2005, de Groot 2001, 2005, and papers therein). In this chapter on XANES it is not our intention to provide a comprehensive review of all the XANES studies since 1988 but to summarize what X-ray edges are commonly investigated and what one can expect to be able to extract from the data. The reader is also advised to read the chapters in this volume on analytical transmission electron microscopy by Brydson et al. (2014, this volume) where (core level) electron energy loss (EELS) spectroscopy is discussed, and by Lee et al. (2014, this volume) on X-ray Raman spectroscopy (XRS), as these techniques provide element specific information similar to XANES.

X-ray absorption near-edge structure (XANES) spectroscopy using synchrotron radiation is a well-established technique providing information on the electronic, structural and magnetic properties of matter. In XANES, a photon is absorbed and an electron is excited from a core state to an empty state. To excite an electron in a given core-level, the photon energy has to be equal or higher than the binding energy of this core-level. This gives rise to the opening of a new absorption channel when the photon energy is scanned. The energy of an absorption edge therefore corresponds to the core-level energy, which is characteristic for each element, making XANES an element-selective technique.

In addition to the XANES region, at higher energies the extended X-ray absorption fine structure (EXAFS) region is found. The spectral shape in the near-edge region is determined by electronic density of states effects and gives mainly information about the electronic properties and the local geometry of the absorbing atom. The EXAFS region is dominated by single scattering events of the outgoing electron on the neighboring atoms, providing mainly information about the local geometric structure around the absorbing site. In this chapter we will focus on XANES.

## INTRODUCTION

XANES is an important tool for the characterization of bulk minerals as well as for studies of mineral surfaces and adsorbents on mineral surfaces. The particular assets of XANES spectroscopy are its element specificity and the possibility to obtain detailed information in the absence of long range order. Below, it will be shown that the X-ray absorption spectrum in many cases is closely related to the density of unoccupied electronic states of a system. As such XANES is able to provide a detailed picture of the local electronic structure of the element studied.

### Interaction of X-rays with matter

In XANES, the changes in the absorption of X-rays due to the photoelectric effect is measured. The XANES spectrum is given by the absorption cross section μ. An X-ray photon acts on charged particles such as electrons. As X-ray passes an electron, its electric field pushes the electron first in one direction, then in the opposite direction, in other words the field oscillates in both direction and strength, allowing the electron to capture the energy. The Fermi Golden Rule states that the XANES intensity ($I_{XANES}$) for the transition from a system in its initial state $\Phi_i$ to a final state $\Phi_f$ is given by:

$$I_{XAXES} \propto \left| \left\langle \varepsilon \left| \hat{e}_q \cdot r \right| v \right\rangle \right|^2 \rho$$

where $\hat{e}_q \cdot r$ is the electric dipole operator. The quadrupole transition is more than 100 times smaller and often can be neglected. In the case of the pre-edge structures of the metal *K*-edges, the quadrupole transition is important because the 3*d* density of states is much larger than the 4*p* density of states and the quadrupole peaks appear in the pre-edge region where there is no 4*p* density of states.

### Binding energy

If an assembly of atoms is exposed to X-rays it will absorb some of the incoming photons. At a certain energy a sharp rise in the absorption will be observed. This sharp rise in absorption is called the absorption edge. The energy of the absorption edge is determined by the binding energy of a core level. Exactly at the edge, the photon energy is equal to the binding energy, or more precisely the edge identifies transitions from the ground state to the lowest electron-hole excited state.

The core hole binding energy is formally defined in relation to the core electron ionization energy, as is measured in an X-ray photoemission experiment. The ionization energy is the amount of energy required to remove an electron from an atom, as one would do in an X-ray photoemission spectroscopy (XPS) experiment (cf., Nesbitt and Bancroft 2014, this volume). In case of a solid, the ionization energy is corrected by the work function, the energy difference between the lowest empty state and the vacuum level. The core hole binding energies of all metals are tabulated in the X-ray data booklet (Thompson and Vaughan 2011). The XANES edge energy is not necessarily exactly the same as the core hole binding energy. The two processes are respectively:

$$\text{XPS: } \Psi_0 > \Psi_0\underline{c} + \varepsilon$$

$$\text{XAS: } \Psi_0 > \Psi_0\underline{c}v$$

In XPS the ground state ($\Psi_0$) is excited to the ground state plus a core hole ($\underline{c}$), where the electron ($\varepsilon$) is excited to higher energy, while in XAS the ground state is excited with a core-to-valence excitation ($\underline{c}v$). The XPS binding ($E_B$) is defined as the photon energy ($\Omega$) minus the measured kinetic energy of the electron ($E_k$) and corrected for the work function ($\phi$):

$$E_B = \Omega - E_k - \phi$$

The work function is the minimal energy to emit an electron from the material. In metals the XAS edge energy can be assumed to be equal to the XPS binding energy, because exactly at the XPS binding energy a transition is possible to the lowest empty state. Experimentally the XAS edge energy can be slightly higher than the XPS binding energy, for example if the transition to the lowest empty state is forbidden by selection rules.

**Single electron excitation approximation and selection rules**

In first approximation XANES can be described as the excitation of a core electron to an empty state. In the Fermi golden rule, the initial state wave function is rewritten as a core wave function and the final state wave function ($\varepsilon$) as a valence electron wave function ($v$). This implicitly assumes that all other electrons do not participate in the X-ray induced transition. In this approximation, the Fermi golden rule can be written as:

$$I_{XAXES} \propto \left| \left\langle \varepsilon \left| \hat{e}_q \cdot r \right| v \right\rangle \right|^2 \rho$$

The X-ray absorption selection rules determine that the dipole matrix element is non-zero if the orbital quantum number of the final state differs by one from the initial state ($\Delta L = \pm 1$, i.e., $s \rightarrow p$, $p \rightarrow s$ or $d$, etc.) and the spin is conserved ($\Delta S = 0$). In the dipole approximation, the shape of the absorption spectrum should look like the partial density of the ($\Delta L = \pm 1$) empty states projected on the absorbing site, convoluted with a Lorentzian. This Lorentzian broadening is due to the finite lifetime of the core-hole, leading to an uncertainty in its energy according to Heisenberg's principle. The single electron approximation gives an adequate simulation of the XANES spectral shape if the interactions between the electrons in the final state are relatively weak. This is the case for all excitations from $1s$ core states ($K$-edges).

**Calculations of XANES spectra**

The dominant method to calculate the density of states is Density Functional Theory (DFT) where either band structure, multiple scattering or chemical DFT codes can be used (cf., Jahn and Kowalski 2014, this volume). Programs to calculate the X-ray absorption spectral shape include FEFF, Wien2k, QuantumEspresso, ADF and ORCA. Depending on the specific method used one has to use a number of "technical" parameters such as the number of states used, the specific exchange-correlation potential and semi-empirical parameters such as the Hubbard U (the two-electron repulsion energy). An overview of the various software packages can be presently found at *http://www.xafs.org* but will move to *http://www.ixasportal.net/wiki/doku.php* shortly.

***Core hole effects and hole-electron excitations.*** Following the final state rule (von Barth and Grossmann 1982), one has to calculate the distribution of empty states in the final state of the absorption process. The final state includes a core hole on the absorbing site. The inclusion of the core hole introduces a significantly larger unit cell in case of reciprocal space calculations. In case of real-space calculations, the inclusion of a core hole is straightforward and only the potential of the central atom is modified. It has been shown for many examples that the inclusion of the core hole improves the agreement with experiment (Taillefumier et al. 2002). It is not well established if the inclusion of a fullcore hole gives the best description of

the XANES spectral shape. For example, one can use the exchange core hole (XCH) method, or methods that explicitly calculate the creation of hole-electron excitation such as Time-Dependent DFT (DeBeer-George et al. 2008).

***Multiplet effects.*** The core hole that is part of the XANES final state does not only have an influence on the potential, but the core state also has a wave function. In case of a $1s$ core state, this wave function can be neglected. In case of $2s$ and $3s$ wave functions the overlap is larger but the only effect that plays a role is the spin-up or spin-down character of the core hole. The spin-moment of the core hole interacts with the valence electrons (or holes) giving rise to an exchange splitting in $2s$ and $3s$ XANES. The same exchange interaction plays a role in $2s$ and $3s$ XPS spectra, which are more often studied than their XANES counterparts ($L_1$ and $M_1$ edges, Okada et al. 1994). Things become dramatically more complex in those cases where a core hole carries an orbital momentum. The core hole spin-orbit coupling that separates the $2p$ XANES spectra into their $2p_{3/2}$ ($L_3$) and $2p_{1/2}$ ($L_2$) parts. In addition, the $2p$ wave function can have significant overlap with the valence electrons. In case of $3d$-systems, the $2p3d$ electron-electron interactions are significant and significantly modify the spectral shape. The term "multiplet effect" is used to indicate this core-valence electron-electron interaction (de Groot 1994).

## EXPERIMENTAL ASPECTS OF XANES

### Doing a XANES experiment at a beamline

Prior to doing experiments one has to select an appropriate beamline at a suitable synchrotron radiation facility and it's a good idea to check on what costs will be involved should your experiments be allocated beamtime. Often facilities cover travel and living expenses for researchers, but not always. A proposal has to be written and submitted to the facility (online and by a set deadline) outlining the type of experiments that will be done, edges to be investigated, type of samples, energy resolution required and probable length of time to do the experiments (usually in terms of 8 hour shifts), as well as, any special requirements such as use of wet and dry labs, high pressure or temperature equipment, etc. These proposals are then peer reviewed and beamtime allocated based on competitive review of all the proposals requiring access to the experimental beamline and synchrotron radiation facility. If the experiments are approved it is allocated a set number of shifts for their experiment. Once at the beamline to run experiments, it is important to remember that they must be performed during the limited time allocated, so it is important to utilize all available time. This means that experiments will run 24 hours per day requiring more than a single person to be present (usually 2-3 people are required). Samples must be prioritized in case of problems with the X-ray beam since a variety of unexpected disruptions may occur, such as loss of the X-ray beam, computer glitches etc. that may reduce available experimental time. It is also advisable to have extra samples available to run in case the experiments go quicker and smoother than anticipated (not usually the case!).

For example, for Fe XANES with an edge energy of ~7110 eV, the beamline must be capable of collecting data over the appropriate energy range of interest (from ~20 eV before the edge to ~150 eV above the edge for a typical XANES experiment. The theoretical width of the peak responsible for the $1s$ state to higher energy states is ~1.5 eV (Krause and Oliver 1979) so that the beamline optics must ideally be sufficient to resolve features of this width, i.e., energy resolution should be at least 2 times better. In addition, the data need to be collected at a step size that will resolve subtle experimental features such as shoulders on the pre-edge peaks. Usually the step size in the pre-edge region is set at 0.1 or 0.2 eV and slightly larger step sizes (0.5 eV) across the edge itself with an even larger step size for the EXAFS region, 1.0 eV close to the edge and up to 5 eV at higher energies. The energy range must also be calibrated, for example using metallic reference foils. Furthermore, an internal standard should be used if experiments are going to be performed on the same samples and

edges at *different* beamlines as the energy position may change slightly from beamline to beamline due to different facility characteristics. In addition, for quantitative measurements of iron oxidation states a set of standards must be used with well-known oxidation states, preferably determined using another technique such as Mossbauer or wet chemical analysis, and the standards must have the Fe in somewhat similar matrices to those of the unknown samples. This means that for quantitative Fe redox measurements on glasses, glass standards should be used while for minerals mineral standards should be used (cf., e.g., Galoisy et al. 2001; Berry et al. 2003a; Wilke et al. 2005; Cottrell et al. 2009). Finally it is important that the experimental conditions from one experimental run to another be the same, which means that a quick energy calibration should be run periodically throughout experimental runs, as well as, immediately after restoration of the beam following any beam disruption such as a beam dump. Depending upon the resolution, signal-to-noise and time required to collect a spectrum, multiple spectra (usually 2 or 3) are collected on the same sample and averaged. It is also important to check that the sample is not being affected by the beam (beam damage) so some time should be allocated to collecting spectra with and without moving the position of the beam on the sample. This is particularly important for redox studies where the beam itself may change the redox state of the sample.

**Data reduction**

Once the data have been collected and individual spectra checked for "glitches," such as random spikes in the data which must be removed, the data need to be reduced to a suitable form for analysis and interpretation. XANES data reduction is relatively simple and may be done with a variety of available software. Data reduction steps include possible correction for self-absorption effects, removal of a pre-edge background (usually a linear fit or a Victoreen polynomial) and normalization of the edge jump to one.

In some publications the background continuum is removed from the XANES spectrum. Background continuum removal is important for EXAFS analysis, but for XANES analysis it is not obvious what advantage is gained from such continuum removal. In fact, theoretical XANES simulations based on DFT calculate the whole XANES spectral shape including the background continuum. The background continuum is removed using some sort of arctan or error function but correction that has been widely used since the late 80's is an arctan function (cf., Poe et al. 2004; Höche et al. 2011). An example of an arctan fit from Wilke et al. (2001) is shown in Figure 1. Outka and Stohr (1988) note that there are several different types of continuum steps that can be observed and it is important to account for the step if the spectra are going to be modeled using some sort of fitting of the peaks by Gaussian, Lorentzian or pseudo-Voigt peak profiles. Unfortunately, the placement and width of the background subtraction functions is not well defined. Outka and Stohr's (1988) prefer an error function because the width of the function is related to a known parameter; the instrumental resolution, while the width of the arctan is related to the life time of the excited state which may not be known. As to the position of the step, Outka and Stohr (1988) suggest it should be placed 1 to several eV below the core level ionization energy. Regardless of how the continuum step is modeled it is important that all the experimental data be treated in a consistent manner with background removal fully described and justified.

Prior to analysis and interpretation of the pre-edge features one further correction needs to be applied. The background of the edge under the pre-edge features needs to be removed and this is done by fitting a polynomial such as a spline function that smoothly reproduces the slope of the data prior to the pre-edge and immediately following the pre-edge peaks. For extracting the pre-edge the background may also be described by the tail of a Gaussian or Lorentzian function (cf., Farges et al. 2004). One example for background removal by a spline function is shown in the inset in Figure 1. The data are now ready to be analyzed and interpreted.
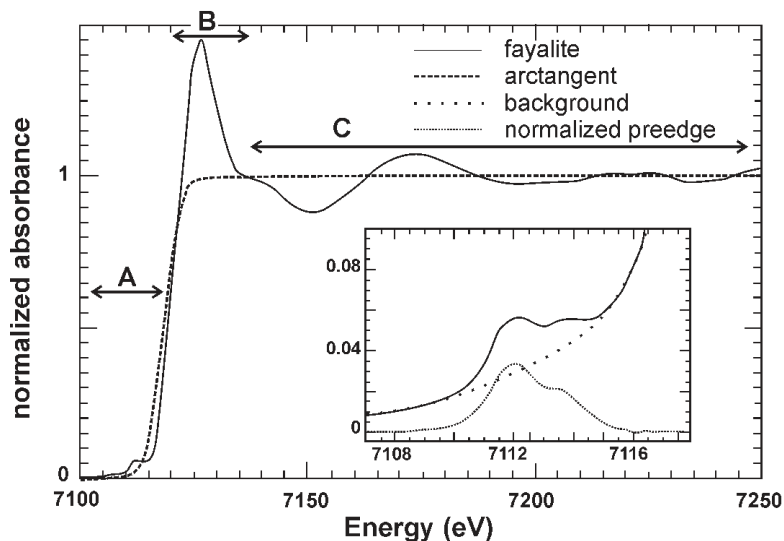
**Figure 1**. The arctan function and normalization of the pre-edge. The inset shows the background fit for the pre-edge region (after Wilke et al. 2001). The pre-edge (A), edge (B) and post-edge (C) regions are indicated. The inset shows the background removal under the pre-edge features.

## XANES DETECTION MODES

### Transmission detection of XANES

A XANES spectrum originates from the fact that the probability of an electron to be ejected from a core level is dependent on the energy of the incoming beam. For this reason the energy of the X-rays is scanned during an experiment. The X-ray interacts with the sample of interest and the intensity after the sample is measured. An important factor of transmission detection is the requirement for a homogeneous sample. Variations in the thickness or pinholes are reasons for the so-called thickness effect that can significantly affect the spectral shape by introducing a non-linear response (Schroeder et al. 1996). Transmission experiments are standard for hard X-rays, but due to the attenuation length of less than one micron, soft X-ray XANES is usually not measured in transmission mode, except in the case of Transmission X-ray Microscopy (TXM) beamlines (de Smit et al. 2008).

### Electron yield detection of XANES

The decay of the core hole gives rise to an avalanche of electrons, photons and ions escaping from the surface of the substrate. By measuring any of these decay products, it is possible to measure samples of arbitrary thickness. An important prerequisite for the use of decay channels is that the channels that are measured are linearly proportional to the absorption cross section. With the total electron yield method, one detects all electrons that emerge from the sample surface, independent of their energy. One can detect the current that flows to the sample or detect the emitted electrons. The interaction of electrons with solids is much larger than the interaction of X-rays with solids. This implies that the electrons that escape from the sample must originate close to the surface. The probing depth of total electron yield (TEY) lies in the range between approximately 1 to 10 nm, depending on the edge strength and the material studied. A quantitative study on the oxygen *K*-edge determined an electron escape depth of 1.9 nm (Abbate et al. 1992).

**Fluorescence yield detection of XANES**

The fluorescence decay of the core hole can be used as the basis for the absorption measurement. The amount of fluorescent decay increases with energy and dominates over Auger decay for hard X-ray experiments. The photon created in the fluorescent decay has a mean free path of the same order of magnitude as the incoming X-ray, which implies that there will be saturation effects if the sample is not dilute. For materials dilute in the studied element the background absorption $\mu_B$ dominates the absorption at the specific edge and the measured fluorescence intensity (also known as fluorescence yield (FY)) is proportional to the absorption coefficient. For less dilute materials the spectral shape is modified and the highest peaks will appear compressed with respect to the lower peaks, an effect known as self-absorption or saturation. In case of the *L*-edges of transition metal compounds and the *M*-edges of rare earths the fluorescence decay is strongly energy dependent, which implies that for those systems FY detection is not directly proportional to the X-ray absorption spectral shape (de Groot 2012).

**Partial Fluorescence Yield detection of XANES**

Recently, a range of partial fluorescence yield methods have been developed. We briefly discuss two important approaches, respectively inverse partial fluorescence yield (IPFY) and high-energy fluorescence detection (HERFD). IPFY measured the integrated fluorescence of an element in the system other than the edge element that is measured. It can be shown that such an approach effectively yields a fluorescence yield spectrum that is effectively not sensitive to saturation effects (Achkar et al. 2011). HERFD uses a high-resolution fluorescence detector to scan through a XANES spectrum. HERFD-XANES measurements are often performed in connection to resonant inelastic X-ray scattering (RIXS) experiments and relate to a constant-emission-energy cross-section through the RIXS plane. Furthermore, by extracting the constant-incident cross-section at the position *K*-edge pre-edge *L*-edge or *M*-edge-like spectra may be recorded (Caliebe et al. 1998; Glatzel and Bergmann 2005). For systems where multiplet effects are important, the HERFD-XANES can be modified from the XANES spectral shape (Suljoti et al. 2009). Hämäläinen et al. (1991) showed that HERFD-XANES effectively removes the lifetime broadening. This largely enhances the accuracy in the determination of the pre-edge spectral shapes and their intensities. HERFD detection also allows the detection of XANES spectra that are selective to the valence, spin-state or site symmetry (de Groot 2001; Glatzel and Bergmann 2005). One can tune the energy of the fluorescence detector to the peak position of one valence and vary the energy of the incoming X-ray, thereby measuring the X-ray absorption spectrum of that particular valence.

**Electron energy loss spectroscopy and X-ray Raman**

It can be shown that electron energy loss spectroscopy (EELS) as detected in an electron microscope can measure exactly the same spectral shape as XANES. This is the case under the assumptions that the primary electron energy is higher than a few thousand eV and that the scattering angle is small. Details on EELS spectroscopy are discussed in the chapter by Brydson et al. (2014, this volume).

X-ray Raman spectroscopy is the X-ray analog of optical and UV Raman. A hard X-ray, typically with an energy of about 10.000 eV impinges on the sample and the scattered radiation is measured at an energy lower than 10.000 eV. Like normal Raman one can study vibrational excitations (meV range) and electronic excitations (eV range). In addition, one can study core electron excitations that relate to energy losses of several hundred eV. Note that such core level X-ray Raman could also be named X-ray energy loss spectroscopy (XELS) and as such is the direct X-ray analog of electron energy loss spectroscopy (EELS). As is the case for EELS, the core excitation spectra from X-ray Raman spectroscopy can be described in analogy with XANES under the assumption of small scattering moments. X-ray Raman has a great potential for *in situ* measurements and it presents a hard X-ray alternative to conventional XANES

experiments in the study of systems with light elements, including Li, B, C, N and O (Lee et al. 2014, this volume).

## XANES microscopy

XANES experiments can be performed with X-ray microscopes. A number of transmission X-ray microscopes (TXM) or scanning transmission X-ray microscopes (STXM) exist for the soft X-ray range and the hard X-ray range. Typical resolutions that can be obtained are of the order of 20 nm. We refer to dedicated reviews for more details on the characteristics of the X-ray optics, etc. In the present review we assume that the TXM microscopes essentially allow doing XANES spectroscopy with 20 nm spatial resolution. If the sample is rotated in the beam the extension to XANES tomography is straightforward (Gonzalez-Jimenez et al. 2012).

## XANES ANALYSIS OF METAL *K*-EDGES

An important set of environmental and mineralogical studies involve the $1s$ X-ray absorption spectra (*K*-edges) of the $3d$-metals. We will discuss respectively the shape, the energy position and the white line intensity of the $1s$ XANES spectra. The $1s$ edges of the $3d$ transition metals have energies ranging from about 4 to 9 KeV. Cabaret and co-workers have carried out DFT calculations for $TiO_2$ (Cabaret et al. 1999). The complete spectral shape of $TiO_2$ is reproduced and it can be concluded that the $1s$ XANES of $3d$ transition metals does correspond to the metal $p$-projected density of state. In addition, the pre-edge region is found to be an addition of dipole and quadrupole transitions.

In many mineralogical applications, the systems studied are not exactly known. The metal $1s$ edges do show fine structure and edge shifts that can be used without the explicit calculation of the density of states. For example, the $Fe^{3+}$ edges are shifted to higher energy with respect to the $Fe^{2+}$ edges. The shift to higher energies with higher valence is a general phenomenon that can be used to determine the valence of $3d$ transition metals in unknown systems.

## Special energy positions of X-ray absorption edges

We will define the following special energy positions in the XANES edge structure:

- The X-ray absorption edge ($E_{edge}$)
- The pre-edge energy ($E_{pre}$)
- The transition with the lowest excitation energy ($E_B$)
- The energy where the escaping electron would have exactly zero energy ($E_0$)

In case of the *K*-edges of transition metal systems, it is not a trivial task to determine the energy position of a XANES edge $E_{edge}$. There are, at least, three different methods to define the energy of the edge: (a) the inflection point, (b) the energy where the intensity is 50% of the edge maximum and (c) the average of the energies at 20% and 80% of the edge maximum. The inflection point can be accurately determined from the maximum of the first derivative. In case of a single, non-structured edge the methods (a) to (c) all find exactly the same energy. The situation becomes more complicated with a spectrum for which a clear shoulder is visible on the leading edge. For example, iron metal has an edge on which a clear shoulder is visible. The inflection point might lose its value in such a case and, in fact, there can be two inflection points. In our opinion there is no clear criterion to decide which procedure should be followed. Much depends on the spectral details of the observed spectra. The best procedure would perhaps be the use of two or three methods for the edge determination. In case of many $3d$-transition metal systems, a clear pre-edge is visible due to transitions to $3d$-states. The pre-edge energy ($E_{pre}$), defined as the first maximum of the pre-edge can also be used as an experimental indicator.

We define the transition with the lowest energy as the binding energy, noting that this energy is not necessarily the same as in XPS as discussed above. Within a ground state calculation, the lowest unoccupied state is determined by the Fermi level can be determined from the comparison with a simulation of the XANES spectral shape. However, if the final state rule is used, the extra core hole potential can shift the edge excitation energy to lower energy, losing its direct relation to the ground state Fermi level. In X-ray photoemission experiments, $E_0$ is defined as the vacuum level, i.e., the energy at which the electron would have zero kinetic energy. The energy difference between $E_F$ and $E_0$ is the work function.

Despite the variety of special edge energies including several procedures to determine them, the use of consistent procedures to determine energy positions can lead to clear trends, for example a relation between edge energies and the formal valence of the system. An example is the determination of the pre-edge energies and the edge energies of a series of vanadium oxides by Wong et al. (1984). They find a linear relation between the edge position and the formal oxidation state. In addition, a linear relation was found between the pre-edge energy and the formal oxidation state. The slope of the pre-edge and edge energies is different, respectively about 2 eV/valence for the edge energy and 0.6 eV/valence for the pre-edge energy. This also implies that the energy difference between the pre-edge position and the edge position is linear with the formal oxidation state.

An interesting issue relates to the relative energy position of the edge and pre-edge peak position of octahedral and tetrahedral sites. In the case of iron coordination compounds, equivalent energy positions are found (Westre et al. 1997) whereas for example in the case titanium, copper and aluminum a systematic shift is observed with the tetrahedral peak shifted by approximately 1 eV in the case of copper (Yamamoto et al. 2002).

## The pre-edge region

The pre-edge region is related to transitions from the $1s$ core state to the $3d$-bands. Both direct $1s3d$-quadrupole transitions and dipole transitions to $4p$-character hybridized with the $3d$-band are possible. For the quadrupole transitions the matrix elements are less than 1% of the dipole transition, but on the other hand the amount of $3d$-character is by far larger than the $p$-character. This can make, depending on the particular system, the contributions of quadrupole and dipole transitions equivalent in intensity in the pre-edge region.

*The pre-edge structures in systems with isolated metal ions.* First we discuss the pre-edge spectra in systems with isolated metal ions in coordination compounds. The general model to interpret these pre-edges is to consider them as quadrupole transitions into empty $3d$-states. Quadrupole transitions have intrinsic transition strengths of approximately 0.1% of the dipole transitions, but because of the high density of states for the $3d$-band they are visible as small peaks with ~1 to 3% intensity in most, octahedral, transition metal systems. If inversion symmetry is broken, for example in tetrahedral complexes, the metal $3d$ and $4p$ states mix and there are direct dipole transitions into the $4p$-character of the $3d$-band.

The position and number of peaks are sensitive to the oxidation state and coordination of Fe. Their energy separation corresponds to the bound state spectroscopic levels of a Z+1 ion (cf., Westre et al. 1997). Because the $1s$ core hole has no effect on the relative energy positions, the $3d^5$ $Fe^{3+}$ spectra can be modeled using the ground state orbital configuration of $3d^6$ (Schulman et al. 1976; Calas and Petiau 1983). This is because the core hole generated by the promotion of the excited electron to the $3d$ orbitals, is close enough to the nucleus (Z) that the outer orbitals see a configuration similar to the next highest atom on the periodic table (Z+1) (cf., Sutton et al. 2000). Consequently, the pre-edge features can thus be interpreted using ligand field theory or charge transfer multiplet theory (cf., de Groot 2005; de Groot and Kotani 2008). Octahedral complexes only have quadrupole transitions and these transitions can be simulated from $3d^N$ to $1s^13d^{N+1}$ multiplet calculations. This approach has been used by Westre et al. (1997) to explain the pre-edge structures in iron coordination compounds.

Tetrahedral transition metal complexes, or in general systems where inversion symmetry is broken, have dipole-quadrupole mixing (Westre et al. 1997; DeBeer-George et al. 2005). In the case of tetrahedral symmetry, the local dipole-quadrupole mixing *only* involves the $t_2$-states, not the *e*-states. Because inversion symmetry is broken, the metal 3*d* and metal 4*p* states mix with each other and form a set of combined 3*d*+4*p* symmetry states. As such, the dipole (D) and quadrupole (Q) transitions reach the same final states, and their peaks are visible at the same energy.

***The pre-edge structures in systems with ligand-bridged metal ions.*** In case of oxides with oxygen-bridged metal ions the spectral situation is more complex. In addition to the local effects, there can be effects due to non-local transitions, as has been shown for the case of $TiO_2$ (Cabaret et al. 1999). The case of $TiO_2$ is described in detail in the next section. An example of non-local pre-edge structure can be found in the cobalt *K*-edge XANES of $LiCoO_2$. Figure 2 shows the normal *K*-edge XANES spectrum in comparison with the HERFD XANES. The peak at 7718 eV is related to the main edge, in other words to the dipole transitions to the 4*p* band. The 1*s* XANES spectrum of $LiCoO_2$ contains two clearly observable pre-edges A and B. $LiCoO_2$ is a non-magnetic (S = 0) low-spin oxide and its ground state has a filled $t_{2g}$ band and an empty $e_g$ band. This implies the presence of a



**Figure 2.** Comparison between XAS spectra recorded at the Co *K* edge using total fluorescence yield (dashed line) and using HERFD XANES (solid line).

single 1*s*3*d* quadrupole peak, which seems in contrast with the two peaks in experiment. Detailed angular dependent experiments showed that the first peak (A) at 7709 eV has quadrupole nature and the second peak (B) at 7711 eV has dipole character (Vankó et al. 2008). This second pre-edge peak of dipole character is absent in low-spin Co(III) complexes such as the Co(acac)$_3$ complex. Both systems are low-spin trivalent cobalt systems, where Co$^{III}$(acac)$_3$ has isolated Co ions, while in $LiCoO_2$ there are oxygen mediated Co-Co interactions. These observations confirm that the first peak is the local 1*s*3*d* quadrupole transition, while the second peak is a dipole 1*s*4*p* transition to the 4*p* character of the 3*d*-band. These non-local pre-edge transitions have been observed for the cobalt oxides (Vankó et al. 2008), $TiO_2$ (Cabaret et al. 1999; Shirley 2004; Uozumi et al. 1992), iron oxides (Caliebe et al. 1998; Glatzel et al. 2008) and $MnO_2$ (Farges 2005). Shukla et al. (2006) observed very small non-local transitions, alternatively called off-site transitions, in $La_2CuO_4$.

## The edge region and peaks at higher energies in the XANES region

In addition to the edge shift discussed above, the shape of the edge region can be interpreted in relation to reference compounds, for example the XANES edge structure of a metal in oxides. Some studies interpret spectral features at higher energies. A well-known example is the use of the $1/R^2$ rule, which relates the energy of a peak in the XANES with the distance $R$ between the absorbing atom and its neighbors. This rule effectively uses electron scattering, similar as used in the EXAFS region of the spectrum. The scattering vector $k$ is proportional to $\sqrt{E_k}$. In the chapter on EXAFS it is shown that within the single scattering approximation the distance $R$ is inversely proportional to the scattering vector $k$, yielding as a result the $1/R^2$ rule. The $1/R^2$ rule has been applied successfully for the determination of bond lengths in (adsorbed) small molecules (Stohr 1992) and melts (Wilke et al. 2007).
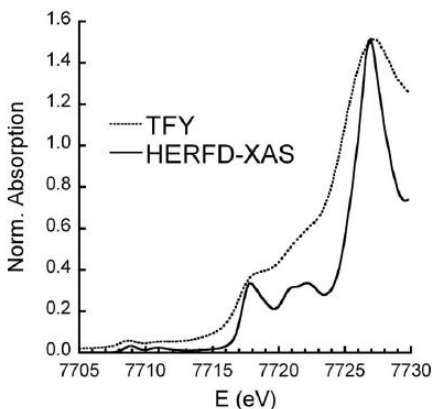
### XANES analysis of metal *L*-edges

The metal *L*-edges of the 3*d* transition metals are dominated by multiplet effects as described in the introduction. We will first briefly explain multiplet theory and multiplet analysis. For more details we refer to dedicated reviews on the calculations of *L*-edge spectra (de Groot 1994, 2001). In this review we focus on the consequences for practical *L*-edge analysis applied to minerals. The multiplet effects are too large to make any sensible connection to the empty density of states, as is possible for the *K*-edges. However the *L*-edges can be analyzed without theoretical simulations, focusing on respectively the spectral shifts, the integrated intensity, the branching ratio and XMCD experiments for improved site symmetry analysis.

### Multiplet analysis of *L*-edges

*L*-edges to transition metal compounds with partly filled 3*d* states are dominated by transitions to the empty 3*d* states. In first approximation the transition to the 4*s* states and higher states are neglected. They can be subtracted from the experimental spectra by an edge jump subtraction procedure (Wasinger et al. 2003). We approximate the ground state as $3d^N$ and the final state as $2p^5 3d^{N+1}$. A description of the *L*-edge needs the following interactions for the ground state and the final state:

1. An adequate description of the chemical bonds for molecules and band structure for solids, which can be approximated with model Hamiltonians, for example crystal field theory or charge transfer theory.

2. The intra-atomic 3*d*3*d* multipole interactions described with the $F^2$ and $F^4$ Slater integrals that can be reformulated as the Racah B and C parameters.

3. The 3*d* spin-orbit coupling

4. The core hole spin-orbit coupling, yielding a distinction between the $L_3$ and $L_2$ edge.

5. The core hole potential.

6. The core-valence exchange interaction, the direct spin-spin coupling of the core spin and the valence spins, within the multiplet model described with the G1 Slater integral.

7. The higher order term of the core-valence exchange interaction described with the G3 Slater integral.

8. The core hole – valence hole multipole interactions. The 2*p* and 3*p* core holes have a dipole-dipole interaction with the 3*d* holes, described with the $F^2$ Slater integral.

The basis for the crystal-field multiplet and charge-transfer multiplet calculations is the observation that the *L*-edges of many transition metal systems yield quasi-atomic spectra that can be described well with the atomic $3d^N$ to $2p^5 3d^{N+1}$ transition, where all other effects are included into an effective electric field. This implies that the translation symmetry is neglected and the hybridization described with an effective field. The local electron-electron interactions and the 3*d* spin-orbit coupling are treated explicitly. All final state effects of the 2*p* core hole are treated explicitly, including the core hole spin-orbit coupling and the atomic multiplet interactions. They are calculated for an isolated atom or ion and transferred to a molecule or solid. The charge-transfer multiplet (CTM) model has been initially developed by Theo Thole, partly in collaboration with Kozo Okada, Hirohiko Ogasawara, Akio Kotani, Gerrit van der Laan and George Sawatzky (Thole et al. 1988). The program of Theo Thole, modified by Hirohiko Ogasawara, has been incorporated into a user friendly interface CTM4XAS that can calculate the XAS, XPS, XES and RIXS spectra of transition metal systems and rare earths (Stavitski and de Groot 2010).

## QUALITATIVE SPECTRAL ANALYSIS OF THE *L*-EDGES

### Energy shifts

It turns out that the *L*-edge also shifts in energy with valence (cf., Nesbitt and Bancroft 2014, this volume). The shift is approximately 1.5 eV per formal valence change, as determined empirically for a number of elements. Because the *L*-edge spectral shape is a multi-peaked complex structure, it is difficult to assign an energy to a particular peak position. Instead it is more customary to determine the center of gravity of the complete *L*-edge. A complicating issue is the edge jump due to continuum states that should be subtracted.

### Intensities of the *L*-edges

According to the optical sum rule of a $2p$ to $3d$ transition, the integrated intensity of the *L*-edge yields the number of empty $3d$ states. To derive this value it is important to normalize the experimental spectrum to the edge jump and to subtract the edge jump from the experimental spectrum. Because *L*-edges are often measured with electron yield or fluorescence yield, without normalization to the edge jump, no significant number can be determined.

### The branching ratio

An experimental parameter that has been often analyzed is the branching ratio, the intensity ratio between the $L_3$ and the $L_2$ edge. The advantage is that this number can be determined without normalization to the edge jump but in order to obtain a reliable number the edge jumps must be subtracted. The branching ratio is sensitive to the ground state symmetry, especially its spin state. This makes the branching ratio also sensitive to the valence (Thole and van der Laan 1988).

### Polarization dependence and XMCD

Spectral analysis can be refined if polarization dependent spectra can be measured. Linear polarization needs an ordered system, for example a crystal with tetragonal symmetry. Systems that are ferro(i)magnetic or paramagnetic systems that can be magnetized can be measured with X-ray circular magnetic dichroism (XMCD). For example XMCD can be used to determine the relative site and valence occupations of mixed spinel systems, as is discussed below.

## XANES ANALYSIS OF LIGAND *K*-EDGES

The *K*-edges of the ligands binding to the metal can be calculated with DFT calculations. In case of ligand *K*-edges the comparison with DFT calculations is often very good. The most important experimental parameter that can be determined without calculations is the edge-normalized intensity of the $3d$-band. The integrated intensity of the peaks that overlap with $3d$ states yields the amount of ligand character in the $3d$-band. In other words this yields the ligand-$p$ – metal-$d$ covalency (Hedman et al. 1990). Another parameter is the position of the first peak. While the metal edges shift to higher energy with the metal valence, the ligand edges shift to lower energy with increased metal valence, essentially because it costs less energy to extract a core electron from a more negatively charged ion.

## APPLICATIONS OF XANES IN MINERALOGY AND GEOCHEMISTRY

### Transition metals: *K*-edges

By far the most common application of XANES in Earth sciences has traditionally been in investigating the oxidation state and coordination environment of transition metals, particularly iron (Fe), in minerals and amorphous materials such as glasses and melts. Below we focus on the transition metals that have been most commonly studied in recent years. While

they by no means represent the full range of transition metals that have been investigated, many of the comments, pitfalls and experimental requirements outlined, are applicable to any transition metal *K*-edge XANES study. We use iron as the main example.

***Iron – pre-edge and edge features.*** Iron is one of the most geologically important elements as it is the most abundant element found within the crust (Earth!) that exhibits different oxidation and coordination states in minerals and in magmas. Its coordination and redox state can strongly influence the physical and chemical behavior of magmas. An important method for accurately determining the reduced ($Fe^{2+}$)-to-oxidized ($Fe^{3+}$) ratio or $Fe^{3+}/Fe_{total}$ within minerals and solid materials is by Mössbauer spectroscopy. However, Mossbauer spectroscopy lacks the sensitivity required for samples with small amounts of iron (<1 wt%). The Fe *K*-edge, measured in fluorescence yield mode, is sensitive to small amounts of iron because hard X-rays measure a bulk signal. It is usually collected from ~7100 eV to ~7300 eV[1] but features beyond ~7150 eV are related to the EXAFS and are not considered here.

As discussed above, the *K*-edge XANES consists of a pre-edge region, a main peak characteristic of the edge jump and secondary features beyond the main edge peak. While the main peak and higher energy features may be of use in comparing unknown Fe *K*-edge XANES spectra with spectra from known mineral or glass standards; the so called "fingerprinting" technique, it is relatively unused for determining coordination and oxidation states of Fe in minerals and amorphous materials. As discussed above in "XANES analysis of metal *L*-edges," the main TM *K*-edge peaks shift to higher energy with increasing oxidation state (e.g., Schulman et al. 1976; Berry et al. 2003a), in the case of iron by ~5 eV but the principle features used for determining oxidation state and coordination are the pre-edge features.

As described above, the pre-edge peaks are due to $1s \rightarrow 3d$ transitions. In a non-centrosymmetric site (i.e., tetrahedral) the peak intensity is increased due to electric dipole contributions as a result of mixing of the $3d$ with $4p$ orbitals. Consequently, the intensity of the peaks increases with decreasing coordination due to the loss of inversion symmetry (Westre et al. 1997). Extracting quantitative numbers for oxidation state and coordination environment requires fitting of the peaks with either Gaussian or pseudo-Voigt peak profiles (Fig. 3) (Hawthorne and Waychunas 1988) give a discussion of peak fitting methods) and determination of the centroid of the fitted peaks. The centroid is the area weighted average of the position of the component used in the fit. The number of peaks fit, their positions and intensities varies depending upon whether there is $Fe^{2+}$ and/or $Fe^{3+}$ and whether *the different* Fe oxidation states are in 4-fold (tetrahedral, [4]Fe), 6-fold (octahedral, [6]Fe), 5-fold (square pyramid or trigonal bipyramid, [5]Fe) or higher coordination.

In minerals with no mixing of $Fe^{2+}$ and $Fe^{3+}$, $Fe^{2+}$ in tetrahedral coordination exhibits 2 pre-edge features at ~7111 eV and ~7113 eV. However, four peaks are predicted by theory (Westre et al. 1997; Arrio et al. 2000). When in octahedral coordination, three features are observed in experimental spectra although site distortion may reduce the intensity of the third peak (Wilke et al. 2001) and three peaks are predicted by theoretical calculations (Westre et al. 1997; Arrio et al. 2000). When $Fe^{2+}$ is in 5-fold coordination two peaks are observed in the experimental spectrum, similar to when in tetrahedral coordination and 3 peaks predicted by theory. Finally when in 8-fold coordination, two maxima are observed in the pre-edge region.

Tetrahedral $Fe^{3+}$ has one pre-edge peak with a centroid at 7113.5 eV. There are two peaks predicted but the second peak intensity is too low to be resolved in the experimental data. Five coordinated $Fe^{3+}$ also exhibits a single peak when in trigonal bipyramidal coordination

---

1 Note throughout the following sections the energy range shown is the region over which the spectra are normally collected. For the precise edge energy the reader should consult the X-ray data booklet compiled by Thompson and Vaughan (2011) which can be downloaded from http://xdb.lbl.gov.
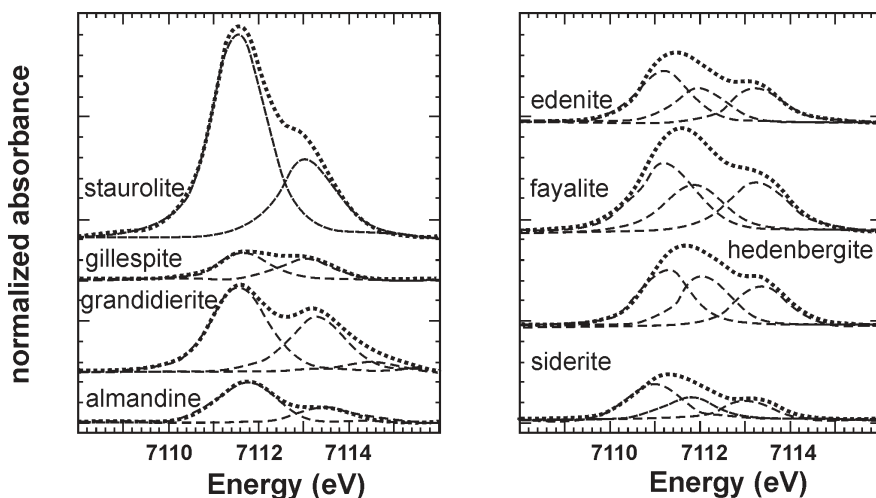
**Figure 3**. Examples of curve fits for mineral phases containing $Fe^{2+}$ and $Fe^{3+}$ (after Wilke et al. 2001).

and two peaks when in a square pyramid configuration (2 predicted). Farges (2001) has investigated a number of grandidierites where $Fe^{2+}$ is located in a trigonal bipyramid site. The spectra exhibit two pre-edge peaks due to $Fe^{2+}$ at ~7111.7 eV and minor $Fe^{3+}$ at ~7113.3, respectively. The most intense pre-edge peak, due to $Fe^{2+}$ in the trigonal bipyramid site, has a centroid at ~$7112 \pm 0.05$ eV. $^{[6]}Fe^{3+}$ compounds have two components whose centroids are at 7112.8 eV and 7114.3 eV, in agreement with theoretical predictions (Westre et al. 1997; Arrio et al. 2000).

*Iron – presence of both oxidation states.* In mineral phases that contain both oxidation states, analysis and interpretation of the pre-edge becomes more problematic. One approach is to use a linear combination of different spectra (see below). In this approach one attempts to match the experimental spectrum by summing different percentages of standard spectra of phases containing only $Fe^{2+}$ or $Fe^{3+}$ (Fig. 4).

The centroid position is an excellent measure of oxidation state of Fe when a material is composed solely of either ferrous or ferric iron, an $Fe^{2+}$ pre-edge can be observed at a centroid position of 7112 eV and for $Fe^{3+}$ 1.5 eV higher in energy at 7113.5 eV (cf., Wilke et al. 2001, 2004, 2005, 2009). Note that the edge itself is shifted ~5 eV higher in energy for $Fe^{3+}$ versus $Fe^{2+}$. For a given coordination state there is a linear response between centroid position and integrated pre-edge intensity. However, when there are mixtures of geometries, site distortion, and oxidation state, the response becomes non-linear (Wilke et al. 2001). Figure 5 plots the integrated pre-edge intensity versus centroid position for binary mixtures of $Fe^{2+}$ and $Fe^{3+}$ in different coordination states and clearly shows non-linear behavior between the two different oxidation states. Analysis of the pre-edge feature then requires some careful thought with regard to the intensity of the main peak, its shoulders, if any, as well as the relative intensities of the pre-edge features.

*Titanium.* Titanium *K*-edge XANES (~4900-5000 eV) has been primarily used to investigate the coordination state of Ti in glasses and melts (cf., Greegor et al. 1983; Yarker et al. 1986). However, regardless of the material being studied it is the pre-edge features, like that of Fe, that are used to determine the coordination environment of Ti. The pre-edge features are again due to quadrupole $1s \rightarrow 3d$ transitions similar to the Fe *K*-edge above (cf., Fig. 1) (Grunes 1983; Waychunas 1987; Uozumi et al. 1992). In the case of Ti, however, we do not
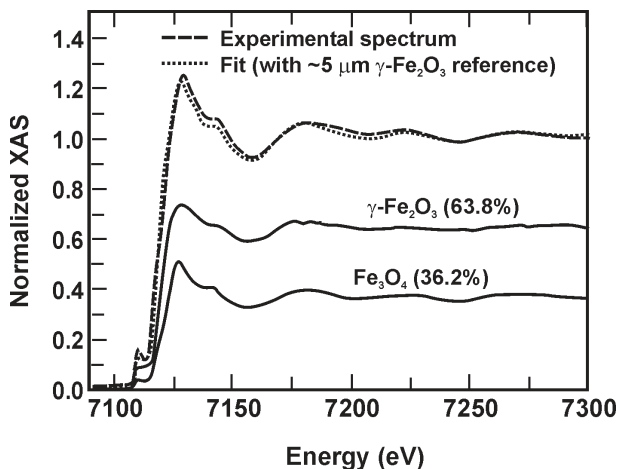
**Figure 4**. Fit of experimental spectrum of iron oxide nanoparticles by a linear combination of the spectra of maghemite ($\gamma$-Fe$_2$O$_3$) and magnetite (Fe$_3$O$_4$) (after Espinosa et al. 2012).
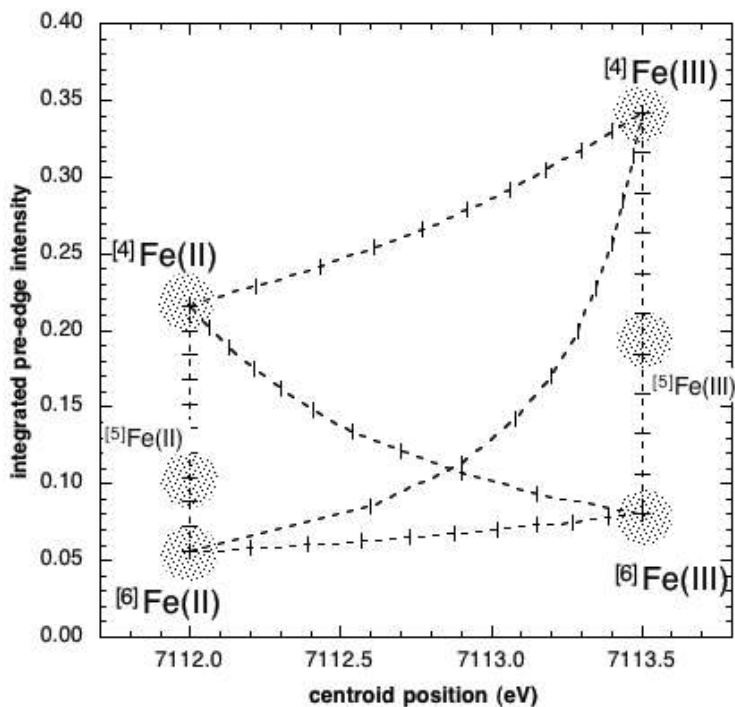


**Figure 5**. Relationship between centroid position of the pre-edge features, Fe coordination and oxidation state, (after Wilke et al. 2001, 2005; Petit et al. 2001) (provided courtesy of M Wilke).

normally have to worry about the presence of a second oxidation state like Ti$^{3+}$. At least under conditions relevant to most mineralogical and geochemical processes, because very strong reducing conditions must be present to produce Ti$^{3+}$.

Titanium *K*-edge spectra with Ti$^{4+}$ in 6-fold coordination ($^{[6]}$Ti) exhibit from 1-3 weak intensity pre-edge peaks (Fig. 6). These peaks are conventionally labeled A$_1$, A$_2$, and A$_3$, (at ~4968, ~4971 and ~4974 eV) with a shoulder observed on the low energy side of the A$_2$ peak. However, observation of the shoulder depends on the spectral resolution of the data and may not always be observed. Cabaret et al. (1999, 2010) used a full-potential linearized augmented plane wave (LAPW) method of calculating the pre-edge dipolar and quadrupolar transitions. They showed that the A$_1$ peak is due to a quadrupolar, $t_{2g}$, transition (Ti $1s \rightarrow$ Ti $3d$ ($t_{2g}$)) while A$_3$ is entirely dipolar in nature (Ti $1s \rightarrow$ Ti $4p$). However, the A$_2$ peak has contributions from both dipolar (Ti $1s \rightarrow$ Ti $4p$) and quadrupolar transitions (Ti $1s \rightarrow$ Ti $3d$ (e$_g$)). In addition they also concluded that the A$_2$ and A$_3$ contributions are related to medium range order as they are derived from the hybridizations of the central Ti-$4p$ orbital with the second shell Ti-$3d$ orbitals.

When Ti is 4-fold ($^{[4]}$Ti) or 5-fold ($^{[5]}$Ti) coordinated there is an increase in intensity of the A$_2$ peak due to increased mixing of the $3d$ quadrupole and $4p$ dipole states as the polyhedra become less centrosymmetric (cf., Fig. 7) or the centrosymmetry is broken by atomic vibrations (Brouder et al. 2010). Farges et al. (1996a) have defined three regions characteristic of Ti in $^{[4]}$Ti, $^{[5]}$Ti, and $^{[6]}$Ti coordination (Fig. 8) based on both the intensity and position of the A$_2$ pre-edge peak as well as its intensity. The pre-edge intensity, determined by comparing the intensity of the pre-edge (4850-4950 eV) region and the



**Figure 6**. Pre-edge features observed in rutile (TiO$_2$) Ti *K*-edge XANES spectrum (after Uozumi et al. 1992).



**Figure 7**. Ti *K*-edge spectra for selected crystalline phases containing $^{[4]}$Ti (K$_2$Ti$_2$O$_7$), $^{[5]}$Ti (K$_2$Ti$_2$O$_5$) and $^{[6]}$Ti (r-TiO$_2$) (after Farges et al.1996a, 1997).

average intensity of the XAFS region (5050-5200 eV) shows a general negative correlation with increasing Ti coordination. In addition, the position of the pre-edge peak is at lower energy for $^{[4]}$Ti relative to $^{[6]}$Ti by ~ 2 eV. The pre-edge peak characteristic of $^{[4]}$Ti is found at ~4969 eV with an intensity 80% or greater of the intensity of the main edge while the pre-edge feature of $^{[6]}$Ti is at ~4971 eV with a relative intensity of ~25% of the main edge. The five-fold ($^{[5]}$Ti) pre-edge peak occurs at energies intermediate between $^{[4]}$Ti and $^{[6]}$Ti values at~ 4970 eV with a relative intensity between 40-80% of the main edge. It is important to remember that it is *intensity* and *position* together that define the coordination. Using only one or the other is insufficient.
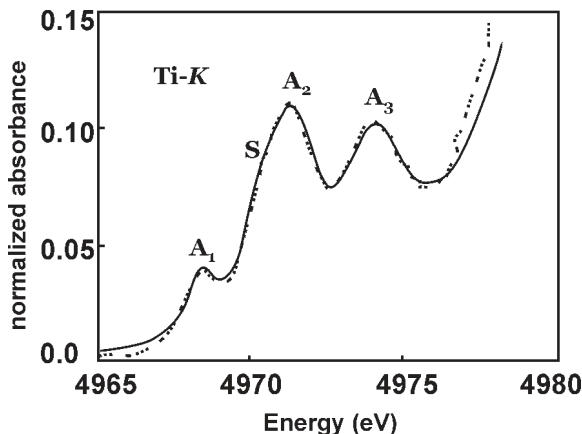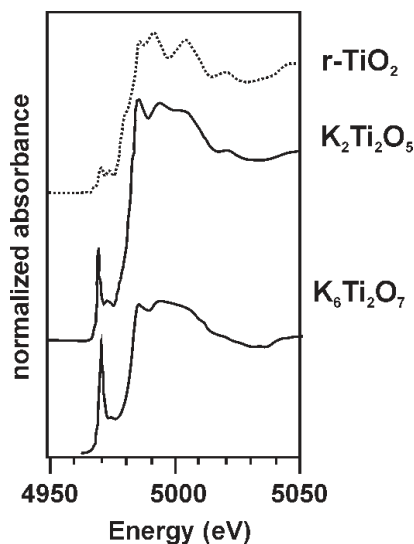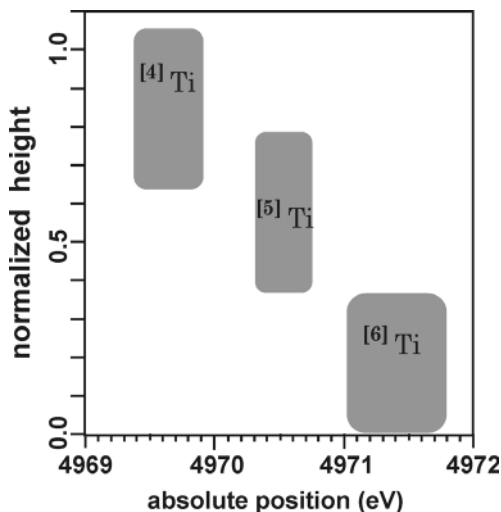
**Figure 8**. Plot of normalized pre-edge intensity versus energy position showing the three areas corresponding to [4]Ti, [5]Ti and [6]Ti (after Farges et al. 1996a, 1997).

In addition to being useful for determining the Ti coordination, the pre-edge features can also be used to estimate particle size. The intensity ratio of $A_2$ to $A_3$ increases as particle size decreases (Luca et al. 1998). The Ti *K*-edge itself consists of three or more features in the region of ~4950-5050 eV. These features can be described by multiple scattering effects between the ejected X-ray photo electron and the surrounding atoms or to transitions involving Ti $1s \rightarrow$ Ti $4p$ orbitals possibly with core hole effects (Poumellec et al. 1991a,b). Spectral features can be reproduced quite well using one of the theoretical codes available: either one of the multiple scattering or *ab inito*/first principles band structure codes noted above. In particular, the partial (or projected) density of states (p-DOS) is most useful for interpreting XANES spectra in general as this provides information on which orbitals are involved in the electronic transitions. Unfortunately the p-DOS is often not provided in simulation publications although it is commonly calculated during the simulations and a quick E-mail to the principle author is often helpful for obtaining it. Furthermore, using a "fingerprint" approach of comparing standards containing Ti in different crystal chemical environments one can use the linear combination method to help identify unknown Ti phases and different phases in samples containing mixtures of Ti-containing minerals etc.

When $Ti^{4+}$ is reduced to $Ti^{3+}$ the XANES spectrum and pre-edge features may still be analyzed to determine the Ti coordination state in a similar manner to unreduced samples. However, both the pre-edge and edge features are shifted to lower energy relative to the energy positions of features in the unreduced samples containing only $Ti^{4+}$ (Simon et al. 2007; Ollier et al. 2008). The magnitude of the energy shift depends upon how much $Ti^{4+}$ has been reduced to $Ti^{3+}$.

***Other transition metals.*** Essentially all of the first row transition metal *K*-edges have been investigated in minerals to some extent and a variety of examples are given below.

Titanium(Ti): Grunes 1983; Waychunas 1987; Uozumi et al. 1992; Paris et al. 1993; Dingwell et al. 1994; Farges et al. 1996a,b, 1997; Romano et al. 2000; Jiang et al. 2007; Cormier et al. 2011.

Vanadium (V): Nabavi et al. 1990; Abbate et al. 1993; Giuli et al. 2004; Sutton et al. 2005; Simon et al. 2007; Burke et al. 2012; Höche et al. 2013.

Chromium (Cr): Brigatti et al. 2000; Berry and O'Neil 2004; Berry et al. 2006;Villain et al. 2007; Gaudry et al. 2007; Odake et al. 2008; Juhin et al. 2008; Farges 2009; Fandeur et al. 2009; Frommer et al. 2009, 2010; Burke et al. 2012.

Manganese (Mn): Manceau et al. 1992; Farges 2005; Alvarez et al. 2007; Fandeur et al. 2009; Chalmin et al. 2009; Manceau et al. 2012.

Iron (Fe): Waychunas et al. 1983; Galoisy et al. 2001; Petit et al. 2001; Wilke et al. 2001; Farquhar et al. 2002; Berry et al. 2003a; Wilke et al. 2001, 2005, 2006; Magnien et al. 2008; Cottrell et al. 2009; Berry et al. 2010; Beck et al. 2012; Dyar et al. 2012; Rivard et al. 2013.

Cobalt (Co): Manceau et al. 1992; Choy et al. 2001.

Nickel (Ni): Manceau et al. 1992; Galoisy and Calas 1993; Farges et al. 1994; Giuli et al. 2000; Farges et al. 2001a,b; Fandeur et al. 2009; Curti et al. 2009; Essilfie-Dughan et al. 2012.

Copper (Cu): England et al. 1999; Alcacio et al. 2001; Mavrogenes et al. 2002; Berry et al. 2006; Cook et al. 2012.

Zinc (Zn): Pattrick et al. 1998; Waychunas et al. 2003.

In most cases, it is the pre-edge features that are used to determine oxidation state and coordination environment and, in particular, the position and intensity of the centroid of the pre-edge peaks rather than the position of the edge itself (cf., Cabaret et al. 2010). Reviews of TM *K*-edges have been given by de Groot (1993, 2008, 2009). Furthermore, the second and third row TMs are being increasingly studied as well with not only *K*-edges but also with *L*- *M*- and *N*-edges. Obtaining XANES spectra from these elements is a little more trying technically due to interference affects from the close proximity of other elemental edges.

**Transition metals: *L*-edges**

The 3*d* transition metal *L*-edges have been less studied, partly because of their large surface sensitivity. *L*-edges are also sensitive to changes in coordination and oxidation state, and because of their lower intrinsic broadening contain more information with regards to the electronic structure of the transition metal ions (Fister et al. 2007). The theory of XANES spectra of transition metal *L*-edge is described above. In case of $Ti^{4+}$ oxides the peak splitting within each edge is primarily due to the $t_{2g}$ $e_g$ symmetry of the *d*-orbitals in a centrosymmetric environment ($O_h$ symmetry for octahedral and 8-fold coordination) and is related (but not equal) to the crystal field splitting parameter 10D*q*. Further splitting of the higher energy peak within the $L_3$ edge has been attributed to distortion of the coordination environment (de Groot et al. 1992; Crocombette and Jollet 1994), possible second-neighbor interactions (Crocombette and Jollet 1994), coupling of electronic and vibrational states due to a dynamic Jahn-Teller effect (Brydson et al. 1989) or core hole effects (Crocombette and Jollet 1994). Without multiplet effects, the intensity ratio between the $L_3$ and $L_2$ edges is 2:1 and this ratio is observed for systems involving 4*d* electrons but not for 3*d* systems due to the large multiplet effects (de Groot et al. 1994).

*L*-edge spectra of 3*d* metals are collected in a similar manner to the *K*-edges above. However, experiments are carried out on what are commonly referred to as "soft X-ray" beamlines. These beamlines are usually limited in energy to <10 keV and in most cases require vacuum sample chambers. Spectra are collected over an energy range that covers both edges if possible with a step size equal to the lifetime broadening of about 0.1 to 0.2 eV. Data reduction is similar to that for *K*-edges with removal of the pre-edge background and fitting of an arctan or error function as above. However, with *L*-edges more than one such function usually must be fit to account for the $L_3$- and $L_2$-edge. The positions and heights of the functions are not well

known and consequently the fitting of such functions tends to be determined simply on what gives the "best fit" to the data.

In order to use the *L*-edges for determining coordination environments in minerals and glasses it is essential to carefully analyze the subtle changes in relative peak intensities and positions (cf., Henderson et al. 2003; Henderson and St-Amour 2004; Cormier et al. 2011). In addition, second nearest neighbors may also affect the spectra (Höche et al. 2013) and must be taken into account when selecting appropriate mineral standards for comparison or linear combination modeling (cf., Fig. 9).
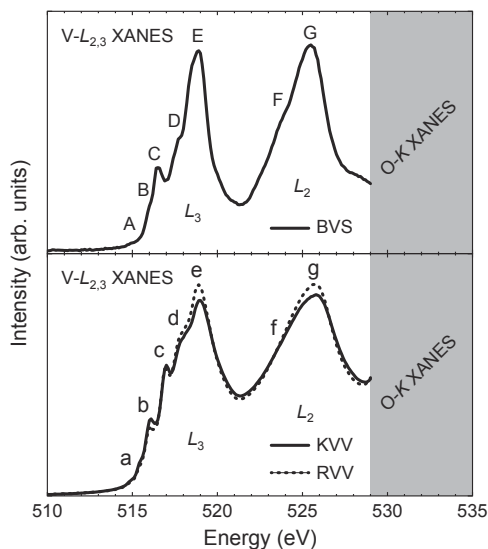


**Figure 9**. V $L_{2,3}$ spectra (~515-530 eV) for Ba (Ba$_2$VSi$_2$O$_8$) (top), potassium (K$_2$VV$_2$O$_8$) and rubidium (Rb$_2$VV$_2$O$_8$) vanadium fresnoites (bottom). Spectra in the bottom panel has V in two oxidation states and coordinations (V$^{4+}$ (CN = 5) and V$^{5+}$ (CN = 4) yet are quite similar to the top spectrum with V only in a single oxidation and coordination state (Used by permission of Mineralogical Society of America, from Höche et al. 2013, American Mineralogist, 98, Fig. 3, p 668).

*Titanium L-edges.* Some characteristic Ti *L*-edge spectra (~ 455-475 eV) are shown in Figure 10. The spectra are quite distinct for different Ti oxidation states (Ti$^{3+}$, Ti$^{4+}$) and for different coordination environments ([4]Ti, [5]Ti, [6]Ti). As noted above the lower valence state spectrum (Ti$^{3+}$) is at slightly lower energy relative to the higher valence state (Ti$^{4+}$). Titanium in 4-fold coordination exhibits two peaks in the $L_3$-edge with the higher energy peak being somewhat asymmetric with no splitting. This contrasts with [6]Ti where the second peak is split and where the relative intensities of the split peaks reverses for anatase versus rutile or brookite. Five-fold Ti exhibits a small $t_{2g}$ peak and a sharp $e_g$ peak and the splitting between the two peaks in the $L_3$-edge is reduced relative to [4]Ti and [6]Ti. At the $L_2$-edge the splitting and relative intensities of the $t_{2g}$ and $e_g$ peaks decreases from [6]Ti → [4]Ti → [5]Ti. In addition, [5]Ti has an additional small peak on the low energy side of the $L_2$-edge which may be due to differences between the $t_{2g}$ orbitals. However, caution must be used when determining coordination state since numerous factors affect the peak intensities and positions (see above). This is particularly important when investigating mineral phases where Ti can occupy more than one site (cf., Henderson and Foland 1996) and consequently the *L*-edge spectra are an average of the multiple sites. In all cases it is advantageous to have some sort of theoretical calculations available to aid interpretation (see above plus Höche et al. 2013).

*Iron L-edges.* The Fe$^{2+}$/Fe$^{3+}$ ratio is usually given as the fraction Fe$^{3+}$, Fe$^{3+}$/ΣFe. Systematic studies of the Fe 2*p* EELS spectra of a series of minerals give a reliable method to determine this ratio, based on the determination of the ratio of the Fe$^{3+}$ and Fe$^{2+}$ peaks in the $L_3$-edge (van
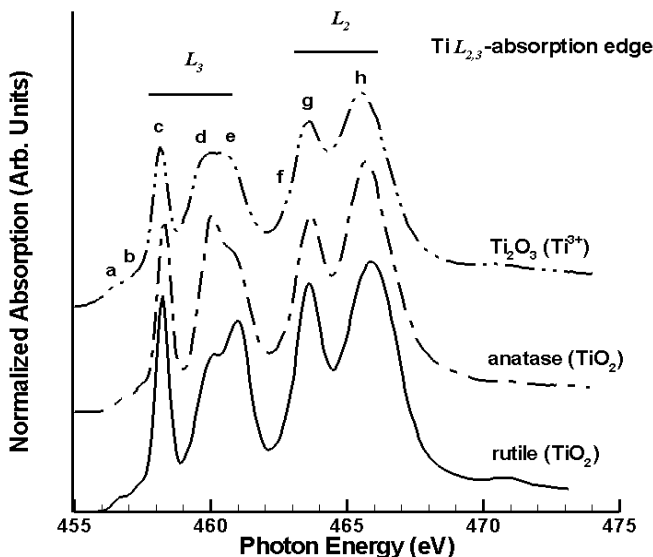
**Figure 10**. Representative spectra of the Ti *L*-edge. The *L*$_3$ and *L*$_2$ edges are indicated.

Aken and Liebscher 2002). An important application of the iron *L*-edges is the determination of the occupation of the tetrahedral and octahedral sites and the variation of divalent and trivalent ions for Fe in spinel ferrites, including $CoFe_2O_4$, $MnFe_2O_4$, $NiFe_2O_4$, $ZnFe_2O_4$ and $MgFe_2O_4$. The line shape of the Fe 2*p* XAS spectrum of $MnFe_2O_4$ is similar to those of both $\alpha\text{-}Fe_2O_3$ and $\gamma\text{-}Fe_2O_3$ indicating that the valence states of Fe ions in $MnFe_2O_4$ are mainly trivalent. Pattrick et al. (2002) analyzed a series of mixed spinel ferrite systems with 2*p* XAS and XMCD. By comparison with multiplet spectra, the site occupancies of the cations have been determined. It turns out that the different mixed (Co, Ni, Zn, Mg) ferrite spinels show considerable variation in site occupancies. Incomplete site speciation is found and the preference of Co, Ni and Mg for the octahedral site and Zn for the tetrahedral site is confirmed. An overview of the 2*p* XAS and XMCD spectra of spinel ferrites have been given by Pearce et al. (2006). The Fe *L*-edge XANES has recently been reviewed by Miedema and de Groot (2013).

*Other transition metal L-edges.* Cressey et al. (1993) give a general introduction of the use of transition metal *L*-edges in mineralogy. Charnock et al. (1996) analyzed the *L*-edges of Fe, Co and Ni sulfides, selenides and tellurides. They also discuss the related iron and nickel spectra. A recent paper is the determination of the valence of cobalt in carrollite $CuCo_2S_4$ by Pattrick et al. (2008). Cobalt *L*-edges of oxides have been published by van Elp et al. (1991), de Groot et al. (1993), Mizokawa et al. (2005) and Coker et al. (2008).

### Silicon and aluminum *K*- and *L*-edges

*Silicon K-edge.* The Si *K*-edge (~1830-1890 eV) is the lowest energy soft X-ray edge for which EXAFS data can be obtained. Edges occurring at lower energies are not able to provide a large enough energy range for EXAFS analysis due to interference from other elemental edges for most geochemically relevant materials. The edge itself has been extensively investigated both in minerals (cf., Li et al. 1993, 1994, 1995a; Gilbert et al. 2003) and glasses/melts (cf., Davoli et al. 1992; Henderson 1995; Henderson and Fleet 1997; Henderson and St-Amour 2004; de Wispelaere et al. 2004; de Ligny et al. 2009). Furthermore, a significant amount of work has been published on this edge using electron energy loss (EELS), parallel electron

energy loss (PEELS) or energy loss near edge spectroscopy (ELNES) and this literature can be very helpful for interpreting soft X-ray XANES spectra (cf., McComb et al. 1991; Garvie et al. 1994, 2000; Sharp et al. 1996; Poe et al. 1997; van Aken et al. 1998; Garvie and Buseck 1999).

The spectrum for α-quartz exhibits 5 main peaks labeled A-F in Figure 11a. While there have been a number of theoretical studies of the quartz and stishovite Si *K*-edge that reproduce the experimental spectra well (cf., Wu et al. 1998; Soldatov et al. 2000; Mo and Ching 2001; Taillefumier et al. 2002) they have not provided a detailed analysis of the p-DOS to enable explicit assignment of the peaks in the spectra. Li et al. (1994, 1995a) used previous molecular orbital studies and gas phase spectra of tetrahedral analogues to assign the peaks in quartz. They assigned the pre-edge peak (peak A) to a dipolar(?) $1s \rightarrow 3s$ transition. Peak B representing the main edge transition (also called white line or shape resonance in older literature) is due to a $1s \rightarrow 3p$ transition, peaks D and F to $1s \rightarrow 3d/p$ states and peaks C and E to multiple scattering from the structure beyond the first coordination sphere. Similar peaks and assignments can be made for stishovite (Fig. 11b) where Si is in 6-fold coordination ($^{[6]}$Si). However, the position of the edge is shifted to higher energy by ~2.2 eV consistent with other elemental edges when there is a change to higher coordination (see above and below).

The Si *K*-edge, compared to other soft X-ray edges, is relatively insensitive to structural changes, at least for silicate minerals (Fig. 11c). This is mostly a result of the nature of the $SiO_4$ tetrahedron, which is fairly well defined in most minerals and does not exhibit a large amount of distortion or variation in Si-O bond lengths relative to other polyhedra. Comparison of the $SiO_2$ polymorphs (Fig. 11b) shows that the pre-edge peak intensity tends to increase in the higher pressure phases, probably due to increased mixing of $3p$ states with the Si $3s$ (Li et al. 1994). Li et al. (1995a) also noted that there is a general shift in the position of the *K*-edge to higher energy with increasing polymerization (Fig. 11c), a weak correlation with Si-O bond length (shift to higher energy with shorter Si-O bond distance) and some dependence of the edge position on the nature of the next nearest neighbors ( NNN) In addition, Bender et al. (2002) have shown that the position of the edge shifts to lower energy as the Q species ($Q^n$, where *n* is the number of bridging oxygens attached to the silicon) shifts from $Q^4$ to $Q^0$.

In $SiO_2$ glass (Fig. 11a) the *K*-edge spectrum is more diffuse with peaks C-F being suppressed in intensity relative to crystalline $SiO_2$. This is due to the inherent disordered nature of glasses, which have a broad range of Si-O-Si angles and Si-O, and Si-Si distances compared to crystalline materials. Only four main peaks are observed. The pre-edge peak A occurs as a weak broadening at the base of the main edge feature, the main transition (Peak B), a weak peak around 1852 eV (Peak C) and a higher energy peak F due to transition of $1s \rightarrow 3d/p$ states, and whose intensity is related to the Si-O-Si angle, becoming more intense as this angle decreases (Davoli et al. 1992). The weak feature labeled C may be due to either transitions from $1s \rightarrow 3d/p$ states or multiple scattering. Unfortunately as noted above, the Si *K*-edge of glasses and melts exhibits even less compositionally dependent variation in peak positions and intensities than crystalline phases and is very uniform. By and large, the only changes observed in glasses (other than a shift of the edge due to a coordination change of Si) are in the ~1848-1855 eV region, are very subtle, and are most probably related to changes in the medium-range structure. An exception to this is a shoulder to the high-energy side of the main peak (B) at ~1849 eV which occurs in some glasses (cf., Fleet et al. 1997; Cabaret et al. 2001; Henderson and St-Amour 2004). It has been assigned to $^{[6]}$Si in phosphate glasses (Fleet et al. 1997) and silica-modified titanias (Iwamoto et al. 2005), or to changes in medium-range structure in alkali and alkaline-earth containing silicate glasses (Henderson and St-Amour 2004) and borosilicate glasses (Cabaret et al. 2001), initiated by the presence of a network modifier (Cabaret et al. 2001; Levelut et al. 2001). Its apparent presence in the Si *K*-edge spectra of a wide range of glass and amorphous compositions is intriguing but has not been explored further.
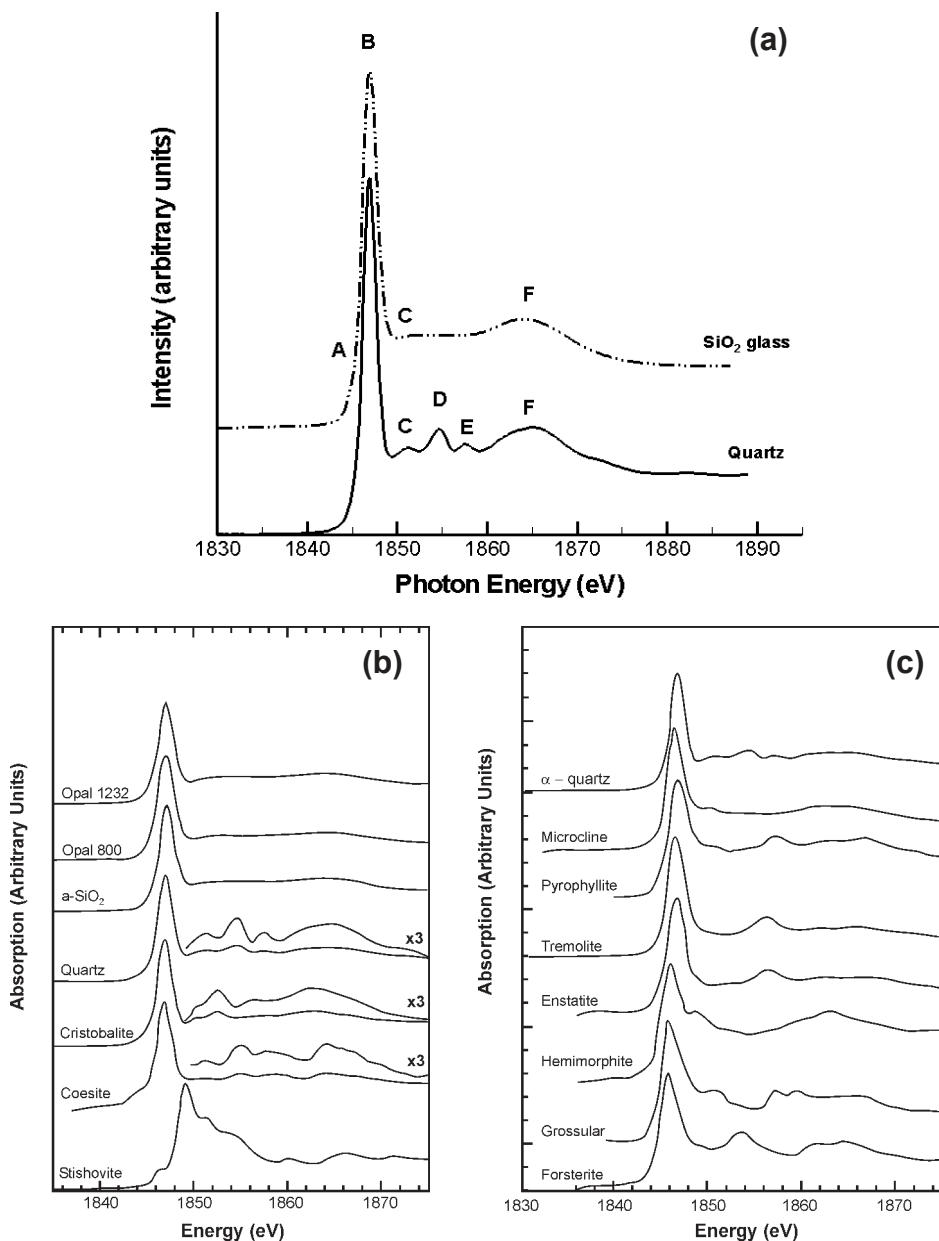
**Figure 11**. Si *K*-edge spectra, α-quartz and SiO₂ glass (a) opal, a-SiO₂ (glass) and SiO₂ polymorphs (after Li et al. 1994) (b) and minrals (c) (after Li et al. 1995b).

*Silicon L-edge.* Like the *K*-edge above, the Si *L*-edge (~100-140 eV) has also been reasonably well studied both by ELNES and XANES (McComb et al. 1991; Kasrai et al. 1993, 1996b; Li et al. 1993, 1994; Sharp et al. 1996; Poe et al. 1997; Garvie and Buseck 1999; Garvie et al. 2000; Gilbert et al. 2003). Peak assignments are similar to that of the Si *K*-edge

(see Fig. 12). However, no pre-edge feature is observed and peak A (Fig. 12) is split by spin-orbit (LS) coupling into two features ~1 eV apart due to the Si $2p_{3/2}$ ($L_3$) and $2p_{1/2}$ ($L_2$) states. This splitting may not be observed if the resolution of the monochromator is insufficient (older literature) or if there is broadening of the peaks due to instrumental affects or inherent broadening such as in amorphous materials. Li et al. (1993) suggest that the strongest feature (peak B) is shifted by ~2 eV to higher energy in stishovite with [6]Si relative to α-quartz with [4]Si, as observed for the *K*-edge. However, Sharp et al. (1996) using ELNES do not observe this. A large number of minerals have been investigated by Garvie and Buseck (1999) using PEELS. They observe a linear increase in energy of the edge onset with increasing polymerization and that the edge features are affected by the NNN and their bonding environments. Although it should be remembered that PEELs lacks the energy resolution of XANES and consequently some features, such as the LS doublet, are not clearly resolved.
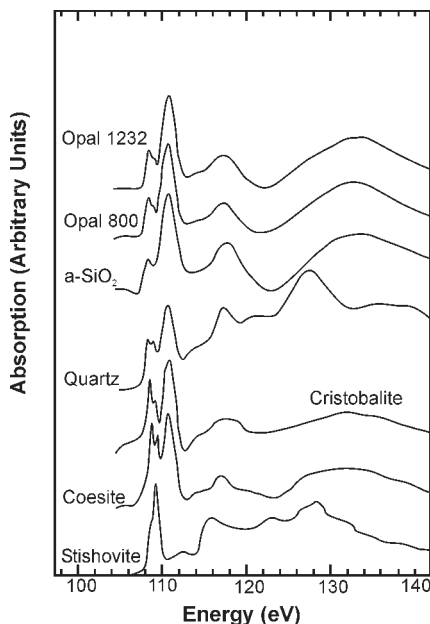


**Figure 12**. Si *L*-edge spectra of the $SiO_2$ polymorphs (after Li et al. 1994).

*Aluminum K-edge.* The aluminum *K*-edge (~1550-1650 eV) has been extensively utilized in mineralogical and geochemical studies (McKeown et al. 1985; McKeown 1989; Ildefonse et al. 1994, 1995, 1998; Li et al. 1995b; Fröba et al. 1995; Wu et al. 1997a; Giuli et al. 2000; Romano et al. 2000; Arai and Sparks 2002; van Bokhoven et al. 2003; Neuville et al. 2004a, 2010; de Wispelaere et al. 2004; Khare et al. 2005; Hu et al. 2008; Xu et al. 2010; Rivard et al. 2013). In general the Al *K*-edge for 4-fold coordinated Al ([4]Al) occurs at ~1566 eV and usually exhibits a single edge maximum or peak. The Al *K*-edge of 6-fold coordinated Al ([6]Al) is ~1.5-2.0 eV higher in energy relative to that of [4]Al and usually exhibits a peak with a maximum at ~1568 eV and a secondary but relatively strong peak at ~1572 eV (see Fig. 13). The shift to higher energy for the higher coordination is simply because the core hole is more effectively screened in octahedral coordination (van Bokhoven et al. 2001).

Both edges have multiple peaks usually labeled A-E by various authors[2]. In Figure 13 the experimental spectrum for berlinite ($AlPO_4$), containing only [4]Al, exhibits 5 main peaks. Peak A is the Al edge due to Al $1s \rightarrow 3p$ transitions and, as noted above, its intensity will depend on the screening of the core hole (Cabaret et al. 1996). In some spectra a pre-edge feature may also be observed (cf., Corundum in Fig. 13) and this is due to $1s \rightarrow 3s$ dipolar transitions that would normally be forbidden by quantum mechanical selection rules but become allowed due to effects from vibrations (Li et al. 1995b; Manuel et al. 2012). This pre-edge feature will increase in intensity with increasing temperature and shift to lower energy (Manuel et al. 2012). The other peaks have been variously assigned to multiple scattering (B and D), $1s \rightarrow 3d$ transitions (C and E), (Li et al. 1995b) or to multiple scattering from medium range environment (Cabaret et al. 1996). Their positions and intensity will depend upon Al site multiplicity, bond angles

---

2     Note it is important to be careful when comparing peak assignments from one author to the next as they do not necessarily label peaks the same or in a consistent manner
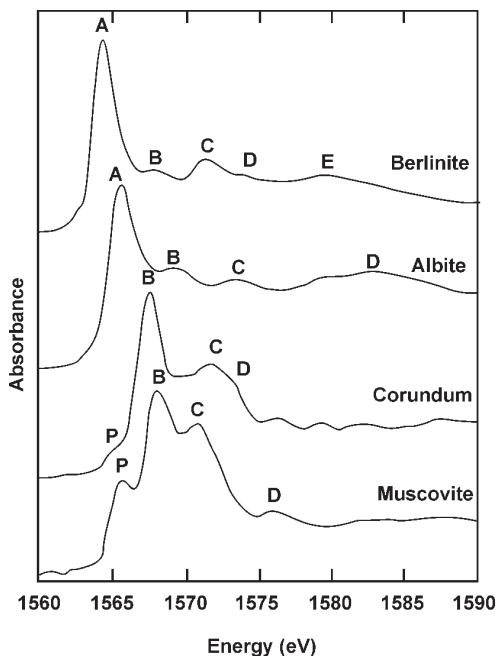
**Figure 13**. Al K-edge spectra of Berlinite (AlPO$_4$, [4] Al), Albite (NaAlSi$_3$O$_8$, [6]Al), corundum (Al$_2$O$_3$, [6]Al) and muscovite (KAl$_2$(AlSi$_3$O$_{10}$)(OH)$_2$, [4]Al and [6]Al) after Ildefonse et al. 1994;Cabaret et al. 1996). Note that muscovite has both [4]Al and [6]Al and has XANES peaks characteristic of both coordinations.

and lengths, and NNN (Fröba et al. 1995; Li et al. 1995b; Wu et al. 1997a; Ildefonse et al. 1998). For example, the edge position of peak A in berlinite is at higher energy than for other [4]Al only compounds because the NNN to Al are phosphorous, which decrease the electronic density around the Al.

The spectrum for corundum (Al$_2$O$_3$) with only [6]Al exhibits a pre-edge peak (P) at 1565 eV, a sharp edge peak (A) at ~1568 eV due to Al $1s \rightarrow 3p$ transitions along with a secondary peak (B) at ~1572 eV due to $1s \rightarrow 3d$ transitions (Ildefonse et al. 1998). Peak C has been assigned to multiple scattering (Li et al. 1995b). However, the spectra for [6]Al minerals are more variable than those of [4]Al containing phases due to variations in site symmetry, site occupancy and Al-O bond lengths (Ildefonse et al. 1998).

Aluminum may also occur in 5-fold coordination ([5]Al), especially in calcium aluminosilicate glasses and melts (Neuville et al. 2004a). However, discriminating between [4]Al or [6]Al and [5]Al is difficult. Cer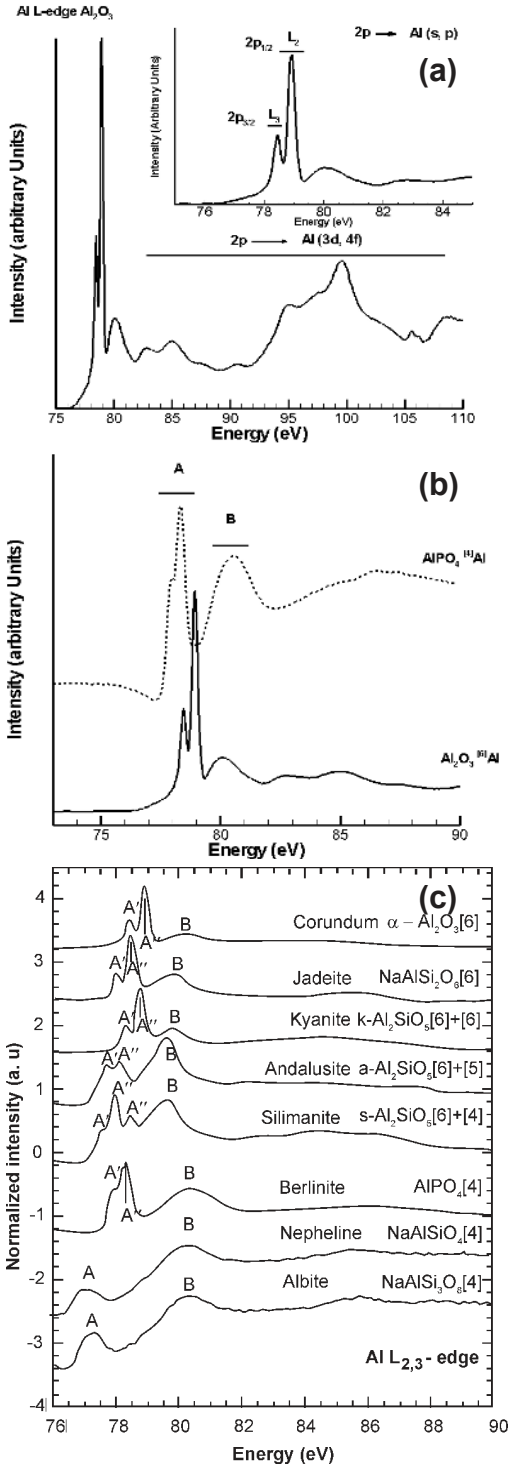tainly in minerals such as the Al$_2$SiO$_5$ polymorphs (sillimanite, andalusite and kyanite) with [4]Al and [6]Al, [5]Al and [6]Al and all [6]Al, respectively, it is not possible to unambiguously determine features that are characteristic of [5]Al (Ildefonse et al. 1998). Li et al. (1995b) have interpreted a peak at ~1567.8 eV in their spectra as being due to [5]Al and lying between peaks at 1566.7 and 1568.7 eV characteristic of [4]Al and [6]Al, respectively although their peak assignments having been brought into question (Ildefonse et al. 1998). Nevertheless van Bokhoven et al. (1999), Chaplais et al. (2001), Hu et al. (2008), and Neuville et al. (2009) have all assigned a peak in their Al *K*-edge spectra to the presence of [5]Al based on its position mid-way between peaks characteristic [4]Al and [6]Al.

***Aluminum L-edge.*** Relative to the Al *K*-edge there have been relatively few mineralogical studies (Bianconi 1979; Balzarotti et al. 1984; Chen et al. 1993a,b; van Bockhoven et al. 2001; Hu et al. 2008; Weigel et al. 2008; Shaw et al. 2009; Zhang et al. 2009; Neuville et al. 2010; Xu et al. 2010), involving the Al *L*-edge (~75-90 eV) despite the increased resolution of *L*- versus *K*-edges (see above). However, like the silicon above, there has been a significant amount of work published on this edge using EELS, PEELS and ELNES and this literature can be very helpful for interpreting the spectra.

Like other *L*-edges the main features of the spectra arise from excitation of an Al $2p$ electron to unoccupied *s* and *d*-like states but in this case are termed excitons since the excitation energy lies in the band gap (cf., Weigel et al. 2008 and references therein). The edge is split into two components the $2p_{3/2}$ ($L_3$) and $2p_{1/2}$ ($L_2$) due to LS coupling. Figure 14a shows a high-resolution spectrum for corundum (sapphire) as well as the transitions contributing to the spectrum. The split feature at ~79 eV (inset) is the $L_{2,3}$ edge. The edge is shifted to lower

Al L-edge Al₂O₃

**(a)**

$2p \longrightarrow$ Al (s, p)

$2p_{1/2}$ $L_2$

$2p_{3/2}$ $L_3$

$2p \longrightarrow$ Al (3d, 4f)

**(b)**

A

B

AlPO₄ [4]Al

Al₂O₃ [6]Al

**(c)**

A' A'' B Corundum α – Al₂O₃[6]

A'A'' B Jadeite NaAlSi₂O₆[6]

A'A'' B Kyanite k-Al₂SiO₅[6]+[6]

A'A'' B Andalusite a-Al₂SiO₅[6]+[5]

A'A'' B Silimanite s-Al₂SiO₅[6]+[4]

A' B Berlinite AlPO₄[4]

A B Nepheline NaAlSiO₄[4]

A B Albite NaAlSi₃O₈[4]

Al L₂,₃ - edge

**Figure 14**. a) Al *L*-edge spectrum of corundum (variety sapphire) showing the transitions responsible for the spectral features. The inset show the $L_{2,3}$ peaks, b) High-resolution spectra (uncorrected) of berlinite (top, [4]Al) and corundum (bottom, [6]Al) along with peaks conventionally labeled A and B, c) XANES Al $L_{2,3}$-edge spectra of crystals and glasses (the numbers in brackets indicate the Al CN.) (after Weigel et al. 2008).

energy by ~1.5 eV for [4]Al versus [6]Al (Fig. 14b) similar to the Si $L_{2,3}$ edge (see above). This is because the core hole is more effectively screened in octahedral coordination (van Bokhaven et al. 2001). The position of the edge jump is also affected by a number of other factors. It is shifted to lower energy by increased bond covalency, the presence of Si as next nearest neighbors (NNN) and the presence of alkalis; the least polarizing NNN cations move the edge jump to lower energy. Weigel et al. (2008) investigated a number of mineralogical phases with varying Al coordination (Fig. 14c). The Al $L_{2,3}$ edges exhibit variations in position, intensities, and degree of splitting. There are two main spectral regions labeled A and B following the convention of Chen et al. (1993a). The A feature is the $L_{2,3}$ edge while the B feature, due predominantly to Al 2*p* transitions to unoccupied Al 3*s* states, is common to all spectra but varies in intensity relative to A due to site distortion and selection rules (in octahedral coordination) (Hansen et al. 1994) and increased *s-p* hybridization (for tetrahedral coordination). Furthermore it tends to be at higher energy relative to peak A in tetrahedral compared to octahedral environments.

The Al $L_{2,3}$ edge (A feature) exhibits more than two peaks in the phases with more than a single Al coordination environment. This is because the $L_{2,3}$ edges of the two sites are overlapping. For example, in the sillimanite spectrum the low energy A'

peak is the $L_3$ edge of [4]Al, the high energy A''' peak the $L_2$ edge of [6]Al while the intermediate peak is a superposition of the $L_2$ edge of [4]Al and the $L_3$ edge of [6]Al (Weigel et al. 2008). The resolution of the A feature depends to some extent on the number of Al sites in the crystal structure, their site occupancies and NNN distribution, all of which tend to broaden the edge. Glass spectra are inherently broad due to their disordered nature, lack of symmetry and wide distribution of bond lengths and angles.

Weigel et al. (2008) also showed that there is a correlation between the position of the peak maximum of the Al $L_3$-edge and the Al-O bond length: the smaller the Al-O bond length the lower the energy of the edge. In addition, the relative intensities of the $L_3$- and $L_2$-edges can be used to calculate the exchange energy (see above and Eqn. 1 of Chen et al. 1993a and Weigel et al. 2008).

### Alkalis (Li, Na, K, Rb, Cs)

*Lithium K-edge.* There are very few experimental XANES studies of the Li $K$-edge (~50-100 eV) because of the difficulty of making measurements at these very low energies as well as the overlap in energy with other elemental edges. The majority of studies have been related to the electrochemical and battery industries (cf., Tsuji et al. 2002; Kobayashi et al. 2007; Lu et al. 2011). The Li $K$-edge for some common compounds is shown in Figure 15.

Generally, the $K$-edge spectra exhibit a relatively intense peak at ~ 62 eV with secondary peaks between 62-65 eV and possibly a broad peak at ~70 eV. The intense sharp feature at 62 eV is a core exciton probably resulting from a $1s$ transition to unoccupied $2p$ states. In lithium halides, this core exciton peak exhibits a linear dependence on the electronegativity of the halide (Fig. 15a); the larger the electronegativity difference between Li and the halide the higher the peak energy (Handa et al. 2005). In some spectra the core exciton peak is relatively weak and appears as a low energy shoulder (Fig. 15b). Its position is also dependent on the
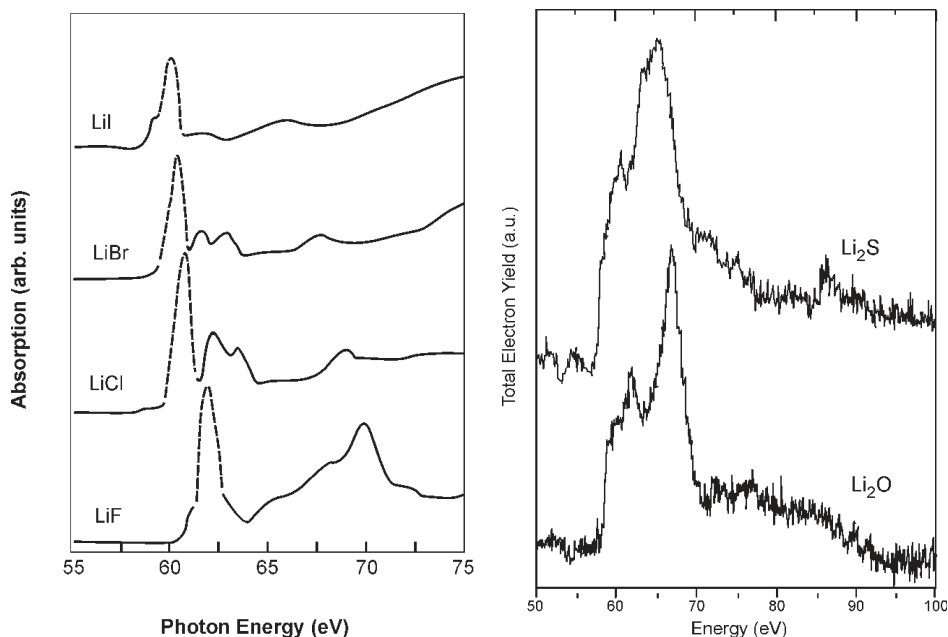


**Figure 15**. Li K-edge spectra of the Li halides (*left*) and a comparison of $Li_2O$ and $Li_2S$ (*right*), (after Handa et al. 2005 and Tsuji et al. 2002).

oxidation state of the anionic group attached to the Li. The peak shifts to higher energy with decreasing oxidation state (Tsuji et al. 2002). There have been some theoretical simulations (Jiang and Spence 2004; Mauchamp et al. 2006, 2008; Olovsson et al. 2009a,b) but they do not provide sufficient details on the p-DOS to aid interpretation of the experimental spectra. The low energy of the Li *K*-edge makes in-situ experiments difficult. Recently an XRS study of the Li *K*-edge was performed using hard X-rays (Miedema et al. 2012).

***Sodium K-edge.*** The first comprehensive Na *K*-edge (~1065-1125 eV) study of minerals and glasses was that of McKeown et al. (1985) although the energy resolution was relatively poor. Since then there have been several studies of alkali halides (Murata et al. 1988; Fujikawa et al. 1989; Kasrai et al. 1991; Hudson et al. 1994) but few studies of other minerals and glass-es. Mottana et al. (1997) looked at Ca-Na pyroxenes while Neuville et al. (2004b) have looked at a range of mineral phases and glasses. Glasses have also been investigated by Cormier and Neuville (2004) who looked at Ca-Na glasses and De Wispelaere et al. (2004) who investigated Na silicate and sodium-alumino-silicate glasses. Representative spectra are shown in Figure 16. The sodium *K*-edge of crystalline phases, other than the halides, consists of essentially two peaks at ~1078 eV and ~1082 eV (Cormier and Neuville 2004) with a pre-edge peak occurring at ~ 1174 eV. This pre-edge peak is not always present and arises from a dipolar $1s \rightarrow 3s$ transition (Murata et al. 1988; Teodorescu et al. 2000). The first main peak at ~1078 eV has been assigned to a Na $1s \rightarrow 3p$ transition while the origin of the second peak at ~ 1082 eV remains ambiguous but is usually assigned to



**Figure 16**. Na K-edge spectra of selected minerals and glasses (after Neuville et al. 2004b).

multiple scattering beyond the immediate Na environment as are peaks above ~1090 eV (cf., Neuville et al. 2004b). A similar assignment can be made for the alkali halides (Teodorescu et al. 2000; Kikas et al. 2001; Prado and Flank 2005). Peaks are also reproduced quite well by multiple scattering theory (Hudson et al. 1994; Riedler et al. 2001a,b). There is a correlation between the higher energy peaks in the halides and the $1/R^2$ rule (see above).

The two main peaks and their relative intensities appear to be a reasonable indicator of Na coordination environment when compared to model compounds (McKeown et al. 1985; Neuville et al. 2004b). The more ordered the Na environment the narrower the peaks. In addition, the intensity of the second peak tends to increase relative to the first peak as Na coordination increases (Cormier and Neuville 2004). There also appears to be an edge shift to lower energy with increasing Al/Na ratio, at least up to a ratio of 1.0 (McKeown et al. 1985), but the overall shape of the spectra are not affected significantly with Al substitution for Si (Cormier and Neuville 2004).
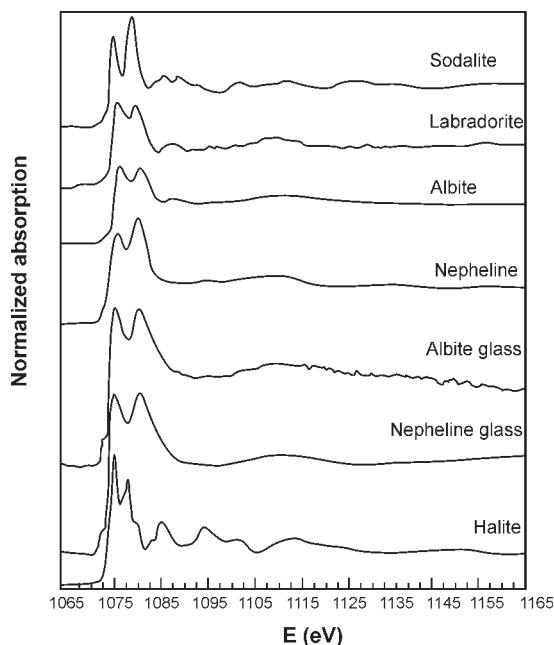
***Potassium K-edge.*** The majority of K $K$-edge (Fig. 17) studies have been on micas (cf., Mottana 2004; Cibin et al. 2005, 2006, 2010; Marcelli et al. 2006; Brigatti et al. 2008) often using a polarized incident beam in order to look at the angular dependence of the $K$-edge with respect to the layered mica structure. The shape of the K $K$-edge (~3595-3680 eV) is similar to that of the Na $K$-edge with two main peaks being observed at ~3610 eV and ~3615 eV. The edge onset shifts to higher energy with increasing K coordination for minerals with similar K environments (Cibin et al. 2005; Marcelli et al. 2006).

Additional peaks are observed at ~3625, ~3630 and ~3640 eV with the peak at ~3625 eV exhibiting a correlation in micas with the out of plane tetrahedral rotation of the tetrahedral sheet and the environment around the interlayer cation (Marcelli et al. 2006), while the peak at ~3630 eV appears to be related to the interplanar spacing



**Figure 17**. K $K$-edge spectra of some common minerals (after Cibin et al. 2005).

between the interlayer and tetrahedral sheet (Brigatti et al. 2008). Brigatti et al. (2008) also suggest that the peak at ~3640 eV is related to the peak at ~3630 eV and has some link to the distance between the A and T sites in micas. Simulations, both multiple scattering and first principles DFT calculations, reproduce the experimental spectra quite well (Lavrentyev et al. 1999; Vinson et al. 2011; Xu et al. 2011). However, detailed p-DOS calculations and analysis of the individual peaks are not given.

***Rubidium K-edge.*** The Rb $K$-edge (~15150-15260 eV) arises from Rb $1s$ transition to unoccupied p states but like the Cs edge below is broadened due to core-hole lifetime broadening (~3 eV)(cf., Soldatov et al. 1996 and references therein). In the case of RbBr there is some indication that the Rb $p$ states are hybridized with the Br $p$ states. In addition, the edge onset shifts with change in Rb oxidation state ($Rb^+$ to $Rb^-$) moving to lower energy with increasing electronegativity (Fussa-Rydel et al. 1988).

Some representative spectra are shown in Figure 18. While there is some variation in the edge features these subtle changes have not been investigated further and the behavior of the Rb $K$-edge remains relatively unexplored.

***Cesium K-edge.*** The Cs $K$-edge is at very high energy (~35940-36040 eV) and almost featureless because of core-hole broadening (~14 eV). Consequently there are few studies of this edge (usually in the gas phase). The Cs $L_3$-edge (energy?) has less broadening and is at lower energy but it too has not been utilized to any large extent (cf., Rossetti et al. 2011).

## Alkaline-Earths (Be, Ca, Mg, Sr, Ba)

***Beryllium K-edge.*** As far as we are aware there are no published Be $K$-edge (~110-160 eV) XANES experimental data. However, there are Be $K$-edge spectra obtained by X-ray Raman (Soininen et al. 2001). The $K$-edge exhibits two relatively sharp peaks at ~119 eV and~124
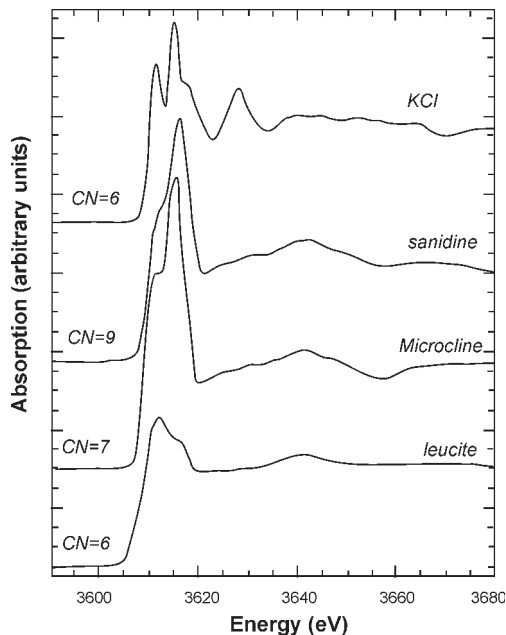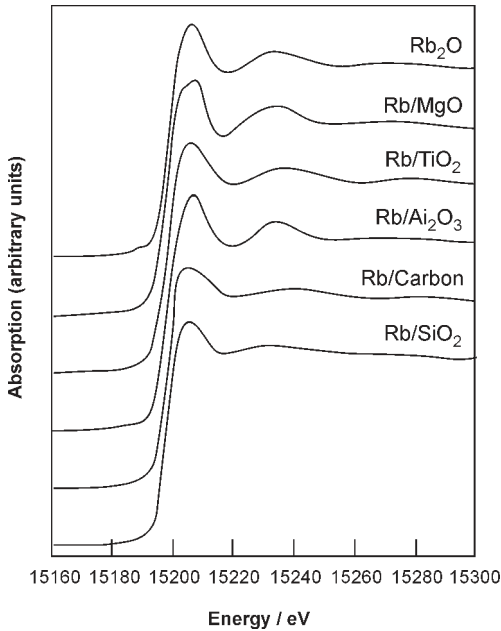
**Figure 18**. Rb *K*-edge on various support substrates at 77K (after Doskocil et al. 1997).

eV. The latter peak is somewhat less intense. There is also a broad low intensity peak at ~139 eV. The first peak is due to a core exciton and the overall spectrum is reproduced quite well by theoretical calculations (Soininen et al. 2001; Gao 2010) but there has been no detailed analysis of the individual peaks.

***Calcium K-edge.*** The Ca *K*-edge (~4020-4100 eV) has been used to determine Ca coordination in minerals (Paris et al. 1995; Quartieri et al. 1995) and glasses (Cormier and Neuville 2004; Neuville et al. 2004a) using the "fingerprinting" method of comparison with known mineral standards (Fig. 19). There appears to be a linear relationship between the energy of the edge and coordination (Sowrey et al. 2004), at least up to a Ca coordination of 9. The edge shifts to higher energy (~ 1 eV) as Ca coordination increases. The relationship does not hold for co-
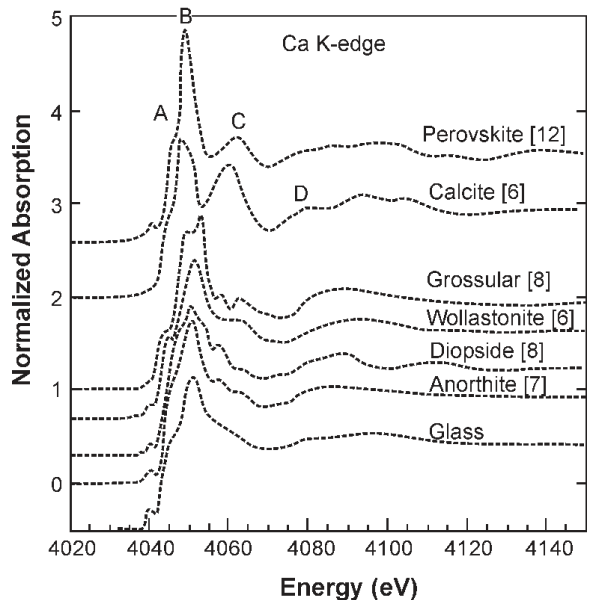
ordination numbers greater than 9. However, the post-edge shape of the XANES envelope is characteristic for higher coordinated (> 9) Ca (Sowery et al. 2004).

The XANES spectrum often exhibits one or more small pre-edge features at ~4040 eV, a shoulder on the low energy side of the edge at ~4045 eV, the main edge at ~4050 eV, with several higher energy peaks at ~4060 eV. The XANES has been modeled successfully using multiple scattering (Xu et al. 2013). However, Cabaret et al. (2013) have recently carried out first principle DFT calculations on the Ca *K*-edge in graphite intercalation compounds. They provide a detailed analysis of the interatomic interactions contributing to the edge features, which can be used to aid



**Figure 19**. Ca K-edge spectra of anorthite glass and some common Ca containing minerals, (after Cormier and Neuville 2004).

the interpretation of Ca XANES features in other phases. Cabaret et al. (2013) assign the pre-edge feature to a quadrupolar $1s \rightarrow 3d$ transition that becomes dipole allowed due to mixing with Ca $4p$ states. It does not occur if the Ca is in a centrosymmetric site. Peak A is due to Ca $1s \rightarrow$ Ca $4p$ states mixed with $3d$ and $4s$ states of NNN Ca atoms. In the graphite intercalation compounds there is also a contribution from $\pi^*$ states (see C $K$-edge). Similar contributions may occur with other types of ligands. Peak B is due to Ca $4p$ interactions with NNN Ca $3d$ and $4s$ states and ligand $\pi^*$ states. The main peak C above is due to Ca $4p$ states mixed with NNN Ca $4p$ states and ligand $\sigma^*$ states (see C $K$-edge). The peak D is a result of in plane hybridization between Ca $4p$ states but is variable in intensity and position and not fully explained by DFT calculations.

*Magnesium K-edge.* Mg $K$-edge (~1300-1400 eV) XANES has been used to investigate the coordination of Mg in a variety of minerals such as calcite and aragonite (Finch and Alison 2007), pyroxenes (Mottana et al. 1999), perovskites (Andrault et al. 1998), garnet and spinel (Ildefonse et al. 1995; Quartieri et al. 2008; Neuville et al. 2009), silicates and phyllosilicates (Li et al. 1999; Miehé-Brendlé et al. 2010), and several other mineral phases (cf., Trcera et al. 2009 and references therein). It has also been used to study the Mg coordination in glasses (Li et al. 1999; Trcera et al. 2009) and melts (Neuville et al. 2009). The spectrum consists of around 5 or more peaks; three in the region of 1300-1320 eV (labeled A-C in Fig. 20) and two broader peaks at ~1323 and ~1331 eV (labeled D′ and D in Fig. 20). Additional shoulders and smaller peaks may also be observed depending upon the composition of the sample, as well as, a pre-edge feature at ~1305 eV. The pre-edge peak is due to a dipolar $1s \rightarrow p$ transition of the Mg atom possibly with contributions from the empty Mg $3s$ states (Trcera et. 2009).

The edge has been shown to move to higher energy (~2.5 eV) between [4]Mg and [8]Mg (Trcera et al. 2009) with increasing Mg coordination and this can be used to discriminate [4]Mg/[6]Mg, and
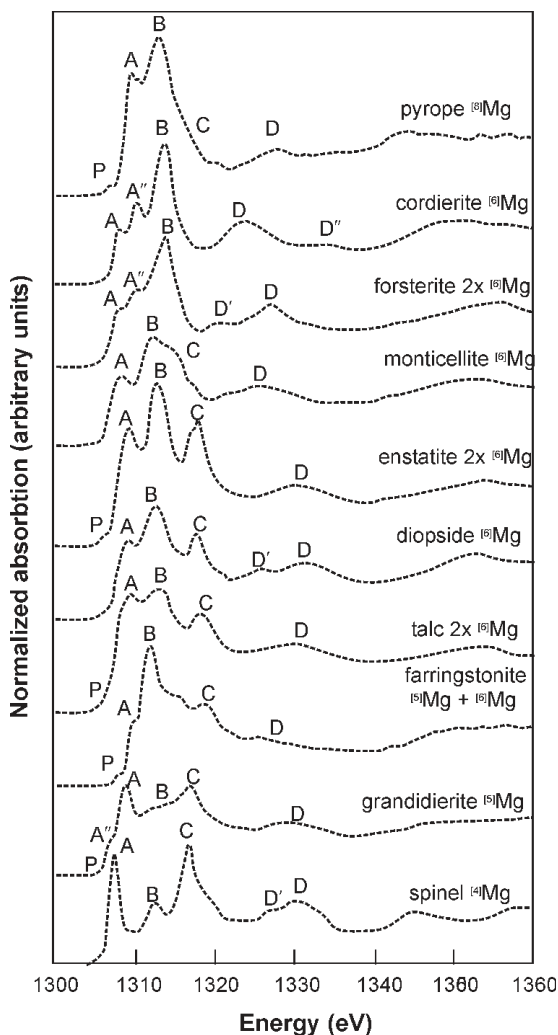


**Figure 20**. Mg $K$-edge spectra for a variety of minerals (after Trcera et al. 2009). The splitting of the A peak is due to different Mg site occupancies.

[6]Mg/[8]Mg sites (Ildefonse et al. 1995). However, it is not possible to resolve [5]Mg. The shift is related to increasing Mg-O bond lengths as the coordination changes (Li et al. 1999). However, caution should be used in using the edge shift as it is also correlated with site distortion, shifting to lower energy with increasing site distortion of $MgO_4$ or $MgO_6$ polyhedra (Trcera et al. 2011).

Peaks A/D and B are due to Mg $1s \rightarrow 3p$ transitions of the absorber atom mixed with other Mg *s* (peaks A/D) and *p* states (peak B), respectively and can be correlated with Mg site occupancies in minerals. Peak D and higher energy peaks also involve contributions from the Mg *d* orbitals (Mizoguchi et al. 2006). The appearance of peak C seems to have some sort of relationship to the presence or absence of Fe in minerals (Trcera et al. 2009). Early multiple scattering studies (cf., Wu et al. 1996; Cabaret et al. 1998) indicated that the spectrum was sensitive to changes in short and medium range order. Recently, Trcera et al. (2009, 2011) have carried out first principle DFT calculations. Unlike the Ca *K*-edge, the Mg *K*-edge does not appear to be sensitive to the degree of polymerization in glasses. However, the energy positions and intensities of the main peaks do depend on the nature of the alkali cation present in the glass. Peak A shifts to lower energy as the atomic number of the alkali increases and peak C exhibits a correlation with the Mg-alkali distance. Peak B is not sensitive to the nature of the alkali present (Trcera et al. 2009).

***Strontium K-edge.*** The Sr *K*-edge (~16080-16200 eV) has been used to investigate the Sr environment in carbonate phases and solutions (Kohn et al. 1990; Pingitore et al. 1992; Greegor et al. 1997; Parkman et al. 1998; Finch and Alison 2007; Borchert et al. 2013). The Sr *K*-edge (Fig. 21) is distinct when Sr is contained in calcite (Sr in 6-fold coordination) with a double peak feature at ~16115 and ~16130 eV, and a broader peak at ~16160 eV whereas in aragonite (Sr in 9-fold coordination) it has a single peak at ~16115 eV and a broad peak at ~16150 eV (Finch and Alison 2007).

***Barium K-edge.*** As far as we are aware there are no Ba *K*-edge (~37435-37485 eV) studies of minerals or glasses. However, the Ba $L_3$-edge (~5200-5300 eV) has been used to identify various Ba-containing carbonate and biomineral phases (cf., Finch et al. 2010) and glasses (cf., Handa et al. 2006).
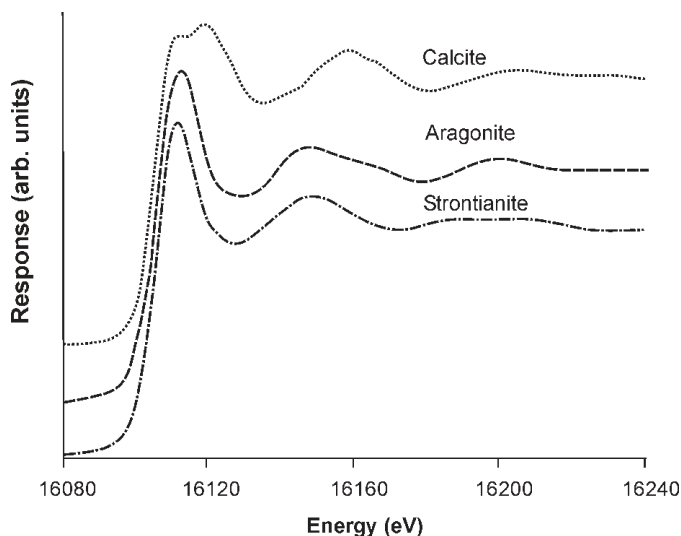


**Figure 21**. Strontium *K*-edge of three common Sr-containing minerals, (after Finch and Alison 2007).

## Ligand edges (C, O, B, S, P)

***Carbon K-edge.*** The carbon *K*-edge (~280-320 eV) of graphite (Mele and Ritsko 1979; Terminello et al. 1991) is shown in Figure 22, and is due to exciton transitions of the C 1*s* electron to unoccupied C 2*s* and 2*p* states. Furthermore it is divided into what are termed σ* (>290 eV) and π*states (<290 eV). The former involve the C 2*s*, 2*p_x* and 2*p_y* orbitals and the latter the C 2*p_z* orbital (Skytt et al. 1994). The σ* states lie in the plane of the C-C bond while the π* states are perpendicular to the C-C plane. As a consequence of this π* states are particularly sensitive to changes in incident beam orientation (Rosenberg et al. 1986; Brühwiler et al. 1995), as well as, the nature of the functional groups attached to the C (Boese et al. 1997). The σ* states are sensitive to the nature of the C-C and C=C bonds; C-C σ* states have peak energies lower than C=C σ* states (Hitchcock et al. 1986).

Diamond has also been studied (Morar et al. 1985; Ma et al. 1992, 1993) and exhibits a characteristic sharp σ* exciton peak at ~289 eV similar to that of graphite (~292 eV). Furthermore, the ratio of the π*/σ* states has been used to measure irradiation damage to the surface of the diamond (Reinke et al. 2000).

Currently, the C *K*-edge is widely utilized for discriminating the nature of carbon compounds in soils (Jokic et al. 2003; Solomon et al. 2005, 2012), amino acids (Kaznacheyev et al. 2002), and carbonyl compounds (Urquhart and Ade 2002). In recent years it is routinely employed in STXM experiments on organic materials (cf., Brandes et al. 2008; Lawrence et al. 2012).



**Figure 22**. C *K*-edge of graphite showing σ* and π*states (*top*, after Terminello et al. 1991) and orientational effects of the incident beam on the sample surface, (*bottom*, after Rosenberg et al. 1986).

***Oxygen K-edge.*** Oxygen *K*-edge XANES (~520-580 eV) generally results from an O 1*s* transition to O 2*p* anti-bonding states mixed with cation orbitals (cf., de Groot et al. 1989; Cabaret et al. 2007). Of particular interest is that the edge is sensitive to interactions with the cations bound to the oxygen (Fig. 23) and consequently contains information not just on the oxygens but also on the surrounding cations (cf., Wang and Henderson 2004; Henderson et al. 2007, 2009; Cabaret et al 2007; Zhang et al. 2010).
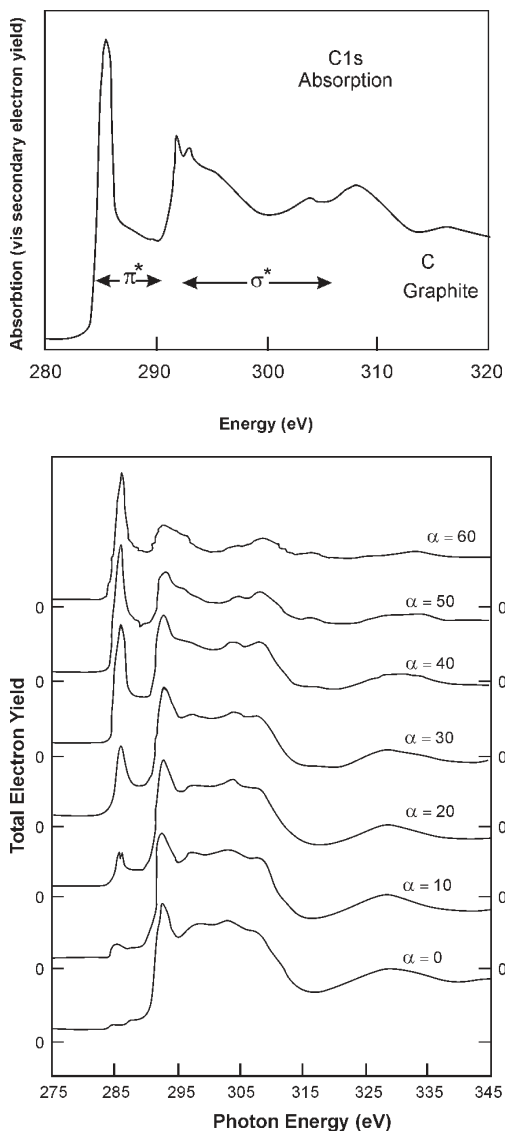
However, the spectra are complex and influenced by a number of factors other than the nature of the cation bonded to the oxygen. These include whether or not oxygen is bridging (BO) or non-bridging (NBO), the coordination geometry and nature of the cations to which the O is bonded, and the bond angles between the oxygen and surrounding cations. Consequently interpretation of O *K*-edge spectra is non-trivial and requires knowledge of the atomic structure of the sample, as well as, theoretical calculations. When O is bonded to only one other cation such as in simple oxides like $SiO_2$, $GeO_2$, or $Al_2O_3$ where the O atoms are all bridging and only attached to a single type of cation then the O *K*-edge spectra are relatively uncomplicated. However, the complexity is greatly increased when there are both NBOs and BOs, different $Q^n$ species and oxygen is bonded to more than one type of cation. This is seen in Figure 24a where in corundum the oxygen is bridging and attached to a single type of 6-fold aluminum, in berlinite the oxygen is also bridging but now shared between tetrahedral Al and P, while in $CaAl_2O_4$ there are three types of Ca (one 9- and two 7-fold sites) and O is shared between these and six Al sites in 4-fold coordination (Neuville et al. 2010). In general, transitions due to NBOs occur at slightly lower energy than transitions involving BOs because NBO bonds are shorter than BO and have higher electron density (Jiang 2002). In addition, the simulations of $CaAl_2O_4$ O *K*-edge spectra by Jiang (2002) suggest that as the Ca coordination increases, the peak associated with oxygen, shifts to lower energy by ~0.5 eV. Whether or not this is general behavior for O *K*-edge peaks as cation coordination changes, remains unresolved.

Furthermore, for O *K*-edge spectra there is also the possibility of forming beam-induced $O_2$ "defects" on the surface of the sample, particularly for data collected in TEY mode. These "defects" occur as a relatively intense sharp pre-edge peak around 533 eV (peak a in Fig. 24b). It is due to an O 1*s* transition to π* states of O-O bonds in $O_2$ molecules that have diffused to the surface (Jiang 2006; Jiang and Spence 2006).

When oxygen is associated with a transition metal in an octahedral environment, the O *K*-edge spectrum is strongly influenced by the unoccupied *d* orbitals of the transition metal. Consequently, O *K*-edge spectra are very similar across the first row transition metals. Figure 24c shows O *K*-edge spectra for rutile ($TiO_2$), anatase ($TiO_2$) and $Ti_2O_3$. They are similar to other studies (Brydson et al. 1987, 1989; de Groot et al. 1989; Ruus et al. 1997; Wu et al. 1997b). The spectra exhibit two prominent peaks at ~531.0 and 533.7 eV). These peaks arise from the transition of an oxygen 1*s* electron to O 2*p* σ* states that are hybridized with empty transition metal 3*d* orbitals (de Groot et al. 1989). The splitting into two peaks (labeled a and b) is due to $t_{2g}$-$e_g$ splitting of the 3*d* orbitals and the intensity is related to the degree of covalency between the oxygen atoms and the transition metal (de Groot et al. 1989). The second set of bands in the ~540-546 eV range are due to oxygen 1*s* transitions to O 2*p* states
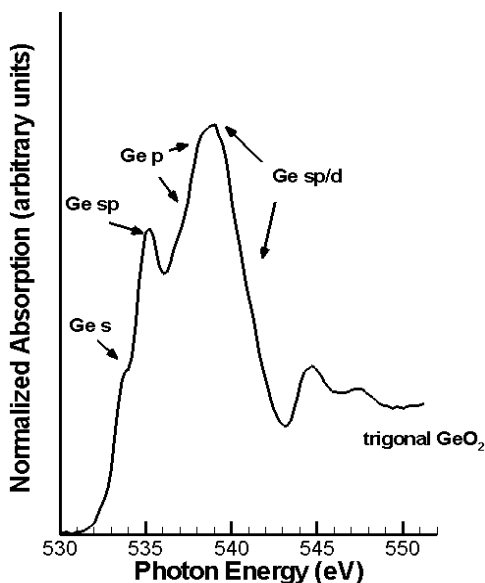


**Figure 23**. O *K*-edge spectrum of crystalline trigonal $GeO_2$ showing the peaks due to the O 1s → O 2*p* transition and the cation orbitals with which the O 2*p* state is hybridized/mixed (cf., Wang and Henderson 2004; Cabaret et al. 2007).
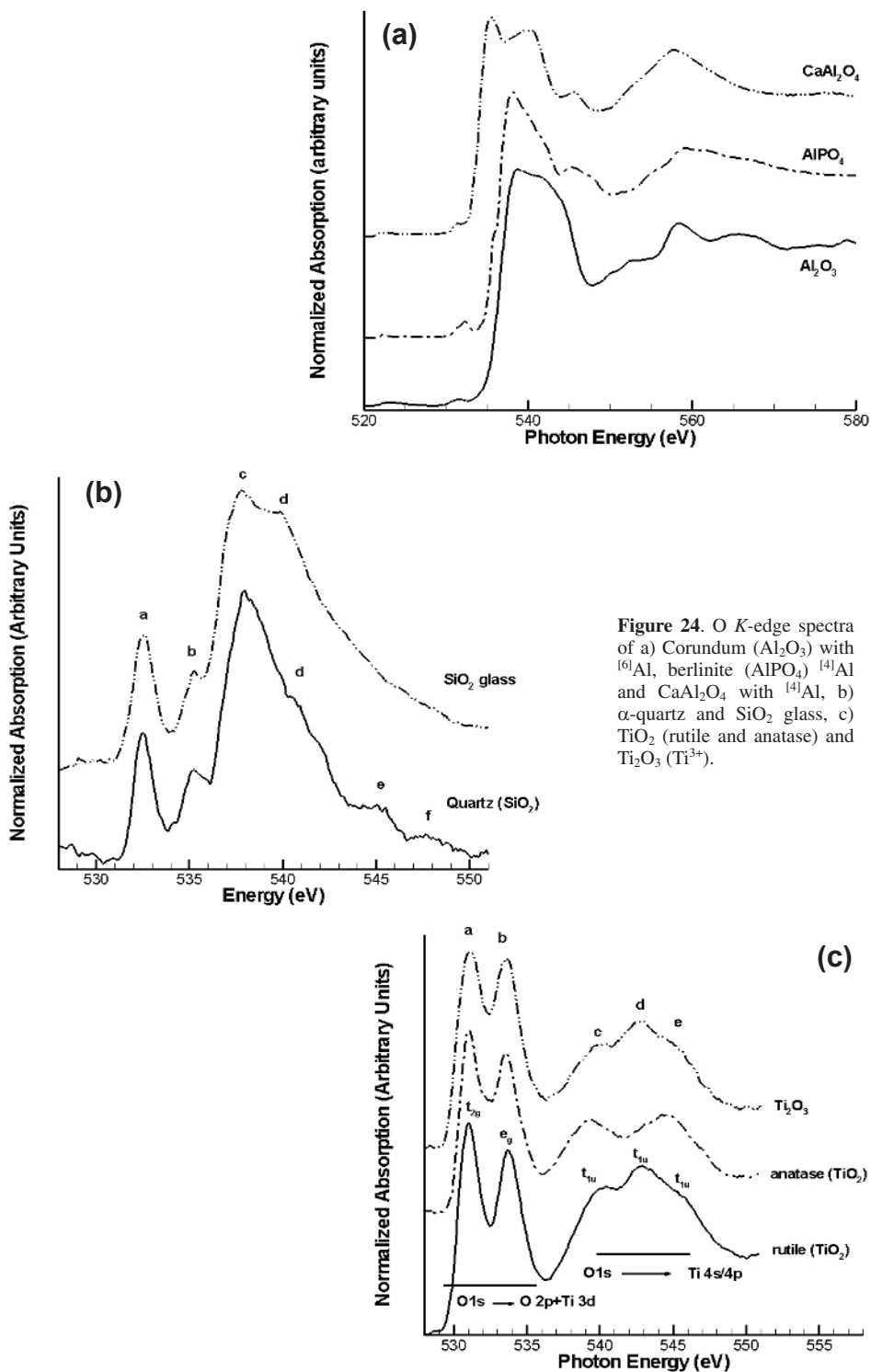
**Figure 24**. O *K*-edge spectra of a) Corundum (Al₂O₃) with [6]Al, berlinite (AlPO₄) [4]Al and CaAl₂O₄ with [4]Al, b) α-quartz and SiO₂ glass, c) TiO₂ (rutile and anatase) and Ti₂O₃ (Ti³⁺).

that are hybridized with transition metal $4s$ and $4p$ states (de Groot et al. 1989). Furthermore, the peaks in this region can be assigned to transitions to the lowest unoccupied $t_{iu}$ states (peaks c and d) and to higher lying $t_{iu}$ type orbitals (peak e) (Bydson et al. 1989). There is also a weak shift to higher energy of the O $K$-edge when the formal number of $d$-electrons increases on the Ti, i.e., when going from $Ti^{4+}$ to $Ti^{3+}$ (Yoshiya et al. 1999). When the transition metal is in 4- or 5-fold coordination similar mixing occurs but spectral interpretation is more complicated (Wu et al. 2002; Henderson et al. 2003) because of the $t_{2g}$-$e_g$ inversion (4-fold) and the loss of degeneracy of the $d$-orbitals (5-fold).

**Boron K-edge.** Interest in this edge (~195-210 eV) stems mainly from the potential use of borosilicate glasses in the encapsulation of high-level nuclear waste and the need to determine the B coordination in these materials (cf., Peuget et al. 2006, 2007). There have been several B $K$-edge XANES studies of borate and borosilicate minerals (Hallmeier et al. 1981; Brydson et al. 1988; Sauer et al. 1993; Li et al. 1995c, 1996; Garvie et al. 1995; Kasrai et al. 1998; Fleet and Muthupari 1999, 2000; Fleet and Liu 2001). In general, the spectra of $B_2O_3$ ([3]B), sassolite (B(OH)$_3$)([3]B), BPO$_4$ ([4]B) and danburite (Ca[B$_2$Si$_2$O$_8$]) ([4]B) are often used as reference spectra for interpreting other B containing phases (Fig. 25).
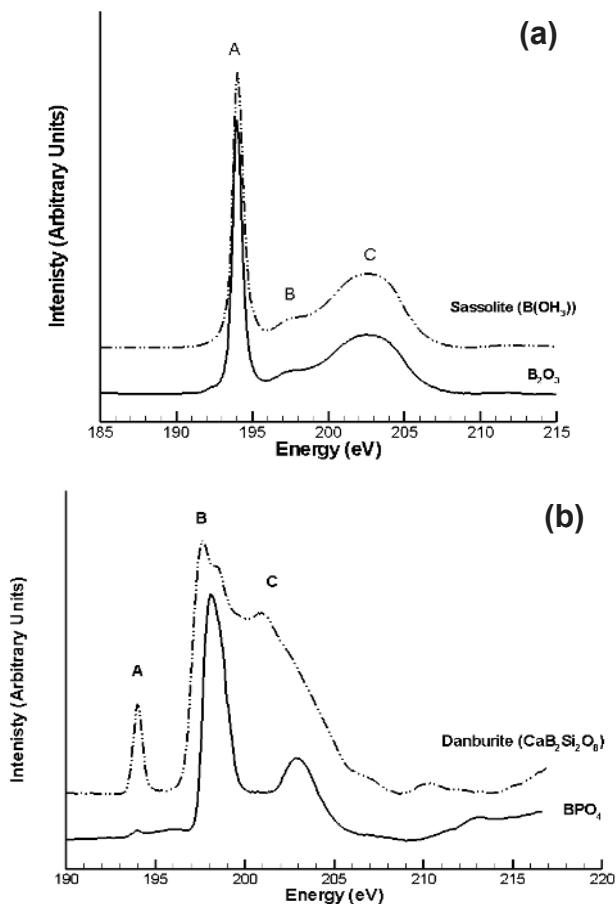


**Figure 25**. B $K$-edge XANES spectra of a) $B_2O_3$ and Sassolite (B(OH)$_3$) containing 100% [3]B and b) BPO$_4$ and danburite (Ca[B$_2$Si$_2$O$_8$]) containing nominal 100% [4]B.

In $B_2O_3$ (Fig. 25a) peak A is assigned to a [3]B transition from $1s \rightarrow 2p_z$ ($\pi$*) states, which project normal to the plane of $BO_3$ groups (Schwarz et al. 1983). A weak peak, B (around 197.5 eV) arises from a dipole-forbidden transition from [3]B $1s \rightarrow a_1'$ (B $3s$ + O $2s$ + O $2p$) ($\sigma$*) states (Ishiguro et al. 1982). $BO_3$ site distortion enhances this transition, due to the mixing of valence $2p$ $\pi$ or $\sigma$* antibonding and $2s$ states. The broad feature C around 198-205 eV consists of at least three distinct peaks at 200, 202 and 204 eV. They are assigned to transitions of B $1s$ electrons to unoccupied B-O sigma antibonding ($\sigma$*) orbitals of $e'$ (B $2p_x$ + B $2p_y$ + O $2s$ + O $2p$) symmetry, which are calculated to be ~10 eV above the B $2p_z$ orbital. Again Ishiguro et al. (1982) assign this peak to B $3p$ and $4p$ rather than $2p$ interactions.

For the $BPO_4$ and danburite spectra (Fig. 25b) in which only [4]B should be present, we can assign the peaks to transitions of B $1s$ electrons to unoccupied sigma antibonding (*$\sigma$) states of $t_2$ (B $2p$ + O $2p$) symmetry (peaks around 198 eV) and $a_1$ (B $2s$ + O $2p$) symmetry (peak at 200 eV) while the broad feature (labeled C in Fig. 25) may be assigned to transitions of B $1s$ electrons to the unoccupied $\sigma$ * orbitals of $a_1$ and $t_2$ symmetry (Schwarz et al. 1983; Sauer et al. 1993; Garvie et al.1995). However, distortion of $BO_4$ tetrahedra may result in loss of degeneracy of the $\sigma$* ($t_2$) orbital and peak broadening (Schwarz et al. 1983; Garvie et al. 1995; Fleet and Muthupari 1999, 2000) may occur which is observed as a shoulder at 199 eV on the high-energy side of the main peak.

Recent first principles calculations of the p-DOS have been carried out for crystalline $B_2O_3$, and $BPO_4$ (Ferlat et al. to be published). They show that some of the intensity of the main peak at 194 eV for $B_2O_3$ is also due to mixing with O $2p$ states while in the higher energy region (198-205 eV) the strongest contributor is a B $1s \rightarrow 2p$ transition at ~ 203-204 eV. At lower energy (198-200 eV) there are strong contributions from B $2s$ and B second neighbor $2p$ and $3p$ transitions while to the high energy side of the broad envelope second neighbor B $2s$ transition are the major contributors to the intensity. Simulations for $BPO_4$ show that the slight asymmetry of the peak at ~197 eV to the high energy side is due to a contribution from B $2s$ states and the high energy peak at ~202-205 eV results from contributions primarily from second neighbor P $3p$ interactions along with lesser contributions from B $2p/3p$ interactions.

***Boron -- effects of sample preparation.*** Spectra for compounds with nominal 100% [4]B often exhibit a sharp peak at 194 eV characteristic of [3]B. Earlier studies attributed this to the conversion of [4]B to [3]B by the X-ray beam or to reaction of the sample with OH (Sauer et al. 1993; Garvie and Buseck 1996) during sample preparation. Certainly for ELNES studies possible beam induced conversion may be likely, given the highly focused nature of the beam. Kasrai et al. (1998) considered that the [4]B transformed to [3]B when samples were crushed and ground and that mechanical disruption was the major source of the conversion. This suggestion is supported by the results shown in Figure 26 in which the B $K$-edge spectrum of a danbu-
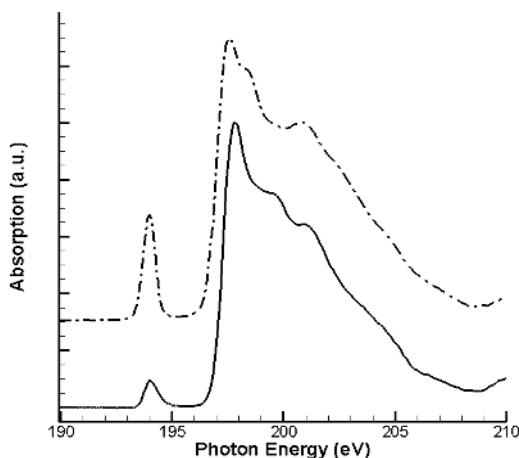


**Figure 26**. B $K$-edge XANES spectra of Danburite collected after different preparation conditions: crushed and under $N_2$ (*upper*); crushed fragments with a "fresh" surface exposed immediately prior to insertion in the sample chamber (*lower*).

rite sample has been collected under different experimental conditions. There is a significant difference between a sample crushed and ground in $N_2$ versus the same sample just crushed and not ground in $N_2$. The conversion is most likely a result of the increased surface area of the ground sample, with [3]B forming at the expense of [4]B simply because at the surface of the particles the planar $BO_3$ unit is likely to be geometrically preferred.

Representative spectra of minerals nominally containing only [3]B, only [4]B and mixed [3/4]B are shown in Figure 27 and their compositions given in Table 1. In the nominal 100% [4]B minerals a sharp feature characteristic of [3]B (peak A) can be seen at ~194 eV because all of the samples were ground prior to data collection. This peak may exhibit subtle asymmetry in some [3]B and mixed [3/4]phases although it is more prevalent in the [3]B only phases. Fleet and Muthupari (2000) attributed this to distortion of the $BX_3$ (where X = O, OH) group. However, Dong et al. (to be published) suggest it occurs due to separation of the B $2p$ and O $2p$ contributions to this peak. One should also note the high degree of variation in the intensity and

**Table 1.** Formulae of minerals shown in Figure 27.

| Mineral | Formula |
|---|---|
| **Minerals with only trigonal B** | |
| Sassolite | $[B(OH)_3]$ |
| Sussexite | $Mn_2(OH)[B_2O_4(OH)]$ |
| Szaibelyite | $Mg_2(OH)[B_2O_4(OH)]$ |
| Vonsenite | $Fe_2Fe^{3+}O_2(BO_3)$ |
| Warwickite | $(Mg,Ti,Fe^{3+},Al)_2O(BO_3)$ |
| **Minerals with both trigonal and tetrahedral B** | |
| Colemanite | $Ca[B_3O_4(OH)_3](H_2O)$ |
| Hydroboracite | $CaMg[B_3O_4(OH)_3]_2(H_2O)_3$ |
| Inyoite | $Ca[B_3O_3(OH)_5](H_2O)_4$ |
| Inderite | $Mg[B_3O_3(OH)_5](H_2O)_5$ |
| Kurnakovite | $Mg[B_3O_3(OH)_5](H_2O)_5$ |
| Howlite | $Ca_2B_5SiO_9(OH)_5$ |
| Boracite (low) | $Mg_3[B_3O_{10}]_2(BO_3)Cl$ |
| **Minerals with only tetrahedral B** | |
| Datolite | $CaBSiO_4(OH)$ |
| Pinnoite | $Mg[B_2O(OH)_6]$ |
| Reedmergnerite | $Na[BSi_3O_8]$ |
| Searlesit | $NaBSi_2O_5(OH)_2$ |
| Serendibite | $Ca_2(Mg,Fe^{2+})_3(Al,Fe^{3+})_{4.5}B_{1.5}Si_3O_{23}$ |
| Sinhalite | $AlMg(BO_4)$ |

positions of peaks B and C in all three groups of spectra. The overlap of peak B in the [3]B spectra at ~198 eV with peak B in the [4]B phases will lead to complications with extraction of quantitative B coordination numbers (see below). In addition, Fleet and Liu (2001) curve fit the spectral envelope in the 195-215 eV range in mixed [4]B mineral phases and noted a correlation between splitting of the fitted B peak and divergence of tetrahedral B-O bond length. However, Dong et al. (to be published) do not observe this.

Fleet and Muthupari (2000) also noted a correlation between the position of the [3]B peak at ~194 eV and the B-O bond length. They observed that the peak shifted to lower energy as the B-O bond length increased. This correlation is observed for minerals containing only [3]B (Fig. 28a, squares) but is less certain in minerals containing both coordination states (cf., Fig. 28a triangles). Dong et al. (to be published) speculate that it is related to more effective binding of the photoelectron to the nucleus due to the shorter B-O bond. In addition, there is a correlation between the position of the 194 eV peak and the increasing complexity of the B linkages (Fleet and Muthupari 2000; Dong et al. unpublished data) due to increasing positive charge on the B atom (Fleet and Muthupari 2000).

***Determining the [3]B/[4]B ratio.*** Sauer et al. (1993) noted that the spectra of [3]B is dominated by a sharp peak at ~194 eV and that of [4]B by a relatively sharp peak at ~199 eV. They also suggested that spectra of mixed [3/4]B phases were essentially the sum of the
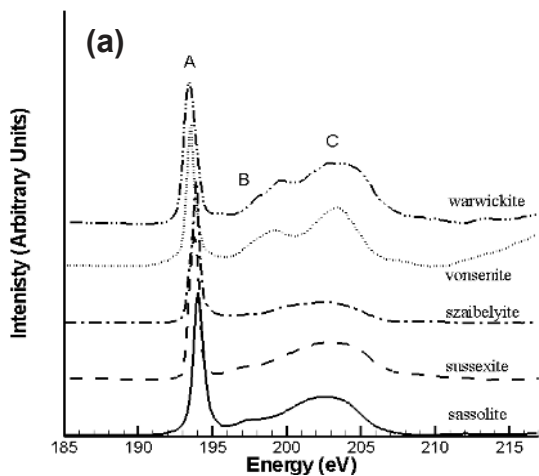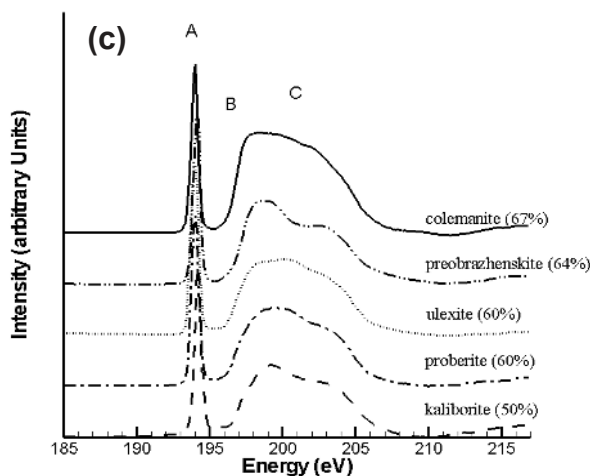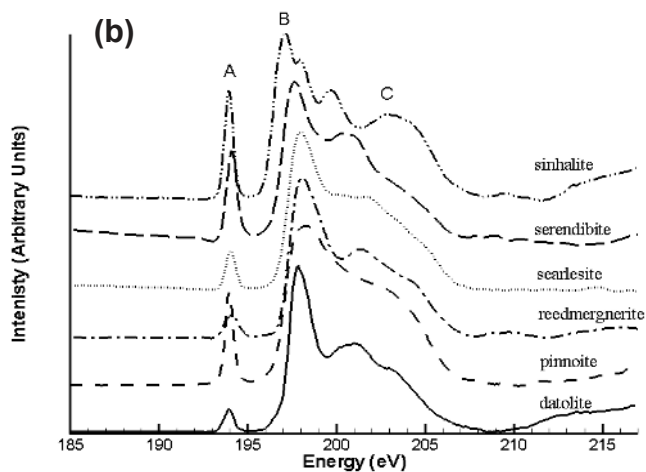
**Figure 27**. Representative spectra of minerals nominally containing a) 100% [3]B, b) 100% [4]B and c) mixed [3]B and [4]B (classified by nominal [4]B percentage).

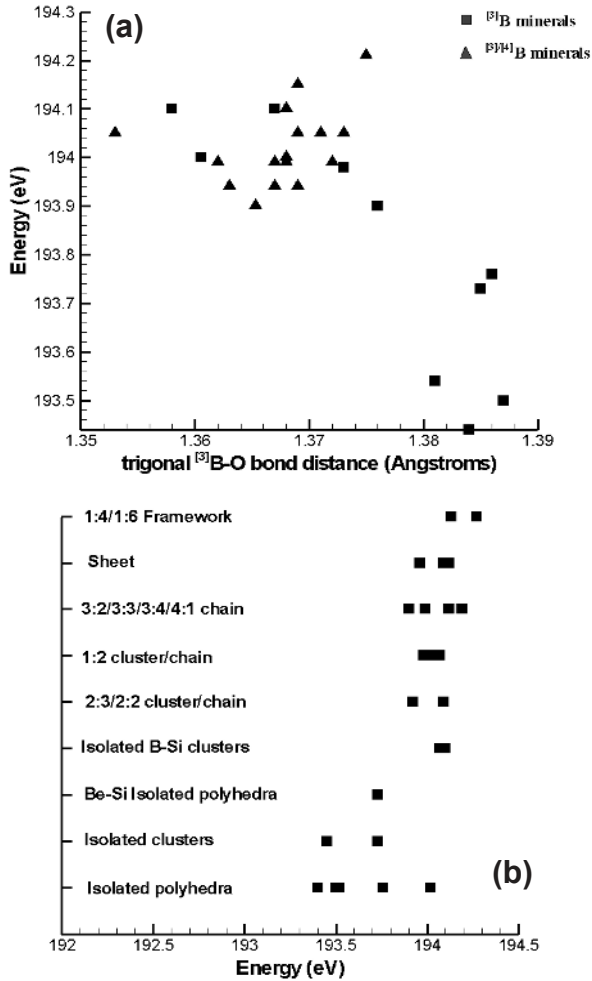**Figure 28**. Correlation between position of the [3]B peak at ~194eV versus a) average B-O bond length and b) on the extended structure of the BX$_3$ (where X =O,OH) group in borate and borosilicate minerals containing only [3]B or [3]/[4]B.

individual [3]B and [4]B spectra and consequently quantitative [3]/[4]B ratios could be determined by a simple integration of the intensities of peaks characteristic of [3]B via the following equation;

$$f_{tri} = \frac{J(\pi^*)/(J(\Delta E))}{[J(\pi^*)/(J(\Delta E))]_{ref}} \tag{1}$$

Where $f_{tri}$ is the fraction of [3]B in an unknown, $J(\pi^*)$ and $J(\pi^*)_{ref}$ are the intensities of the $\pi^*$ peaks (~194 eV) of the unknown, and a reference material containing 100% [3]B, $J(\Delta E)$ and $J(\Delta E)_{ref}$ are the integrated intensities in the energy window $\Delta E$ (~18-20 eV) above the respective B $K$-edges. This method has also been used by Garvie et al. (1995) and Fleet and Muthupari (2000), with some slight modification of the energy windows. Fleet and Muthupari (2000) noted that the area and position of the peak due to [3]B at ~194 eV was sensitive to the [3]B

content and the B-O bond length. In addition, the area of the peak assigned to [4]B at ~ 198 eV was also sensitive to concentration of [4]B but quantification was difficult because of overlap with the broad feature at 203-204 eV due to both [3]B and [4]B. This latter overlap makes accurate determination of the relative coordination numbers somewhat problematic. Figure 29 shows a plot of calculated versus nominal [3]B concentration in mixed coordination phases. It is clear that this method underestimates the proportion of [3]B at high [3]B contents and overestimates it at low [3]B contents.

Borate and borosilicate minerals may also form superstructural units (cf., Hawthorne et al. 1996). Sipr et al. (2007) have
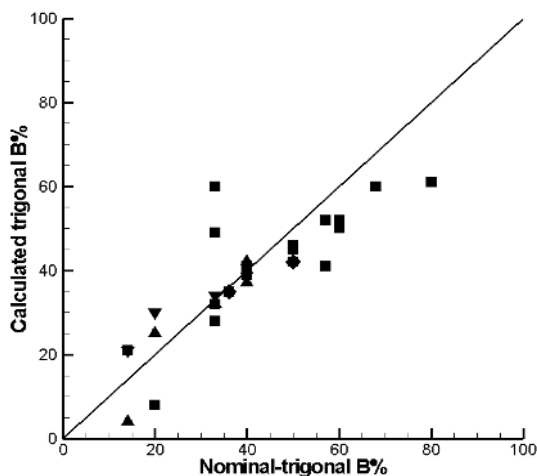


**Figure 29**. Proportion of [3]B calculated using the total area method: squares (Dong et al. unpublished data), triangles (Fleet and Muthupari 2000), gradient (Sauer et al. 1993), diamonds (Garvie et al. 1995).

investigated theoretically, the influence of superstructural units on the XANES spectra of B-containing minerals. They note that spectra of minerals containing boroxyl rings, diborate and tridiborate units differ from a simple superposition of spectra containing isolated [3]B and [4]B units as opposed to spectra of structures containing pentaborate and triborate units. They find that boroxyl ring structures should be recognized by a small sub peak ~25 eV above the edge while diborate and ditriborate units will produce "fine structure" around the main XANES peak (cf., Sipr et al. 2007; Sipr and Rocca 2010).

*Sulfur K-edge.* Recent reviews of sulfur XANES have been given by Fleet (2005) and Wilke et al. (2011) and references therein. Sulfur is a ubiquitous volatile element in the Earth that occurs naturally in a wide variety of oxidation states from 2− to 6+ and consequently the sulfur $K$-edge (~2460-24520 eV) can vary by up to 12 eV in energy (Li et al. 1995d; Fleet 2005; Fleet et al. 2005; Almkvist et al. 2010). The two most common oxidation states for sulfur in solids of earth systems are oxidized $S^{6+}$ (sulfate oxy-anion; $SO_4^{2-}$) and reduced $S^{2-}$ (sulfide) (Fig. 30). The S $K$-edge of sulfur found as sulfate, such as in gypsum ($CaSO_4 \cdot 2H_2O$), displays a sharp feature at 2482 eV due to core level transitions of a $1s$ electron to the $t_2$ ($3p$-like) anti-bonding orbitals (Li et al. 1995d). This peak is found in other sulfates including $MgSO_4 \cdot 2H_2O$, $K_2SO_4$, $Na_2SO_4$, anhydrite, celestite, barite and hauyn (Li et al. 1995d; Wilke et al. 2008; Alonso Mori et al. 2009; Klimm et al. 2012). The peak is relatively sharp due to the narrow S-O bond distribution in the $SO_4^{2+}$ groups. Higher energy peaks within sulfate spectra are attributed to multiple scattering by nearest- and NNN.

In contrast, monosulfide minerals (Fig. 31) show greater variation in edge position and intensity due to the meta-sulfide bond covalency (or ionicity), as well as, the degree of site distortion. Farrell et al. (2002) have studied monosulfide solid solutions in Fe-Mn-Mg sulfide system and CaS. A pre-edge feature (peak a) shifts to higher energy in the order FeS (2469.9 eV), MnS (2471.0 eV), CaS (2473.8 eV) while it is absent in the MgS spectra. The peak results from excitation of a $1s$ electron to unoccupied $3d$ antibonding states which is allowed due to hybridization of the metal $3d$ electrons with the S $3p$ $\sigma$* antibonding states (Tossell 1977). It is strongest in iron sulfides, due to the presence of unoccupied $e_g$ orbitals (Farrell
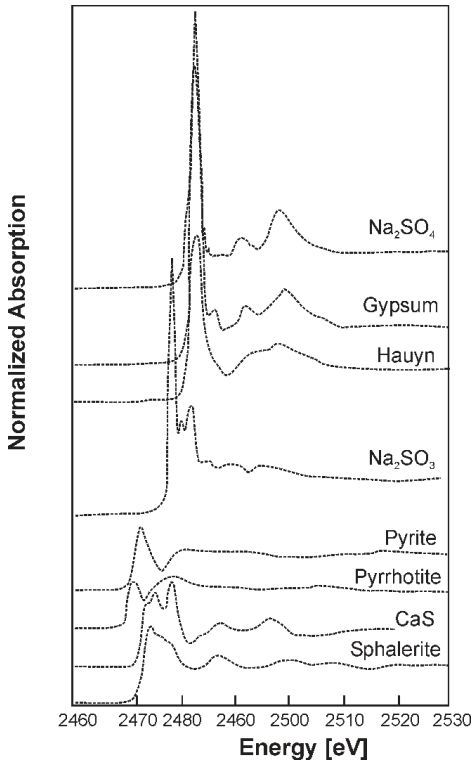
**Figure 30**. Compilation of S *K*-edge XANES of sulfur compounds with varying S oxidation state, (after Wilke et al. 2011).
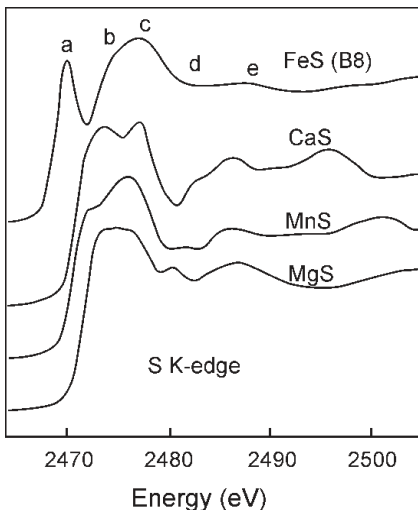


**Figure 31**. S K-edge spectra after Farrell et al. (2002) showing the effect of filling the *3p* like anti-bonding states.

and Fleet 2001; Farrell et al. 2002), and weakest in CaS, due low-lying Ca 3*d* antibonding orbitals that reduce the band gap (Stepanyuk et al. 1989; Farrell et al. 2002). MgS has no low-lying metal 3*d* ($e_g$) orbitals available to hybridize with the S antibonding states and consequently exhibits no pre-edge feature. Farrell et al. (2002) attribute peaks b and c to 1*s* to 3*p* σ* antibonding states hybridized with Fe 4*s* and 4*p* σ* antibonding states in the conduction band. Furthermore they conclude that the relative intensity of peaks b and c are proportional to the available unoccupied $t_{2g}$-like and $e_g$-like antibonding orbitals, as well as, to the degree of hybridization between 3*p* σ* antibonding and 4*s* and 4*p* σ* antibonding states. Finally peaks at higher energies (approx. >2480 eV) have been assigned to multiple scattering.

The spectra of FeS, NiS and CoS have been simulated by Soldatov et al. (2004) using multiple-scattering codes. The simulations reproduce the experimental spectra reasonably well when a core hole bandwidth of 0.59 eV is taken into account and clusters of sufficient size are used. In both, experimental and calculated spectra all three peaks show a progressive shift to higher energies and higher intensity in the order FeS - NiS - CoS consistent with the $1/R^2$ rule (see above). The lattice parameters a and c decrease from FeS to CoS and consequently peaks b and c increase in energy in these spectra.

While in most mineral phases the sulfur is present as either $S^{6+}$ or $S^{2-}$ recent studies on silicate glasses from ocean island basalts (e.g., Loihi Seamount) and from synthesis at high pressure and temperature have shown evidence for the co-existence of both sulfide and sulfate species (Jugo et al. 2010). From these observations on mixed S-species in glasses the following relationship was derived to calculate the proportion of $S^{6+}$ in the total sulfur content:

$$\frac{S^{6+}}{\sum S} = -C\ln\left\{\frac{\left[\left[I(S^{6+})/\sum I - A\right]\right]}{B}\right\}$$

where $A$, $B$ and $C$ are the coefficients 1.2427, $-0.94911$ and 0.81354, respectively and $\Sigma I = I(S^{6+}) + I(S^{2-})$ where $I(S^{2-})$ is the integrated intensity over the region 2475.7-2480 eV and $I(S^{6+})$ is the integrated intensity over the region 2481.5-2484 eV (Jugo et al. 2010). This relationship has been calibrated for a variety of synthetic glasses and fit parameters are dependent on the integrated area of the spectra and the regions defined as either sulfide or sulfate. This model works well for sulfur in silicate glasses as the edge position of sulfate is constant and the edge for sulfide does vary only in a limited range. Wilke et al. (2011) note that relationship varies depending on the composition of the glass, mostly due the variability of the spectra for the sulfide species. More discussion regarding the quantification of sulfur species can be found in Jugo et al. (2010), Wilke et al. (2011) and Klimm et al. (2012).

Finally, in early studies of S in silicate melts many authors report $S^{4+}$. However Wilke et al. (2008) have shown that this is an artifact of beam damage during XANES or electron microprobe analysis. Recently, Klimm et al. (2012) noted that beam damage is more important for iron-free melts than their iron-bearing counterparts. Although $S^{4+}$ (as sulfite) is unlikely to be a common species in magmatic systems it may be important in other geochemical environments, particularly in vapor and fluids as $SO_2$. In solids, the sulfite oxy-anion, as found in $Na_2SO_3$, is in trigonal pyramidal geometry and the S $K$-edge is at 2478 eV (Alonso Mori et al. 2009; Almkvist et al. 2010).

Alonso Mori et al. (2009) have carried out a number of *ab initio* calculations of the S $K$-edge using multiple scattering, density functional theory and atomic multiplet theory. They compared their calculations with experimental data collected on sulfides ($S^{2-}$), sulfites ($S^{4+}$) and sulfates ($S^{6+}$). They found that the number, position and intensity of the experimental peaks depend primarily on the nature of the S first neighbors although next-nearest neighbors could also play a role. The main edge in sulfates and sulfites was due to a transition of the S $1s$ core electron to the $3p$-like lowest unoccupied level that also has an O $2p$ component and some S $3d$ contribution. However, the main edge of sulfite occurs at lower energy than that of sulfates. For sulfides, the energy of the main edge shifts to lower energy from Zn to Cd and Hg. This is due to increased hybridization from the cation d orbitals. Overall there is ~12 eV energy shift in the edge on going from sulfides to sulfates and this edge shift is characteristic of the S oxidation state in oxycompounds but much less so for sulfides where the S atom is directly bound to the metal cations.

**S $L_{2,3}$-edge.** Sulfur $L_{2,3}$-edge (~160-200 eV) has been reviewed by Chen (1997) and Fleet (2005). The $L$-edge has not been as widely applied as the $K$-edge because the spectra are more complex than the S $K$-edge due to increased contributions from hybridized anti-bonding states (see below), they tend to have low signal to noise and are surface sensitive due to the low penetration depth of soft X-rays.

Sulfate $L$-edge spectra are simpler to interpret than sulfide spectra. Li et al. (1995d) obtained S $L_{2,3}$-edge spectra of typical sulfate minerals (Fig. 32). There is a distinct edge feature lying between 170.2-171.2 eV that exhibits splitting due to LS coupling resulting in the $L_2$ and $L_3$ doublet separated by ~1.2 eV (Fleet 2005). In gypsum, Li et al. (1995d) have assigned a S $2p_{3/2} \rightarrow a_1$ ($3s$-like) transition to the edge shoulder at 170.3 eV (peak $A_1$) and the S $2p_{1/2} \rightarrow a_1$ ($3s$-like) to the edge maximum at 171.3 eV (peak $A_2$). In addition to the edge doublet there is clearly a shoulder at higher energy, peak C, as well as an intense peak (E) centered at ~180 eV. Li et al. (1995d) have assigned peaks C and E to S $2p$ to $t_2$ and $e$ transitions, respectively, though this interpretation has been questioned as it simplifies the hybridized nature of these higher energy contributions (Chen 1997; Farrell et al. 2002; Fleet 2005).
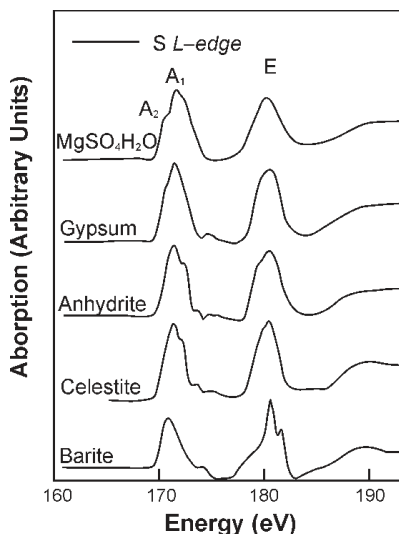
**Figure 32.** S *L*-edge spectra of simple sulfate minerals (after Li et al. 1995d).



**Figure 33**. S L-edge spectra showing the strong LS doublet at ~162-163 eV (after Kasrai et al. 1996a).

The LS doublet is more distinct but lower in intensity than the post-edge features in sulfide minerals. For example, both native sulfur (S$^0$) and pyrite (S$^{1-}$) have a doublet at approximately the same position: 162.7 and 163.9 eV for sulfur versus 162.4 and 163.5 eV for pyrite (Fig. 33) (Kasrai et al. 1996a). For organic sulfur-bearing compounds (e.g., disulfides, alkyl sulfides, aryl sulfides and thiophenes) the S $L_{2,3}$-edge spectra of Sarret et al. (1999, 2002) exhibit at least three separate prominent peaks starting at ~163-164.5 eV separated by about 2 eV. These peaks strongly correlate with those found in thiophene have been used in characterizing unknown kerogens through linear combination fitting, however discrepancies still remain (Sarret et al. 2002).

A second doublet is also observed in the S $L_{2,3}$-edge in the spectra of pyrite and native sulfur (peaks 5 and 6 in Fig. 33) (Kasrai et al. 1996a). This doublet has also been recorded by Farrell et al. (2002) for CaS. The origin of this second doublet is currently attributed to an "echo" or shadow effect of the LS doublet due to multiple scattering or a transition to localized levels higher in the conduction band (Farrell et al. 2002). Earlier work by Kasrai et al. (1988) used peaks 10-45 eV above the edge to evaluate interatomic distances using the 1/$R^2$ rule. They found a strong correlation for PbS, ZnS and MoS$_2$. Fleet (2005) further discussed the 1/$R^2$ rule as applied to galena, PbS, correlating energy with interatomic distance for peaks down to 11 eV above the main edge feature.

Simulations of the S $L_{2,3}$-edge of FeS, NiS and CoS have been performed by Soldatov et al. (2004) using multiple-scattering theory. Their results reproduce the positions of the pre-edge, the edge and two higher energy peaks however, the peak-to-background ratios are not in
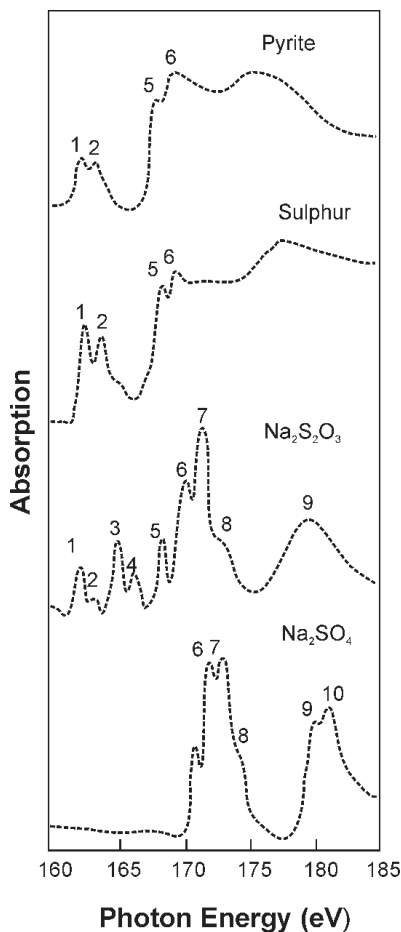
agreement with experiment. Moreover, the pre-edge feature is much stronger in the calculated spectra than in the experimental data. Nevertheless the simulations do show the shift to higher energy, FeS → CoS in order of decreasing lattice spacing as observed experimentally. Soldatov et al. (2004) calculate the density of states of CoS and NiS and observe a "'normal" hybridization between Ni $d$ and the S $p$ unoccupied states, as well as, a second hybridization where the S $p$ states are repulsed away from the Ni $d$ states. Soldatov et al. (2004) note that this phenomenon has been previously reported for rare earth sulfides (Soldatov and Gusatinskii 1984), $CeO_2$ (Soldatov et al. 1994), orthoferrite (Povahzynaja et al. 1995), and stishovite (Soldatov et al. 2000). Finally, they use this energy separation as a measure of the covalency of the bonding in sulfide minerals concluding that NiS bonds are the most covalent in character and FeS are the least covalent (Soldatov et al. 2004).

*Phosphorous.* Phosphorous is an essential nutrient in the Earth's biosphere as well as an incompatible element in most magmatic and hydrological processes. It has a variety of oxidation states between $P^0$, in its elemental form, and $P^{5+}$ as $(PO_4)^{3-}$. In nature, it is almost always found as the latter. Industrially, phosphate minerals are crucial components in fertilizers and phosphate minerals in rocks are often a major sink for rare-earth elements. P $K$-edge XANES has been applied to studies of phosphate minerals (Okude et al. 1999; Ingall et al. 2011), phosphate glasses (Yin et al. 1995; Nicholls et al. 2004); and soils (Beauchemin et al. 2003; Prietzel et al. 2010 and references therein; Kar et al. 2011; Xiong et al. 2012). On the other hand, a substantial amount of P $L$-edge data comes from the thin film and tribology literature where phosphorous and sulfur are key ingredients in lubricants (Kasrai et al. 2003; Nicholls et al. 2007 and references therein). Recently Kruse et al. (2009) have reviewed the phosphorous $L_{2,3}$-edge XANES of a number of commonly used crystalline and organic reference compounds.

*Phosphorous K-edge.* The position of the P K edge (~2140-2190 eV) can shift by ~ 8 eV (Prietzel et al. 2010) depending upon oxidation state (higher energy with increasing oxidation) and is affected by the nature of the ligand attached to the P. The edge shifts to higher energy with increasing ligand electronegativity (Yin et al. 1995). Thus ligand bonding has a strong effect on edge position similar to the cation effect in sulfide minerals (see above). Therefore, when using standards to determine oxidation state, it is important to use standards of the same ligand type (e.g., oxide-bearing or sulfur-bearing) not only similar oxidation state.

P $K$-edge spectra for several compounds are shown in Figure 34. Each spectrum has a sharp edge feature (peak 1) as well as two to three higher energy peaks The sharp edge in all spectra is attributed to a $1s$ core level to the $t_2^*$ ($p$-like) anti-bonding orbitals (Yin et al. 1995). They attributed peaks 2-4 to shape resonances or multiple scattering. The main edge shifts to higher energies with the ligand: from C→S→O (Yin et al. 1995).

A range of phosphate minerals have been investigated by Ingall et al. (2011) at the P $K$-edge and are shown in Figure 35. The 12 apatite specimens all show similar spectral features despite varying carbon, hydroxyl and fluorine contents. A sharp edge peak is centered at 2155.6 eV with a high energy shoulder at (~2157 eV) that is approximately half to a third the intensity of the main edge, and two higher energy peaks centered at 2163.3 eV and 2170 eV. The edge is assigned to a transition of a $1s$ electron to the $t_2^*$ ($p$-like) anti-bonding orbital. Non-apatite calcium-poor phosphate minerals (e.g., whiteite) display sharp edge features between 2153.0 and 2154.0 eV. The non-apatite calcium phosphates have lower intensity edge shoulders and a range of post-edge peaks. Aluminum-bearing phosphate minerals display no shoulder on the main edge and as a result have the narrowest edge (FWHM around 0.9 eV). Oxidized iron- and manganese-bearing phosphates display a unique pre-edge feature at 2150.1 eV associated with the presence of oxidized iron ($Fe^{3+}$). A single pre-edge feature is also observed in the spectra of chromium and cobalt phosphate minerals (Okude et al. 1999) and the copper-bearing phosphate, cornetite (Ingall et al. 2011). Xenotime has five sharp peaks that are attributed
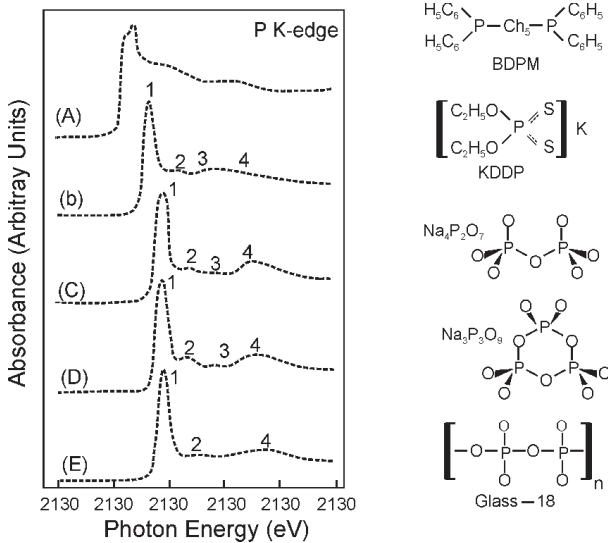
**Figure 34.** P *K*-edge XANES (*left*) of P bound to different ligands (*right*) (after Yin et al. 1995).

to interactions between phosphate and the outer orbitals of group 3 elements. Finally, Ingall et al. (2011) also note that pyromorphite and the uranium-bearing phosphates (e.g., coconinoite, meta-autunite) have a distinctive pre-edge doublet feature (~2151 and ~2152 eV). Thus the P *K*-edge of these general mineral groups may be used to constrain the contents of unknown mineral samples via "fingerprinting" and linear combination modeling.

*Phosphorous L-edge.* The $L_{2,3}$-edge (~130-155 eV) is comprised of the LS coupled doublet at ~134.5-137.5 and 136-141 eV (Fig. 36) corresponding respectively to the $2p_{1/2}$ and $2p_{3/2} \rightarrow a^*_1$ transitions (Yin et al. 1995). The $L_{2,3}$ edge is generally insensitive to the chemical environment. A broad peak at ~138-139 eV, about 2 eV above the edge, can be assigned to a $1s \rightarrow 3p$ anti-bonding state transition similar to that of the Si *L*-edge (Harp et al. 1990; Kruse et al. 2009). A further peak at ~147 eV due to $2p$ to $3d$ transitions is sensitive to the molecular symmetry and local environment.

The separation between the LS doublet varies for different phosphorous-bearing phases (Kasrai et al. 1999; Varlot et al. 2001). Na- and K-bearing phosphates have similar spectral features to Ca- and Mg-bearing phosphates. When Fe (or other TM) is bound to the phosphate quadrupolar transitions become allowed and a pre-edge peak is observed.
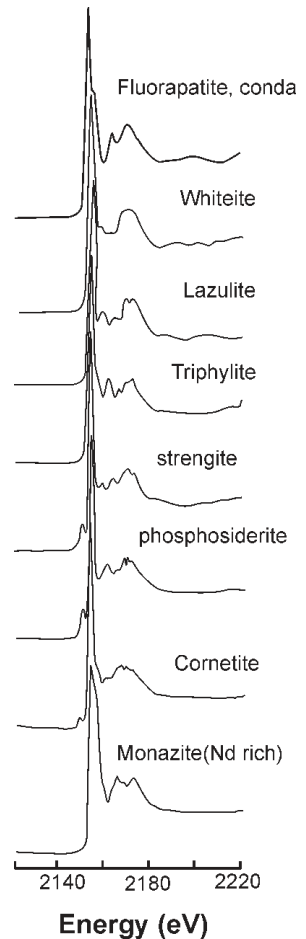


**Figure 35.** P *K*-edge spectra of selected phosphate minerals (after Ingall et al. 2011).
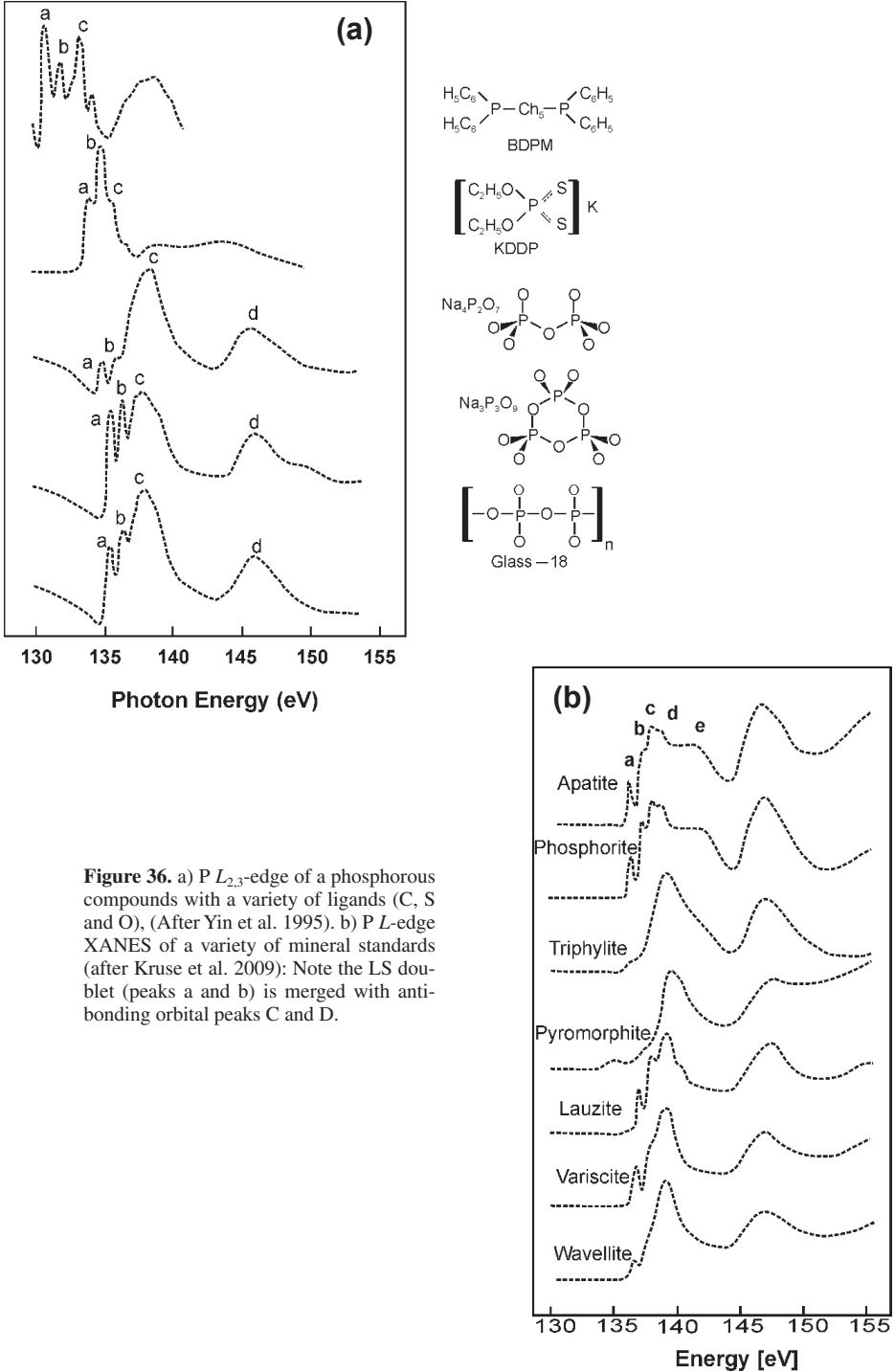
**Figure 36.** a) P $L_{2,3}$-edge of a phosphorous compounds with a variety of ligands (C, S and O), (After Yin et al. 1995). b) P $L$-edge XANES of a variety of mineral standards (after Kruse et al. 2009): Note the LS doublet (peaks a and b) is merged with antibonding orbital peaks C and D.

## SOME EXAMPLES OF STUDIES UTILIZING XANES

In the following section we highlight the use of XANES in more detail by discussing some recent studies.

### Assessing trace element substitution in minerals: Cerium speciation ($Ce^{3+}/Ce^{4+}$) in Ti-rich minerals

Titanite is a ubiquitous mineral that concentrates incompatible elements through incorporation of these elements into the large seven-fold site that holds $Fe^{2+}$ and the rare earth elements. King et al. (2013) determined the oxidation state of cerium (Ce) within two titanites (one green and one brown) using Ce $L_3$-edge (5723 eV) XANES. King et al. (2013) combine the oxidation state information with known ionic radii to evaluate possible substitution mechanisms for Ce in titanites. Their model evaluates favorable from unfavorable trace substitutions in the context of the lattice strain model (Brice 1975; Blundy and Wood 1994) arguing that favorable substitutions minimize the overall changes in combined ionic radii and valence (King et al. 2013). King et al. (2013) used $Ce^{3+}$ ($CePO_4$) and $Ce^{4+}$ ($CeO_2$) standards and used linear combination fitting to determine the $Ce^{3+/4+}$ ratio needed to evaluate their substitution model. The green titanite was calculated to contain 71% of Ce in the 3+ oxidation state whereas the brown titanite contains 46% $Ce^{3+}$ (Fig. 37).
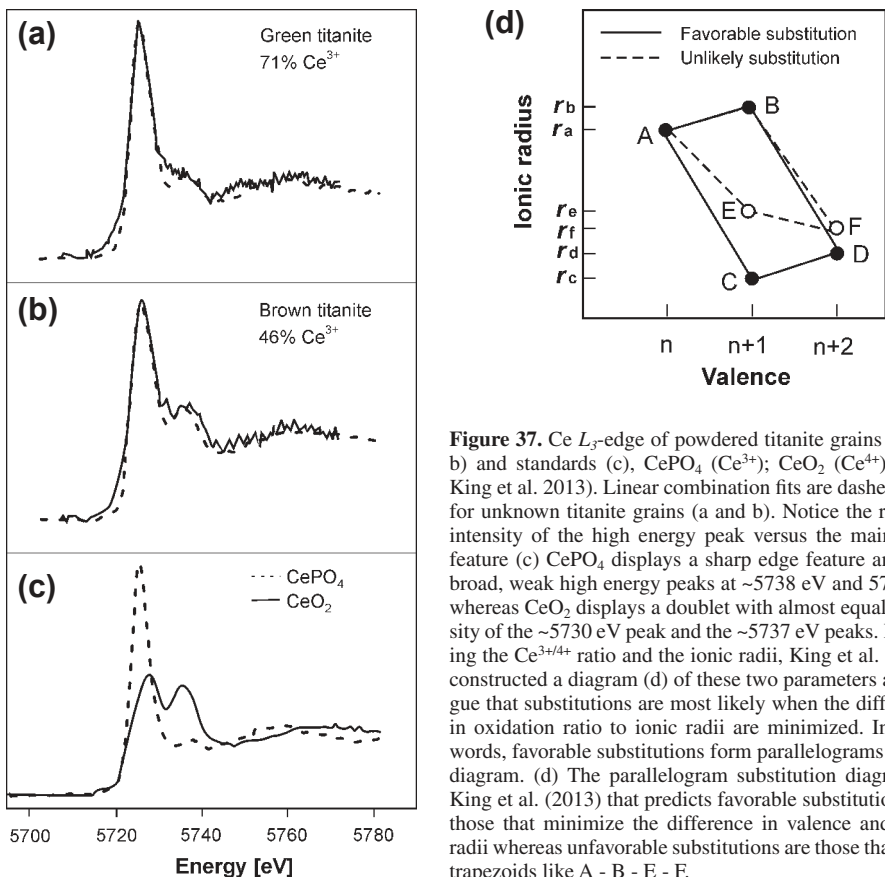


**Figure 37.** Ce $L_3$-edge of powdered titanite grains (a and b) and standards (c), $CePO_4$ ($Ce^{3+}$); $CeO_2$ ($Ce^{4+}$) (after King et al. 2013). Linear combination fits are dashed lines for unknown titanite grains (a and b). Notice the relative intensity of the high energy peak versus the main edge feature (c) $CePO_4$ displays a sharp edge feature and two broad, weak high energy peaks at ~5738 eV and 5758 eV whereas $CeO_2$ displays a doublet with almost equal intensity of the ~5730 eV peak and the ~5737 eV peaks. Knowing the $Ce^{3+/4+}$ ratio and the ionic radii, King et al. (2013) constructed a diagram (d) of these two parameters and argue that substitutions are most likely when the difference in oxidation ratio to ionic radii are minimized. In other words, favorable substitutions form parallelograms on the diagram. (d) The parallelogram substitution diagram of King et al. (2013) that predicts favorable substitutions are those that minimize the difference in valence and ionic radii whereas unfavorable substitutions are those that form trapezoids like A - B - E - F.

**Assessing changes in oxidation state of Nb and Ta with varying $f_{O_2}$ at 1.5 GPa as a possible explanation for the negative Nb/Ta anomaly or "arc signature" of melts**

Burnham et al. (2012) tested the hypotheses that the Nb-Ta anomlies that define the "arc signature" are related to oxidation state of the Nb or Ta. Both Nb and Ta are high field strength elements that are typically found in octahedral coordination, have a 5+ oxidation state and nearly identical ionic radii (0.69 and 0.68 Å). In this coordination Nb-Ta anomalies in arc magmas have an unknown source. The relative depletion of Nb and Ta has been shown to vary implying that these elements are capable of geochemical fractionation despite having the same charge and radii. One obvious explanation would be that the oxidation state varies with $f_{O_2}$, melt composition and pressure. Burnham et al. (2012) collected Nb *K*-edge (Fig. 38) and the Ta $L_3$-edge (Fig. 39) to observe the expected edge shift if differing oxidation states were present. However, the Nb *K*-edge and Ta $L_3$-edge show no major changes. The Ta $L_3$-edge position is consistent with the $Ta_2O_5$ standard ($Ta^{5+}$; 9983.06 eV) though there is a subtle splitting of the edge. The Nb *K*-edge is consistent with $Nb^{5+}$ standard edge position (18 991.0 eV) and only shows subtle changes in its pre-edge features. Clearly over a wide range of $f_{O_2}$'s at ambient and high pressures both Nb and Ta remain in the 5+ oxidation state and in the same structural environment. Ultimately, Burnham et al. (2012) conclude that the anomalous
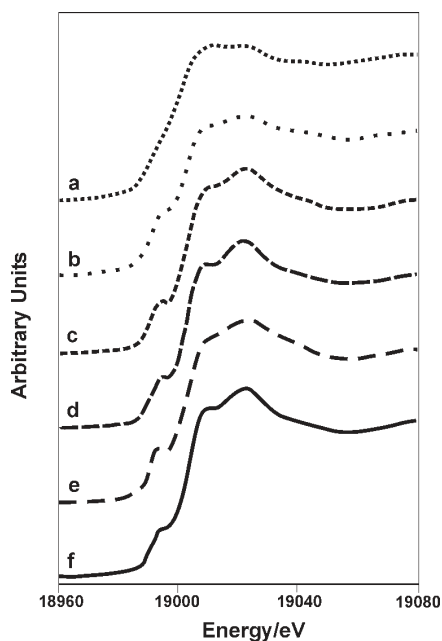


**Figure 38**. Nb *K*-edge spectra after Burnham et al. (2012). a) $NbO_2$ in BN. b-e) Overlain ambient pressure spectra of various compositions at end-member $f_{O_2}$'s; IW +6.7 and IW −4.3. f) Overlain 1.5 GPa spectra of compositions 1110 (IW-4.2) and 1111 (>>IW). See Burnham et al. (2012) for exact compositions. The identical edge positions across all $f_{O_2}$'s and across all compositions indicates constant oxidation state. Notice the subtle changes in pre-edge features.
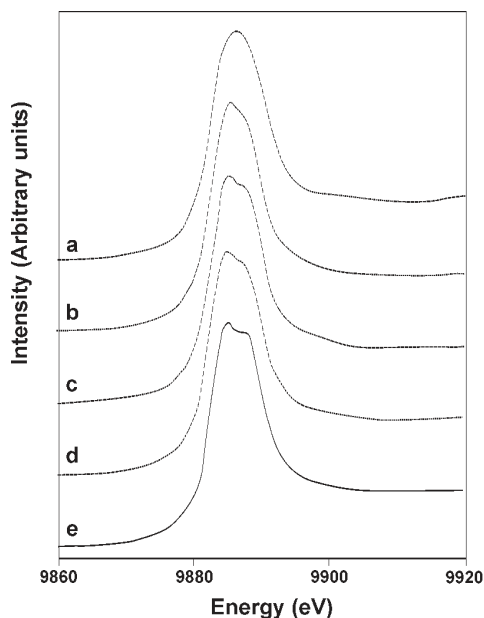
**Figure 39**. Ta $L_3$-edge spectra after Burnham et al. (2012). a) $Ta_2O_5$ in BN glass standard. b-d) Overlain ambient pressure spectra for various compositions at IW +6.7 and IW-3.3. e) Overlain 1.5 GPa pressure spectra for compositions 1110 (IW-4.2) and 1111 (>>IW). Notice the slight separation of the LS doublet with varying $SiO_2$ content and increasing pressure.

Ta-Nb "arc signature" is derived from partitioning due to small differences in ionic radii or polarizability.

### *In situ* high-temperature determination of Cr oxidation state in basaltic melts: A novel XANES furnace design

Berry et al. (2003b) developed a furnace design for carrying out *in situ* high temperature XANES experiments on melts to resolve Cr speciation within iron-bearing basaltic melts under controlled oxygen fugacity ($f_{O_2}$). This is crucial as iron-bearing melts always display $Cr^{3+}$ upon quenching samples because of the electron exchange reaction $Cr^{2+} + Fe^{3+} \rightarrow Fe^{2+} + Cr^{3+}$ during quenching. This quench effect in the presence of iron may be an important phenomenon for many other transition metals and redox sensitive elements. Moreover, models that involve the partitioning of redox sensitive elements between crystals and magmas are dependent upon the correct oxidation state assignment, which in turn is controlled by the $f_{O_2}$. Thus it is critical to constrain the oxidation state of elements under different $f_{O_2}$ at melt conditions rather than in the quenched products.

Under typical terrestrial oxidation conditions Cr occurs in both the 3+ and 2+ oxidation states in iron-free glasses, whereas in iron-bearing glasses only $Cr^{3+}$ has been observed. The controlled-atmosphere furnace uses a $Pt_{0.6}/Rh_{0.4}$ wire heater within an aluminum tube approximately 75 mm in diameter and 300 mm in length and which has two windows in a 90° configuration for the incident and fluorescent X-rays. A Pt/Re wire or strip is used to suspend the molten samples in the furnace, which are held to the strip by surface tension. The sample tube is kept slightly above atmospheric pressure. Cr *K*-edge spectra were collected using a focused beam of 2 mm × 1 mm on an alkali-free "model" mid-ocean ridge basalt which was pre-equilibrated at 1673 K and a log $f_{O_2}$ of −8 before being used in the controlled $f_{O_2}$ experiments under varying temperature conditions. The *in situ* spectra were compared with iron-free standards.

In iron-free glasses the $Cr^{3+}$ pre-edge feature arises from $1s \rightarrow 3d$ quadrupolar transitions (see above). However, in $Cr^{2+}$ a low-energy shoulder is observed on the edge which arises from $1s \rightarrow 4s$ dipolar transitions (Fig. 40). Across the −6 to −10 $f_{O_2}$ range the Cr *K*-edge exhibits a pre-edge shoulder that decreases with increasing $f_{O_2}$ and shifts to lower energy with increasing temperature indicating a change in Cr oxidation state. These results indicate that there is a clear need for *in situ* high temperature studies of redox sensitive elements.
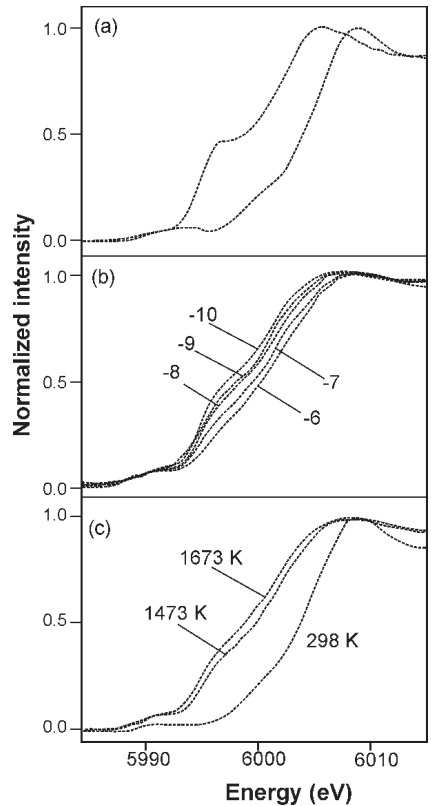


**Figure 40**. Cr *K*-edge measurements after Berry et al. (2003b). a) Iron-free diopside-anorthite glasses doped with $Cr^{2+}$ and $Cr^{3+}$. Note the prominent low energy shoulder on the edge of the $Cr^{2+}$ standard.

## The behavior of Br in CO$_2$-bearing fluids in low-temperature geological settings: A Br K-edge study on synthetic fluid inclusions

Evans et al. (2007) investigated the behavior of RbBr (Fig. 41) salts in CO$_2$-bearing fluid inclusions trapped in synthetic quartz. RbBr was used as an analogue of NaCl as the absorption edge of Br (13474 eV) is a hard X-ray range and thus may penetrate the quartz crystal whereas the absorption edges of Cl lies <3000 eV and is attenuated by the quartz matrix.

The CO$_2$-free fluid inclusion shows a prominent edge maximum at 13482 eV and a broad high-energy peak 13499 eV. As X$_{CO_2}$ increases the energy separation between the two peaks is reduced. This trend appears to be independent of temperature. In fluid inclusions with X$_{CO_2}$ between 0.02 - 0.2 the Br *K*-edge displays a prominent pre-edge, at ~13476.5 eV. Furthermore, with increasing temperature the pre-edge peak decreases in intensity and ultimately disappears above 423 K. Burattini et al. (1991) have assigned the pre-edge peaks in Br *K*-edge spectra to transitions between the 1*s* core level electrons to an unfilled bound *p* states. Covalently bonded Br exhibits an intense pre-edge feature (e.g., Burattini et al. 1991; Feiters et al. 2005) while
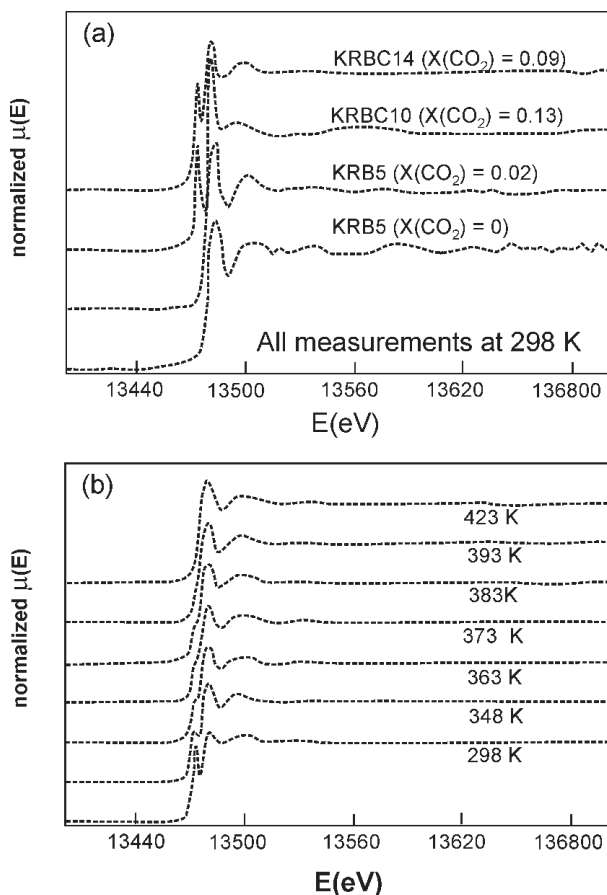


**Figure 41**. Br *K*-edge spectra of synthetic RbBr salt fluid inclusions in quartz crystals (after Evans et al. 2007). a) Br *K*-edge as a function of CO$_2$ content. Note the intense pre-edge peak at X$_{CO_2}$ = 0.09 and 0.13. b) Br *K*-edge as a function of temperature. Notice the decrease in pre-edge feature with increasing temperature. No pre-edge feature is seen at 423 K.

neither Br in electrolytic solution nor solid RbBr salt do. This implies that the Br in these fluid inclusions is covalently bonded. Burattini et al. (1991) also observe that the distance between the two main edge features decreases when the polarity of the solvent is low. In addition, Evans et al. (2007) have observed an increase in the intensity of the pre-edge peak with increasing $CO_2$ and its disappearance at high temperatures. These observations indicate that with increasing $CO_2$ content the RbBr-$CO_2$-$H_2O$ solution reacts to form covalently bonded C- and Br-bearing compounds or that $CO_2$ produces strongly polar molecules to form within the hydrothermal solution. Ultimately, Evans et al. (2007) conclude that the chemical bonding of Br in the presence of $CO_2$ is unexplained by current solution chemistry models, which has important implications for the role of halogens in solution.

## ACKNOWLEDGMENTS

## REFERENCES

Abbate M, Goedkoop JB, de Groot FMF, Grioni M, Fuggle JC, Hofmann S, Petersen H, Sacchi M (1992) Probing depth of soft X-ray absorption spectroscopy measured in total-electron-yield mode. Surf Interface Anal 18:65-69

Abbate M, Pen H, Czyzyk MT, Degroot FMF, Fuggle JC, Ma YJ, Chen CT, Sette F, Fujimori A, Ueda Y, Kosuge K (1993) Soft X-ray absorption-spectroscopy of vanadium-oxides. J Electron Spectrosc Relat Phenom 62:185-195

Achkar AJ, Regier TZ, Wadati H, Kim YJ, Zhang H, Hawthorn DG (2011) Bulk sensitive X-ray absorption spectroscopy free of self-absorption effects. Phys Rev B 83:081106

Alcacio TE, Hesterberg D, Chou JW, Martin JD, Beauchemin S, Sayers DE (2001) Molecular scale characteristics of Cu(II) bonding in goethite-humate complexes. Geochim Cosmochim Acta 65:1355-1366

Almkvist G, Boye K, Persson I (2010) *K*-edge XANES analysis of sulfur compounds:an investigation of the relative intensities using internal calibration. J Synchrotron Radiat 17:683-688

Alonso Mori R, Paris E, Giuli G, Eeckhout SG, Kavcic M, Zitnik M, Bucar K, Pettersson LGM, Glatzel P (2009) Electronic structure of sulfur studied by X-ray absorption and emission spectroscopy. Anal Chem 81:6516-6525

Alvarez M, Rueda EH, Sileo EE (2007) Simultaneous incorporation of Mn and Al in the goethite structure. Geochim Cosmochim Acta 71:1009-1020

Andrault D, Neuville DR, Flank AM, Wang Y (1998) Cation sites in Al-rich $MgSiO_3$ perovskites. Am Mineral 83:1045-1053

Arai Y, Sparks DL (2002) Residence time effects on arsenate surface speciation at the aluminum oxide-water interface. Soil Sci 167:303-314

Arrio MA, Rossano S, Brouder C, Galoisy L, Calas G (2000) Calculation of multipole transitions at the Fe *K*- pre-edge through p-d hybridization in the Ligand Field Multiplet model. Europhys Lett 51:454-460

Balzarotti AAF, Girlanda R, Martino G (1984) Electronic energy levels of α-$Al_2O_3$ from $L_3$ edge photoabsorption of aluminum and small cluster CNDO calculations. Phys Rev B 29:5903-5908

Beauchemin S, Hesterberg D, Chou J, Beauchemin M, Simard RR, Sayers DE (2003) Speciation of phosphorus in phosphorus-enriched agricultural soils using X-ray absorption near-edge structure spectroscopy and chemical fractionation. J Environ Qual 32:1809-1819

Beck P, De Andrade V, Orthous-Daunay FR, Veronesi G, Cotte M, Quirico E, Schmitt B (2012) The redox state of iron in the matrix of CI, CM and metamorphosed CM chondrites by XANES spectroscopy. Geochim Cosmochim Acta 99:305-316

Bender S, Franke R, Hartmann E, Lansmann V, Jansen M, Hormes J (2002) X-ray absorption and photoemission electron spectroscopic investigation of crystalline and amorphous barium silicates. J Non-Cryst Solids 298:99-108

Berry AJ, O''Neill HSC (2004) A XANES determination of the oxidation state of chromium in silicate glasses. Am Mineral 89:790-798

Berry AJ, O'Neill HS, Jayasuriya KD, Campbell SJ, Foran GJ (2003a) XANES calibrations for the oxidation state of iron in a silicate glass. Am Mineral 88:967-977

Berry AJ, Shelley JMG, Foran GJ, O'Neill HS, Scott DR (2003b) A furnace design for XANES spectroscopy of silicate melts under controlled oxygen fugacities and temperatures to 1773 K. J Synchrotron Radiat 10:332-336

Berry AJ, Hack AC, Mavrogenes JA, Newville M, Sutton SR (2006) A XANES study of Cu speciation in high-temperature brines using synthetic fluid inclusions. Am Mineral 91:1773-1782

Berry AJ, Yaxley GM, Woodland AB, Foran GJ (2010) A XANES calibration for determining the oxidation state of iron in mantle garnet. Chem Geol 278:31-37

Bianconi A (1979) Core excitons and inner well resonances in surface soft X-ray absorption (SSXA) spectra. Surf Sci 89:41-50

Blundy J, Wood B (1994) Prediction of crystal-melt partition-coefficients from elastic-moduli. Nature 372:452-454

Boese J, Osanna A, Jacobsen C, Kirz J (1997) Carbon edge XANES spectroscopy of amino acids and peptides. J Electron Spectrosc Relat Phenom 85:9-15

Borchert M, Wilke M, Schmidt C, Kvashnina K Jahn S (2013) Complexation of Sr in aqueous solutions equilibrated with silicate melts: implications for fluid-melt partitioning. Mineral Mag 77:739

Brandes JA, Cody GD, Rumble D, Haberstroh P, Wirick S, Gelinas Y (2008) Carbon *K*-edge XANES spectromicroscopy of natural graphite. Carbon 46:1424-1434

Brown GE Jr (1990) Spectroscopic studies of chemisorption reaction mechanisms at mineral/water interfaces. Rev in Mineral 23: 314-384

Brown GE Jr, Calas G, Waychunas GA, Petiau J (1988) X-ray absorption spectroscopy and its applications in mineralogy and geochemistry. Rev Mineral 18: 431-512

Brown GE Jr, Sturchio NC (2002) An overview of synchrotron radiation applications to low temperature geochemistry and environmental sciences. Rev in Mineral 49:1-115

Brown GE Jr, Parks GA (1989) Synchrotron-based X-ray absorption studies of cation environments in earth materials. Rev Geophys 27:519-533

Brice JC (1975) Some thermodynamic aspects of growth strained crystals. J Cryst Growth 28:249-253

Brigatti MF, Lugli C, Cibin G, Marcelli A, Giuli G, Paris E, Mottana A, Wu ZY (2000) Reduction and sorption of chromium by Fe(II)-bearing phyllosilicates: Chemical treatments and X-ray absorption spectroscopy (XAS) studies. Clay Clay Miner 48:272-281

Brigatti MF, Malferrari D, Poppi M, Mottana A, Cibin G, Marcelli A, Cinque G (2008) Interlayer potassium and its neighboring atoms in micas:Crystal-chemical modeling and XANES spectroscopy. Am Mineral 93:821-830

Brouder C, Cabaret D, Juhin A, Sainctavit P (2010) Effect of atomic vibrations on the X-ray absorption spectra at the K edge of Al in $\alpha$-$Al_2O_3$ and of Ti in $TiO_2$ rutile. Phys Rev B 81:115125

Brühwiler P, Maxwell A, Puglia C, Nilsson A, Andersson S, Mårtensson N (1995) $\pi^*$ and $\sigma^*$ excitons in C 1s absorption of graphite. Phys Rev Lett 74:614-617

Brydson R, Williams BG, Engel W, Sauer H, Zeitler E, Thomas JM (1987) Electron-energy Loss spectroscopy (EELS) and the electronic-structure of titanium dioxide. Solid State Commun 64:609-612

Brydson R, Vvedensky DD, Engel W, Sauer H, Williams BG, Zeitler E, Thomas JM (1988) Chemical information from Electron-loss Near-edge Structure - Core hole effects in the beryllium and boron *K*-edges in rhodizite. J Phys Chem 92:962-966

Brydson R, Sauer H, Engel W, Thomas JM, Zeitler E, Kosugi N, Kuroda H (1989) Electron-energy loss and X-ray absorption-spectroscopy of rutile and anatase - A test of structural sensitivity. J Phys-Condens Mat 1:797-812

Brydson R, Brown A, Benni LG, Livi K (2014) Analytical transmission electron microscopy. Rev Mineral Geochem 78:219-269

Burattini E, Dangelo P, Giglio E, Pavel NV (1991) EXAFS study of probe molecules in micellar solutions. J Phys Chem 95:7880-7886

Burke IT, Mayes WM, Peacock CL, Brown AP, Jarvis AP, Gruiz K (2012) Speciation of Arsenic, Chromium, and Vanadium in Red Mud Samples from the Ajka Spill Site, Hungary. Environ Sci Technol 46:3085-3092

Burnham AD, Berry AJ, Wood BJ, Cibin G (2012) The oxidation states of niobium and tantalum in mantle melts. Chem Geol 330:228-232

Cabaret D, Sainctavit P, Ildefonse P, Flank AM (1996) Full mutiple-scattering calculations on silicates and oxides at the Al *K*-edge. J Phys-Condens Mat 8:3691-3704

Cabaret D, Sainctavit P, Ildefonse P, Flank AM (1998) Full multiple scattering calculations of the X-ray absorption near edge structure at the magnesium K-edge in pyroxene. Am Mineral 83:300-304

Cabaret D, Joly Y, Renevier H, Natoli CR (1999) Pre-edge structure analysis of Ti *K*-edge polarized X-ray absorption spectra in $TiO_2$ by full-potential XANES calculations. J Synchrotron Radiat 6:258-260

Cabaret D, Le Grand M, Ramos A, Flank AM, Rossano S, Galoisy L, Calas G, Ghaleb D (2001) Medium range structure of borosilicate glasses from Si *K*-edge XANES:a combined approach based on multiple scattering and molecular dynamics calculations. J Non-Cryst Solids 289:1-8

Cabaret D, Mauri F, Henderson GS (2007) Oxygen-edge XANES of germanates investigated using first-principles calculations. Phys Rev B 75:184205

Cabaret D, Bordage A, Juhin A, Arfaoui M, Gaudry E (2010) First-principles calculations of X-ray absorption spectra at the *K*-edge of 3*d* transition metals:an electronic structure analysis of the pre-edge. Phys Chem Chem Phys 12:5619-33

Cabaret D, Emery N, Bellin C, Hérold C, Lagrange P, Wilhelm F, Rogalev A, Loupias G (2013) Nature of empty states in superconducting $CaC_6$ and related Li-Ca ternary graphite intercalation compounds using polarized X-ray absorption near-edge structure at the Ca *K*- edge. Phys Rev B 87:075108

Calas G, Petiau J (1983) Coordination of iron in oxide glasses through high-resolution *K*-edge spectra – Information from the pre-edge. Solid State Commun 48:625-629

Caliebe WA, Kao CC, Hastings JB, Taguchi M, Kotani A, Uozumi T, de Groot FMF (1998) 1*s*2*p* resonant inelastic X-ray scattering in $Fe_2O_3$. Phys.Rev B 58:13452-13458

Chalmin E, Farges F, Brown GB Jr (2009) A pre-edge analysis of Mn *K*-edge XANES spectra to help determine the speciation of manganese in minerals and glasses. Contrib Mineral Petrol 157:111-126

Chaplais G, Prouzet E, Flank AM, Le Bideau J (2001) $Al^{27}$ MAS NMR and XAS cross-study of the aluminophosphonate $Al(OH)(O_3PC_6H_5)$. New J Chem 25:1365-1367

Charnock J, Henderson CMB, Mosselmans J, Pattrick R (1996) 3*d* transition metal *L*-edge X-ray absorption studies of the dichalcogenides of Fe, Co and Ni. Phys Chem Minerals 23*:*403-408

Chen JG (1997) NEXAFS investigations of transition metal oxides, nitrides, carbides, sulfides and other interstitial compounds. Surf Sci Reports 30:1-152

Chen JM, Simonson JK, K.H. T, Rosenberg RA (1993a) Correlation between interatomic distances and teh X-ray absorption near-edge structure of singe-crystal sapphire. Phys Rev B 48:10047-10050

Chen JM, Rosenberg RA, Simons JK, Tan KH (1993b) X-ray absorption near-edge structure of single-crystal sapphire using synchrotron-radiation – The interatomic-distance correlation. Jpn J Appl Phys Part 1 32:788-790

Choy JH, Jung H, Yoon JB (2001) Co *K*-edge XAS study on a new cobalt-doped-$SiO_2$ pillared clay. J Synchrotron Radiat 8:599-601

Cibin G, Mottana A, Marcelli A, Brigatti MF (2005) Potassium coordination in trioctahedral micas investigated by *K*-edge XANES spectroscopy. Mineral Petrol 85:67-87

Cibin G, Mottana A, Marcelli A, Brigatti MF (2006) Angular dependence of potassium *K*-edge XANES spectra of trioctahedral micas: Significance for the determination of the local structure and electronic behavior of the interlayer site. Am Mineral 91:1150-1162

Cibin G, Mottana A, Marcelli A, Cinque G, Xu W, Wu Z, Brigatti MF (2010) The interlayer structure of trioctahedral lithian micas: An AXANES spectroscopy study at the potassium *K*-edge. Am Mineral 95:1084-1094

Coker VS, Pearce CI, Pattrick RAD, van der Laan G, Telling ND, Charnock JM, Arenholz E, Lloyd JR (2008) Probing the site occupancies of Co-, Ni-, and Mn-substituted biogenic magnetite using XAS and XMCD. Am Mineral 93:1119-1132

Cook NJ, Ciobanu CL, Brugger J, Etschmann B, Howard DL, de Jonge MD, Ryan C, and Paterson D (2012) Determination of the oxidation state of Cu in substituted Cu-In-Fe-bearing sphalerite via μXANES spectroscopy. Am Mineral 97:476-479

Cormier L, Neuville DR (2004) Ca and Na environments in $Na_2O$–CaO–$Al_2O_3$–$SiO_2$ glasses: influence of cation mixing and cation-network interactions. Chem Geol 213:103-113

Cormier L, Dargaud O, Menguy N, Henderson GS, Guignard M, Trcera N, Watts B (2011) Investigation of the Role of Nucleating Agents in MgO-$SiO_2$-$Al_2O_3$-SiO)-$TiO_2$ Glasses and Glass-Ceramics:A XANES Study at the Ti *K*- and $L_{2,3}$-Edges. Cryst Growth Des 11:311-319

Cottrell E, Kelley KA, Lanzirotti A, Fischer RA (2009) High-precision determination of iron oxidation state in silicate glasses using XANES. Chem Geol 268:167-179

Cressey G, Henderson C, van der Laan G (1993) Use of *L*-edge x-ray-absorption spectroscopy to characterize multiple valence states of 3*d* transition-metals - a new probe for mineralogical and geochemical research. Phys Chem Miner 20:111-119

Crocombette JP, Jollet F (1994) Ti 2*p* X-ray absorption in titanium dioxides. J Phys Condens Matter 6:10811-10821

Curti E, Dähn R, Farges F, Vespa M (2009) Na, Mg, Ni and Cs distribution and speciation after long-term alteration of a simulated nuclear waste glass: A micro-XAS/XRF/XRD and wet chemical study. Geochim Cosmochim Acta 73:2283-2298

Davoli I, Paris E, Stizza S, Benfatto M, Fanfoni M, Gargano A, Bianconi A, Seifert F (1992) Structure of densified vitreous silica – silicon and oxygen XANES spectra and multiple-scattering calculations. Phys Chem Miner 19:171-175

de Groot FMF (1993) X-ray-absorption of transition metal oxides – An overview of the theoretical approaches. J Electron Spectrosc Relat Phenom 62:111-130

de Groot FMF (1994) X-ray absorption and dichroism of transition metals their compounds. J Electron Spectrosc Relat Phenom 67:529-622

de Groot FMF (2001) High-resolution X-ray emission and X-ray absorption spectroscopy. Chem Rev 101:1779-1808

de Groot FMF (2005) Multiplet effects in X-ray spectroscopy. Coord Chem Rev 249:31-63

de Groot FMF (2008) Ligand and metal X-ray absorption in transition metal complexes. Inorg Chim Acta 361:850-856

de Groot FMF (2009) XANES spectra of transition metal compounds. *In*: 14th International Conference on X-Ray Absorption Fine Structure, 190. DiCicco A, Filipponi A (eds) Iop Publishing Ltd, Bristol, #012004

de Groot FMF (2012) Dips and peaks in fluorescence yield X-ray absorption are due to state-dependent decay. Nature Chem 4:766-767

de Groot FMF, Kotani A (2008) Core Level Spectroscopy of Solids. Taylor and Francis CRC press.

de Groot FMF, Grioni M, Fuggle JC, Ghijsen J, Sawatzky GA, Petersen H (1989) Oxygen 1*s* X-ray-absorption edges of transition metal oxides. Phys Rev B 40:5715-5723

de Groot FMF, Figueiredo MO, Basto MJ, Abbate M, Petersen H, Fuggle JC (1992) 2*p* X-ray absorption of titanium in minerals. Phys Chem Miner 19:140-147

de Groot FMF, Abbate M, Vanelp J, Sawatzky GA, Ma YJ, Chen CT, Sette F (1993) Oxygen-1*s* and cobalt-2*p* X-ray absorption of cobalt oxides. J Phys Cond Matt 5:2277-2288

de Groot FMF, Hu ZW, Lopez MF, Kaindl G, Guillot F, Tronc M (1994) Differences between L3 and L2 x-ray absorption spectra of transition metal compounds. J Chem Phys 101:6570-6576

de Ligny D, Neuville DR, Cormier L, Roux J, Henderson GS, Panczer G, Shoval S, Flank AM, Lagarde P (2009) Silica polymorphs, glass and melt: An *in situ* high temperature XAS study at the Si *K*-edge. J Non-Cryst Solids 355:1099-1102

de Smit E, Swart I, Creemer JF, Hoveling GH, Gilles MK, Tyliszczak T, Kooyman PJ, Zandbergen HW, Morin C, Weckhuysen BM, de Groot FMF (2008) Nanoscale chemical imaging of a working catalyst by scanning transmission X-ray microscopy. Nature 456:222-226

De Wispelaere S, Cabaret D, Levelut C, Rossano S, Flank AM, Parent P, Farges F (2004) Na-, Al- and Si *K*-edge XANES study of sodium silicate and sodium aluminosilicate glasses:influence of the glass surface. Chem Geol 213:63-70

DeBeer-George S, Brant P, Solomon EI (2005) Metal and ligand *K*-Edge XAS of organotitanium complexes: Metal 4*p* and 3*d* contributions to pre-edge intensity and their contributions to bonding. J Am Chem Soc 127:667-674

DeBeer-George S, Petrenko T, Neese F (2008) Prediction of iron *K*-edge absorption spectra using time-dependent density functional theory. J Phys Chem A 112:12936-12943

Dingwell DB, Paris E, Seifert F, Mottana A, Romano C (1994) X-ray-absorption study of Ti-bearing silicate-glasses. Phys Chem Miner 21:501-509

Doskocil EJ, Bordawekar SV, Davis RJ (1997) Alkali-support interactions on rubidium base catalysts determined by XANES, EXAFS, $CO_2$ adsorption, and IR spectroscopy. J Catal 169:327-337

Dyar MD, Breves EA, Emerson E, Bell SW, Nelms M, Ozanne MV, Peel SE, Carmosino ML, Tucker JM, Gunter ME, Delaney JS, Lanzirotti A, Woodland AB (2012) Accurate determination of ferric iron in garnets by bulk Mossbauer spectroscopy and synchrotron micro-XANES. Am Mineral 97:1726-1740

England KER, Charnock JM, Pattrick RAD, Vaughan DJ (1999) Surface oxidation studies of chalcopyrite and pyrite by glancing-angle X-ray absorption spectroscopy (REFLEXAFS). Mineral Mag 63:559-566

Espinosa A, Serrano A, Llavona A, Jimenez de la Morena J, Abuin M, Figuerola A, Pellegrino T, Fernández JF, Garcia-Hernandez M, Castro GR, Garcia MA (2012) On the discrimination between magnetite and maghemite by XANES measurements in fluorescence mode. Meas Sci Technol 23:015602

Essilfie-Dughan J, Hendry MJ, Warner J, Kotzer T (2012) Microscale mineralogical characterization of As, Fe, and Ni in uranium mine tailings. Geochim Cosmochim Acta 96:336-352

Evans KA, Mavrogenes J, Newville M (2007) The effect of $CO_2$ on the speciation of bromine in low-temperature geological solutions: an XANES study. J Synchrotron Radiat 14:219-26

Fandeur D, Juillot F, Morin G, Olivi L, Cognigni A, Webb SM, Ambrosi JP, Fritsch E, Guyot F, Brown Jr GE (2009) XANES evidence for oxidation of Cr(III) to Cr(VI) by Mn-oxides in a lateritic regolith developed on serpentinized ultramafic rocks of New Caledonia. Environ Sci Technol 43:7384-7390

Farges F (2001) Crystal chemistry of iron in natural grandidierites: an X-ray absorption fine-structure spectroscopy study. Phys Chem Miner 28: 619-629

Farges F (2005) Ab initio and experimental pre-edge investigations of the Mn *K*-edge XANES in oxide-type materials. Phys Rev B 71:155109

Farges F (2009) Chromium speciation in oxide-type compounds: application to minerals, gems, aqueous solutions and silicate glasses. Phys Chem Miner 36:463-481

Farges F, Brown GE Jr, Calas G, Galoisy L, Waychunas GA (1994) Structral transformation in Ni-bearing $Na_2Si_2O_5$ glass and melt. Geophys Res Lett 21:1931-1934

Farges F, Brown GE Jr, Rehr JJ (1996a) Coordination chemistry of Ti (IV) in silicate glasses and melts: I. XAFS study of titanium coordination in oxide model compounds. Geochim Cosmochim Acta 60:3013-3038

Farges F, Brown GE Jr, Navrotsky A, Gan H, Rehr JJ (1996b) Coordination chemistry of Ti(IV) in silicate glasses and melts: II. Glasses at ambient temperature and pressure. Geochim Cosmochim Acta 60:3039-3053

Farges F, Brown GE Jr, Rehr JJ (1997) Ti *K*-edge XANES studies of Ti coordination and disorder in oxide compounds:Comparison between theory and experiment. Phys Rev B 56:1809-1819

Farges F, Brown GE Jr, Petit PE, Munoz M (2001a) Transition elements in water-bearing silicate glasses/melts. Part I. A high-resolution and anharmonic analysis of Ni coordination environments in crystals, glasses, and melts. Geochim Cosmochim Acta 65:1665-1678

Farges F, Munoz M, Siewert R, Malavergne V, Brown GE, Behrens H, Nowak M, Petit ME (2001b) Transition elements in water-bearing silicate glasses/melts. Part II. Ni in water-bearing glasses. Geochim Cosmochim Acta 65:1679-1693

Farges F, Lefrère Y, Rossano S, Berthereau A, Calas G, Brown GE Jr (2004) The effect of redox state on the local structural environment of iron in silicate glasses: a combined XAFS spectroscopy, molecular dynamics, and bond valence study. J. Non-Cryst Solids 344: 176-188

Farquhar ML, Charnock JM, Livens FR, Vaughan DJ (2002) Mechanisms of arsenic uptake from aqueous solution by interaction with goethite, lepidocrocite, mackinawite, and pyrite: An X-ray absorption spectroscopy study. Environ Sci Technol 36:1757-1762

Farrell SP, Fleet ME (2001) Sulfur *K*-edge XANES study of loal electronic structure in ternary monosulfide solid solution [(Fe, Co, Ni)$_{0.923}$S]. Phys Chem Miner 28:17-27

Farrell SP, Fleet ME, Stekhin I, Kravtsova AN, Soldatov AV, Liu X (2002) Evolution of local electronic structure in alabandite and niningerite solid solutions Am Mineral 87:1321-1332

Feiters MC, Kupper FC, Meyer-Klaucke W (2005) X-ray absorption spectroscopic studies on model compounds for biological iodine and bromine. J Synchrotron Radiat 12:85-93

Finch AA, Allison N (2007) Coordination of Sr and Mg in calcite and aragonite. Mineral Mag 71:539-552

Finch AA, Allison N, Steaggles H, Wood CV, Mosselmans JFW (2010) Ba XAFS in Ba-rich standard minerals and the potential for determining Ba structural state in calcium carbonate. Chem Geol 270:179-185

Fister TT, Seidler GT, Rehr JJ, Kas JJ, Elam WT, Cross JO, Nagle KP (2007) Deconvolving instrumental and intrinsic broadening in core-shell X-ray spectroscopies. Phy Rev B 75: 174106

Fleet ME (2005) XANES spectroscopy of sulfur in Earth materials. Can Mineral 43:1811-1838

Fleet ME, Liu X (2001) Boron *K*-edge XANES of boron oxides: Tetrahedral B-O distances and near-surface alteration. Phys Chem Miner 28:421-427

Fleet ME, Muthupari S (1999) Coordination of Boron in alkail borosilicate glasses using XANES. J Non-Cryst Solids 255:233-241

Fleet ME, Muthupari S (2000) Boron *K*-edge XANES of borate and borosilicate minerals. Am Mineral 85:1009-1021

Fleet ME, Muthupari S, Kasrai M, Prabakar S (1997) Sixfold coordinated Si in alkali and alkali-CaO silicophosphate glasses by Si *K*-edge XANES spectroscopy. J Non-Cryst Solids 220:85-92

Fleet ME, Liu X, Harmer SL, King PL (2005) Sulfur *K*-edge XANES spectroscopy: Chemical state and content of sulfur in silicate glasses. Can Mineral 43:1603-1618

Fröba M, Wong J, Behrens P, Sieger P, Rowen M, Tanaka T, Rek Z, Felsche J (1995) Correlation of multiple-scattering features in XANES spectra of Al and Si *K*-edges to the Al-O-Si bond-angle in aluminosilicate sodalites – An emperical-study. Physica B 208:65-67

Frommer J, Nachtegaal M, Czekaj I, Weng TC, Kretzschmar R (2009) X-ray absorption and emission spectroscopy of Cr-III hydroxides: analysis of the *K*-pre-edge region. J Phys Chem A 113:12171-12178

Frommer J, Nachtegaal M, Czekaj I, Kretzschmar R (2010) The Cr X-ray absorption *K*-edge structure of poorly crystalline Fe(III)-Cr(III)-oxyhydroxides. Am Mineral 95:1202-1213

Fujikawa T, Okazawa T, Yamasaki K, Tang JC, Murata T, Matsukawa T, Naoe SI (1989) Full multiple-scattering approach to Na *K*-edge XANES of NaCl-KCl mixed crystal. J Phys Soc Japan 58:2952-2961

Fussa-Rydel O, Dye JL, Teo BK (1988) Rubidium X-ray-absorption (EXAFS and XANES) studies of Rb- and complexed Rb$^+$ in alkalides and electrides. J Am Chem Soc 110:2445-2451

Galoisy L, Calas G (1993) Structural environment of nickel in silicate glass melts systems. 1. Sepctroscopic determination of coordination states. Geochim Cosmochim Acta 57:3613-3626

Galoisy L, Calas G, Arrio MA (2001) High-resolution XANES spectra of iron in minerals and glasses:Structural information from the pre-edge region. Chem Geol 174:307-319

Gao SP (2010) Ab initio calculation of ELNES/XANES of BeO polymorphs. Phys Status Solidi B 247:2190-2194

Garvie LAJ, Buseck PR (1996) Parallel electron energy-loss spectroscopy of boron in minerals. Rev Mineral 33:821-843

Garvie LAJ, Buseck PR (1999) Bonding in silicates: Investigations of the Si $L_{2,3}$ edge by parallel electron energy-loss spectroscopy. Am Mineral 84:946-964

Garvie LAJ, Craven AJ, Brydson R (1994) Use of electron-energy-loss near-edge fine-structure in the study of minerals. Am Mineral 79:411-425

Garvie LAJ, Craven AJ, Brydson R (1995) Parallel elecrton energy-loss spectroscopy (PEELS) study of B in minerals: The electron energy-loss near-edge structure (ELNES) of the B $K$-edge. Am Mineral 80:1132-1144

Garvie LAJ, Rez P, Alvarez JR, Buseck PR, Craven AJ, Brydson R (2000) Bonding in alpha-quartz ($SiO_2$): A view of the unoccupied states. Am Mineral 85:732-738

Gaudry E, Cabaret D, Brouder C, Letard I, Rogalev A, Wilhlem F, Jaouen N, Sainctavit P (2007) Relaxations around the substitutional chromium site in emerald: X-ray absorption experiments and density functional calculations. Phys Rev B 76:094110

Gilbert B, Frazer BH, Naab F, Fournelle J, Valley JW, De Stasio G (2003) X-ray absorption spectroscopy of silicates for in situ, sub-micrometer mineral identification. Am Mineral 88:763-769

Giuli G, Paris E, Wu ZY, Berrettoni M, Della Ventura G, Mottana A (2000) Nickel site distribution and clustering in synthetic double-chain silicates by experimental and theoretical XANES spectroscopy. Phys Rev B 62:5473-5477

Giuli G, Paris E, Mungall J, Romano C, Dingwell D (2004) V oxidation state and coordination number in silicate glasses by XAS. Am Mineral 89:1640-1646

Glatzel P, Bergmann U (2005) High resolution 1s core hole X-ray spectroscopy in 3d transition metal complexes. Coord Chem Rev 249:65-95

Glatzel P, Mirone A, Eeckhout SG, Sikora M, Giuli G (2008) Orbital hybridization and spin polarization in the resonant 1s photoexcitations of $Fe_2O_3$. Phys Rev B 77:115133

Gonzalez-Jimenez ID, Cats K, Davidian T, Ruitenbeek M, Meirer F, Liu Y, Nelson J, Andrews JC, Pianetta P, de Groot FMF, Weckhuysen BM (2012) Hard X-ray nanotomography of catalytic solids at work. Angew Chem 51:11986-11990

Greegor RB, Lytle FW, Sandstrom DR, Wong J, Schultz P (1983) Investigation of $TiO_2$-$SiO_2$ glasses by X-ray absorption-spectroscopy. J Non-Cryst Solids 55:27-43

Greegor RB, Pingitore NE, Lytle FW (1997) Strontianite in coral skeletal aragonite. Science 275:1452-1454

Grunes LA (1983) Study of the $K$-edges of 3d Transition-metals in pure and oxide form by X-ray-absorption spectroscopy. Phys Rev B 27:2111-2131

Hallmeier KH, Szargan R, Meisel A, Hartmann E, Gluskin ES (1981) Investigation of core-excited quantum yield spectra of highly symmetric boron compounds. Spectrochim Acta A 37:1049-1053

Hamalainen K, Siddons DP, Hastings JB, Berman LE (1991) Elimination of the inner-shell lifetime broadening in X-ray absorption spectroscopy. Phys Rev Lett 67:2850-2853

Handa K, Kojima K, Taniguchi K, Ozutsumi K, Ikeda S (2005) Studies on the Extremely Soft X-ray absorption spectrometry at BL2. Memoires of the SR Center Ritsumeikan University 7:3-6

Handa K, Ide J, Nishiyama Y, Ozutsumi K, Dalba G, Ohtori N, Umesaki N (2006) XAS study of barium borate glasses and crystals. Phys Chem Glasses-B 47:445-447

Hansen PL, Brydson R, McComb DW, Richardson I (1994) EELS fingerprint of Al-coordination in silicates. Microsc Microanal Microstruct 5:173-182

Harp GR, Han ZL, Tonner BP (1990) X-ray-absorption near-edge structures in intermediate oxidation-states of silicon in silicon-oxides during thermal-desorption. J Vac Sci Technol A 8:2566-2569

Hawthorne FC (ed) (1988) Spectroscopic Methods in Mineralogy and Geochemistry. Volume 18. Reviews in Mineralogy. Mineralogical Society of America, Washington

Hawthorne FC, Waychunas GA (1988) Spectrum fitting methods. Rev Mineral 18:63-98

Hawthorne FC, Burns PC, Grice JD (1996) The crystal chemistry of boron. Rev Mineral 33:41-115

Hedman B, Hodgson KO, Solomon EI (1990) X-ray absorption edge spectroscopy of ligands bound to open-shell metal ions. J Am Chem Soc 112:1643-1645

Henderson CMB, Foland KA (1996) Ba- and Ti-rich primary biotite from the Brome alkaline igneous complex, Monteregion Hills, Quebec: mechansims of substitution. Can Mineral 34: 1241-1252.

Henderson GS (1995) A Si $K$-edge EXAFS/XANES study of sodium-silicate glasses. J Non-Cryst Solids 183:43-50

Henderson GS (2007) The germanate anomaly:What do we know? J Non-Cryst Solids 353:1695-1704

Henderson GS, Fleet ME (1997) The structure of titanium silicate glasses investigated by Si $K$-edge X-ray absorption spectroscopy. J Non-Cryst Solids 211:214-221

Henderson GS, St-Amour JC (2004) A Si $K$-edge XANES study of Ti containing alkali/alkaline-earth silicate glasses. Chem Geol 213:31-40

Henderson GS, Liu X, Fleet ME (2003) Titanium coordination in silicate glasses investigated using O *K*-edge X-ray absorption spectroscopy. Mineral Mag 67:597-607

Henderson GS, Neuville DR, Cormier L (2007) An O K-edge study of calcium aluminates. Can J Chem 85:801-805

Henderson GS, Neuville DR, Cormier L (2009) An O *K*-edge XANES study of glasses and crystals in the CaO-$Al_2O_3$-$SiO_2$ (CAS) system. Chem Geol 259:54-62

Hitchcock AP, Newbury DC, Ishii I, Stohr J, Horsley JA, Redwing RD, Johnson AL, Sette F (1986) Carbon *K*-shell excitation of gaseous and condensed cyclic hydrocarbons - $C_3H_6$, $C_4H_8$, $C_5H_8$, $C_5H_{10}$, $C_6H_10$, $C_6H_{12}$, AND $C_8H_8$. J Chem Phys 85:4849-4862

Höche T, Mäder M, Bhattacharya S, Henderson GS, Gemming T, Wuth R, Rüssel C, Avramov I (2011) $ZrTiO_4$ crystallization in nanosized liquid-liquid phase-seperation droplets in glass-a quantitative XANES study. CrystEngComm 13:2550-2556.

Höche T, Ikeno H, Mäder M, Henderson GS, Blyth RIR, Sales BC, Tanaka I (2013) Vanadium $L_{2,3}$ XANES experiments and first-principles multielectron calculations: Impact of second-nearest neighboring cations on vanadium-bearing fresnoites. Am Mineral 98:663-670

Hu YF, Xu RK, Dynes JJ, Blyth RIR, Yu G, Kozak LM, Huang PM (2008) Coordination nature of aluminum (oxy)hydroxides formed under the influence of tannic acid studied by X-ray absorption spectroscopy. Geochim Cosmochim Acta 72:1959-1969

Hudson E, Moler E, Zheng Y, Kellar S, Heimann P, Hussain Z, Shirley D (1994) Near-edge sodium and fluorine *K*-shell photoabsorption of alkali halides. Phys Rev B 49:3701-3708

Ildefonse P, Kirkpatrick RJ, Montez B, Calas G, Flank AM, Lagarde P (1994) $Al^{27}$ MAS NMR and aluminum X-ray-absorption near-edge structure study of imogolite and allophanes. Clay Clay Miner 42:276-287

Ildefonse P, Calas G, Flank AM, Lagarde P (1995) Low Z-elements (Mg, Al, and Si) *K*-edge X-ray-absorption spectroscopy in minerals and disordered-systems. Nucl Instrum Methods Physics B 97:172-175

Ildefonse P, Cabaret D, Sainctavit P, Calas G, Flank AM, Lagarde P (1998) Aluminium X-ray absorption near edge structure in model compounds and Earth's surface minerals. Phys Chem Miner 25:112-121

Ingall ED, Brandes JA, Diaz JM, de Jonge MD, Paterson D, McNulty I, Elliott WC, Northrup P (2011) Phosphorus *K*-edge XANES spectroscopy of mineral standards. J Synchrotron Radiat 18:189-197

Ishiguro E, Iwata S, Suzuki Y, Mikuni A, Sasaki T (1982) Boron *K* photoabsorption spectra of $BF_3$, $BCl_3$, and $BBr_3$. J Phys B 15:1841-1854

Iwamoto S, Iwamoto S, Inoue M, Yoshida H, Tanaka T, Kagawa K (2005) XANES and XPS study of silica-modified titanias prepared by the glycothermal method. Chem Mater 17:650-655

Jahn S, Kowalski PM (2014) Theoretical approaches to structure and spectroscopy of earth materials. Rev Mineral Geochem 78:691-743

Jiang N (2002) on detection of non-bridging oxygen in glasses by electron-energy-loss spectroscopy. Solid State Commun 122:7-10

Jiang N (2006) Structure and composition dependence of oxygen K edge in $CaAl_2O_4$. J Appl Phys 100:013703

Jiang N, Spence J (2004) Core-hole effects on electron energy-loss spectroscopy of $Li_2O$. Phys Rev B 69:115112

Jiang N, Spence JCH (2006) Interpretation of oxygen K pre-edge peak in complex oxides. Ultramicroscopy 106:215-219

Jiang N, Su D, Spence J (2007) Determination of Ti coordination from pre-edge peaks in Ti *K*-edge XANES. Phys Rev B 76:214117

Jokic A, Cutler JN, Ponomarenko E, van der Kamp G, Anderson DW (2003) Organic carbon and sulfur compounds in wetland soils:Insights on structure and transformation processes using *K*-edge XANES and NMR spectroscopy. Geochim Cosmochim Acta 67:2585-2597

Jugo PJ, Wilke M, Botcharnikov RE (2010) Sulfur *K*-edge XANES analysis of natural and synthetic basaltic glasses:Implications for S speciation and S content as function of oxygen fugacity. Geochim Cosmochim Acta 74:5926-5938

Juhin A, Calas G, Cabaret D, Galoisy L, Hazemann JL (2008) Structural relaxation around substitutional $Cr^{3+}$ in pyrope garnet. Am Mineral 93:800-805

Kar G, Hundal LS, Schoenau JJ, Peak D (2011) Direct chemical speciation of P in sequential chemical extraction residues using P *K*-Edge X-Ray absorption near-edge structure spectroscopy. Soil Science 176:589-595

Kasrai M, Fleet ME, Sham TK, Bancroft GM, Tan KH, Brown JR (1988) A XANES study of the S *L*-edge in sulfide minerals:Application to interatomic distance determination. Solid State Commun 68:507-511

Kasrai M, Fleet M, Bancroft G, Tan K, Chen J (1991) X-ray-absorption near-edge structure of alkali halides:The interatomic-distance correlation. Phys Rev B 43:1763-1772

Kasrai M, Yin Z, Bancroft GM, Tan KH (1993) X-ray fluorescence measurements of X-ray absorption near edge structure at the Si, P, and S *L* edges. J Vac Sci Technol A 11:2694-2699

Kasrai M, Brown JR, Bancroft GM, Yin Z, Tan KH (1996a) Sulfur characterization in coal from X-ray absorption near edge spectroscopy. Int J Coal Geol 32:107-135

Kasrai M, Lennard WN, Brunner RW, Bancroft GM, Bardwell JA, Tan KH (1996b) Sampling depth of total electron and fluorescence measurments in Si *L*- and *K*-edge absorption spectroscopy. Appl Surf Sci 99:303-312

Kasrai, M, Fleet ME, Muthupari S, Li D, Bancroft GM (1998) Surface modification study of borate materials from B K-edge X-ray absorption spectroscopy. Phys Chem Miner 25:268-272

Kasrai M, Vasiga M, Fuller MS, Bancroft GM, Fyfe K (1999) Study of the effects of Ca sulfonate on antiwear film formation by X-ray absorption spectroscopy using synchrotron radiation. J Synchrotron Radiat 6:719-721

Kasrai M, Suominen Fuller M, Bancroft GM (2003) X-ray absorption study of the effect of calcium sulfonate on antiwear film formation generated from neutral and basic ZDDPS: Part 1-Phosphorous species. Tribology Trans 46:534-542

Kaznacheyev K, Osanna A, Jacobsen C, Plashkevych O, Vahtras O, Agren H, Carravetta V, Hitchcock AP (2002) Innershell absorption Spectroscopy of amino acids. J Phys Chem A 106:3153-3168

Khare N, Hesterberg D, Martin JD (2005) XANES investigation of phosphate sorption in single and binary systems of iron and aluminum oxide minerals. Environ Sci Technol 39:2152-2160

Kikas A, Nommiste E, Ruus R, Saar A, Martinson I (2001) Core excitons in Na *K* photoabsorption of NaF: Resonant Auger spectroscopy. Phys Rev B 64:235120

King PL, Sham TK, Gordon RA, Dyar MD (2013) Microbeam X-ray analysis of $Ce^{3+}/Ce^{4+}$ in Ti-rich minerals: A case study with titanite (sphene) with implications for multivalent trace element substitution in minerals. Am Mineral 98:110-119

Klimm K, Kohn SC, O'Dell LA, Botcharnikov RE, Smith ME (2012) The dissolution mechanism of sulfur in hydrous silicate melts. I: Assessment of analytical techniques in determining the sulfur speciation in iron-free to iron-poor glasses. Chem Geol 322-323:237-249

Kobayashi H, Emura S, Arachi Y, Tatsumi K (2007) Investigation of inorganic compounds on the surface of cathode materials using Li and O *K*-edge XANES. J Power Sources 174:774-778

Kohn SC, Charnock JM, Henderson CMB, Greaves GN (1990) The structural environments of trace elements in dry and hydrous silicate glasses: a manganese and strontium K-edge X-ray absorption spectroscopy study. Contrib Mineral Petrol 105:359-368

Krause MO, Oliver JH (1979) Natural widths of atomic *K* and *L* levels, *K*-alpha X-ray lines and several KLL Auger lines. J Phys Chem Ref Data 8:329-338

Kruse J, Leinweber P, Eckhardt KU, Godlinski F, Hu Y, Zuin L (2009) Phosphorus $L_{2,3}$-edge XANES: Overview of reference compounds. J Synchrotron Radiat 16:247-259

Lavrentyev AA, Gabrelian BV, Nikiforov IY, Rehr JJ (1999) Ab initio XANES calculations for KCl and PbS. J Phys Chem Solids 60:787-790

Lawrence JR, Dynes JJ, Korber DR, Swerhone GDW, Leppard GG, Hitchcock AP (2012) Monitoring the fate of copper nanoparticles in river biofilms using scanning transmission X-ray microscopy (STXM). Chem Geol 329:18-25

Lee DK, Eng PJ, Mao H-K (2014) Probing of pressure-induced bonding transitions in crystalline and amorphous earth materials: insights from X-ray Raman scattering at high pressure. Rev Mineral Geochem 78:139-174

Levelut C, Cabaret D, Benoit M, Jund P, Flank AM (2001) Multiple scattering calculations of the XANES Si *K*-edge in amorphous silica. J Non-Cryst Solids 293:100-104

Li D, Bancroft GM, Kasrai M, Fleet ME, Feng XH, Tan KH, Yang BX (1993) High-resolution Si *K*-edge and $L_{2,3}$-edge XANES of alpha quartz and stishovite. Solid State Commun 87:613-617

Li D, Bancroft GM, Kasrai M, Fleet ME, Secco RA, Feng XH, Tan KH, Yang BX (1994) X-ray-absorption spectroscopy of silicon dioxide ($SiO_2$) polymorphs – The structural characterization of opal. Am Mineral 79:622-632

Li D, Bancroft GM, Fleet ME, Feng XH (1995a) Silicon *K*-edge XANES spectra of silicate minerals. Phys Chem Minerals 22:115-122

Li D, Secco RA, Bancroft GM, Fleet ME (1995b) Pressure-induced coordination change of Al in silicate melts from the Al *K*-edge XANES of high-pressure $NaAlSi_2O_6$, $NaAlSi_3O_8$ glasses. Geophys Res Lett 22:3111-3114

Li D, Bancroft GM, Fleet ME, Hess PC, Yin ZF (1995c) Coordination of B in $K_2O$-$SiO_2$-$B_2O_3$-$P_2O_5$ glasses using B *K*-edge XANES. Am Mineral 80:873-877

Li D, Bancroft GM, Kasrai M (1995d) S *K*- and *L*-edge X-ray absorption spectroscopy of sulfides and sulfates: Applications in mineralogy and geochemistry. Can Mineral 33:949-960

Li D, Bancroft GM, Fleet ME (1996) B *K*-edge XANES of crystalline and amorphous inorganic materials. J Electron Spectrosc Relat Phenom 79:71-73

Li D, Peng MS, Murata T (1999) Coordination and local structure of magnesium in silicate minerals and glasses: Mg *K*-edge XANES study. Can Mineral 37:199-206

Lu Y-C, Kwabi DG, Yao KPC, Harding JR, Zhou J, Zuin L, Shao-Horn Y (2011) The discharge rate capability of rechargeable Li–O$_2$ batteries. Energy Environ Sci 4:2999-3007

Luca V, Djajanti S, Howe RF (1998) Structural and electronic properties of sol-gel titanium oxides studied by X-ray absorption spectroscopy. J Phys Chem B 102:10650-10657

Ma Y, Wassdahl N, Skytt P, Guo J, Nordgren J, Johnson P, Rubensson JE, Boske T, Eberhardt W, Kevan S (1992) Soft-X-ray resonant inelastic scattering at the C *K*-edge of diamond. Phys Rev Lett 69:2598-2601

Ma Y, Skytt P, Wassdahl N, Glans P, Guo J, Nordgren J (1993) Core excitons and vibronic coupling in diamond and graphite. Phys Rev Lett 71:3725-3728

Magnien V, Neuville DR, Cormier L, Roux J, Hazemann JL, de Ligny D, Pascarelli S, Vickridge I, Pinet O, Richet P (2008) Kinetics and mechanisms of iron redox reactions in silicate melts:The effects of temperature and alkali cations. Geochim Cosmochim Acta 72:2157-2168

Manceau A, Gorshkov AI, Drits VA (1992) Structural chemistry of Mn, Fe, Co and Ni in manganese hydrous oxides. 1. Information from XANES spectroscopy. Am Mineral 77:1133-1143

Manceau A, Marcu MA, Tamura N (2002) Qunatitative speciation of heavy metals in soils and sediments by synchrotron X-ray techniques. Rev Mineral Geochem 49: 341-428

Manceau A, Marcus MA, Grangeon S (2012) Determination of Mn valence states in mixed-valent manganates by XANES spectroscopy. Am Mineral 97:816-827

Manuel D, Cabaret D, Brouder C, Sainctavit P, Bordage A, Trcera N (2012) Experimental evidence of thermal fluctuations on the X-ray absorption near-edge structure at the aluminum K edge. Phys Rev B 85:224108

Marcelli A, Cibin G, Cinque G, Mottana A, Brigatti MF (2006) Polarized XANES spectroscopy:The *K* edge of layered K-rich silicates. Radiat Phys Chem 75:1596-1607

Mauchamp V, Boucher F, Ouvrard G, Moreau P (2006) Ab initio simulation of the electron energy-loss near-edge structures at the Li K edge in Li, Li$_2$O, and LiMn$_2$O$_4$. Phys Rev B 74:115106

Mauchamp V, Moreau P, Ouvrard G, Boucher F (2008) Local field effects at Li *K*-edges in electron energy-loss spectra of Li, Li$_2$O and LiF. Phys Rev B 77:045117

Mavrogenes JA, Berry AJ, Newville M, Sutton SR (2002) Copper speciation in vapor-phase fluid inclusions from the Mole Granite, Australia. Am Mineral 87:1360-1364

McComb DW, Hansen PL, Brydson R (1991) A study of silicon ELNES in nesosilicates. Microscopy Microanalysis Microstructures 2:561-568

McKeown DA (1989) Aluminum X-ray-absorption near-edge spectra of oxide minerals – Calculation versus experimental-data. Phys Chem Miner 16:678-683

McKeown DA, Waychunas GA, Brown GE Jr (1985) EXAFS and XANES study of the local coordination environment of sodium in a series of silica-rich glasses and selected minerals within the Na$_2$O-Al$_2$O$_3$-SiO$_2$ system. J Non-Cryst Solids 74:323-348

Mele EJ, Ritsko JJ (1979) Fermi-level lowering and the core exciton spectrum of intercalated graphite. Phys Rev Lett 43:68-71

Miedema PS, Ngene P, van der Eerden AMJ, Weng TC, Nordlund D, Sokaras D, Alonso-Mori R, Juhin A, de Jongh PE, de Groot FMF (2012) In situ X-ray Raman spectroscopy of LiBH$_4$. Phys Chem Chem Phys 14:5581-5587

Miedema PS, de Groot FMF (2013) The iron *L* edges: Fe 2*p* X-ray absorption and electron energy loss spectroscopy, J Electron Spectrosc Relat Phenom 187:32-48

Miehé-Brendlé J, Tuilier MH, Marichal C, Gallego JC, Reinholdt M (2010) Mg environments in the octahedral sheet of 2:1 talc-like hybrid phyllosilicates: A comparative XAFS study. Euro J Inorg Chem 35:5587-5591

Mizoguchi T, Tatsumi K, Tanaka I (2006) Peak assignments of ELNES and XANES using overlap population diagrams. Ultramicroscopy 106:1120-1128

Mizokawa T, Tjeng L, Lin H, Chen C, Kitawak, R, Terasaki I, Lambert S, Michel C (2005) X-ray absorption study of layered Co oxides with a Co-O triangular lattice. Phys Rev B 71:193107

Mo SD, Ching WY (2001) X-ray absorption near-edge structure in alpha-quartz and stishovite:Ab initio calculation with core-hole interaction. Appl Phys Lett 78:3809-3811

Morar JF, Himpsel FJ, Hollinger G, Hughes G, Jordan JL (1985) Observation of a C-1s core exciton in diamond. Phys Rev Lett 54:1960-1963

Mottana A (2004) X-ray absorption spectroscopy in mineralogy: Theory and experiment in the XANES region. EMU Notes Mineral 6:465-552

Mottana A, Murata T, Wu ZY, Marcelli A, Paris E (1997) The local structure of Ca-Na pyroxenes .1. XANES study at the Na *K*-edge. Phys Chem Miner 24:500-509

Mottana A, Murata T, Marcelli A, Wu ZY, Cibin G, Paris E, Giuli G (1999) The local structure of Ca-Na pyroxenes. II. XANES studies at the Mg and Al *K*-edges. Phys Chem Miner 27:20-33

Murata T, Matsukawa T, Naoe S (1988) XANES and EXAFS studies on *K*-shell absorption in $K_{1-x}Na_xCl$solid solutions. Solid State Commun 66:787-790

Nabavi M, Taulelle F, Sanchez C, Verdaguer M (1990) XANES V-51 NMR-study of vanadium oxygen compounds. J Phys Chem Solids 51:1375-1382

Nesbitt HW, Bancroft GM (2014) High resolution core- and valence-level XPS studies of the properties (structural, chemical and bonding) of silicate minerals and glasses. Rev Mineral Geochem 78:271-329

Neuville DR, Cormier L, Flank A-M, Briois V, Massiot D (2004a) Al speciation and Ca environment in calcium aluminosilicate glasses and crystals by Al and Ca *K*-edge X-ray absorption spectroscopy. Chem Geol 213:153-163

Neuville DR, Cormier L, Flank A-M, Prado RJ, Lagarde P (2004b) Na *K*-edge XANES spectra of minerals and glasses. Eur J Mineral 16:809-816

Neuville DR, de Ligny D, Cormier L, Henderson GS, Roux J, Flank A-M, Lagarde P (2009) The crystal and melt structure of spinel and alumina at high temperature: An in-situ XANES study at the Al and Mg *K*-edge. Geochim Cosmochim Acta 73:3410-3422

Neuville DR, Henderson GS, Cormier L, Massiot D (2010) The structure of crystals, glasses, and melts along the $CaO-Al_2O_3$ join: Results from Raman, Al *L*- and *K*-edge X-ray absorption, and $^{27}Al$ NMR spectroscopy. Am Mineral 95:1580-1589

Nicholls M, Najman MN, Zhang Z, Kasrai M, Norton PR, Gilbert P (2007) The contribution of XANES spectroscopy to tribology. Can J Chem 85:816-830

Nicholls MA, Norton PR, Bancroft GM, Kasrai M (2004) X-ray absorption spectroscopy of tribofilms produced from zinc dialkyl dithiophosphates on Al–Si alloys. Wear 257:311-328

Odake S, Fukura S, Arakawa M, Ohta A, Harte B, Kagi H (2008) Divalent chromium in ferropericlase inclusions in lower-mantle diamonds revealed by micro-XANES measurements. J Mineral Petrol Sci 103:350-353

Okada K, Uozumi T, Kotani A (1994) Split-off formation in the final state of photoemission of Ti compounds. J Phys Soc Japan 63:3176-3184

Okude N, Nagoshi M, Noro H, Baba Y, Yamamoto H, Sasaki TA (1999) P and S *K*-edge XANES of transition-metal phosphates and sulfates. J Electron Spectrosc Relat Phenom101:607-610

Ollier N, Lombard P, Farges F, Boizot B (2008) Titanium reduction processes in oxide glasses under electronic irradiation. J Non-Cryst Solids 354:480-485

Olovsson W, Tanaka I, Mizoguchi T, Puschnig P, Ambrosch-Draxl C (2009a) All-electron Bethe-Salpeter calculations for shallow-core X-ray absorption near-edge structures. Phys Rev B 79:041102(R)

Olovsson W, Tanaka I, Puschnig P, Ambrosch-Draxl C (2009b) Near-edge structures from first principles all-electron Bethe-Salpeter equation calculations. J Phys-Condens Mat 21:104205

Outka DA, Stöhr J (1988) Curve fitting analysis of near-edge core excitation spectra of free, adsorbed, and polymeric molecules. J Chem Phys 88:3539-3554

Paris E, Mottana A, Della Ventura G, Robert JL (1993) Titanium valence and coordination in synthetic richterite – Ti-richterite amphiboles – A synchrotron-radiation XAS study. Eur J Mineral 5:455-464

Paris E, Wu ZY, Mottana A, Marcelli A (1995) Calcium environment in omphacitic pyroxenes – XANES experimental-data versus one-electron multiple-scattering calculations. Eur J Mineral 7:1065-1070

Parkman RH, Charnock JM, Livens FR, Vaughan DJ (1998) A study of the interaction of strontium ions in aqueous solution with the surfaces of calcite and kaolinite. Geochim Cosmochim Acta 62:1481-1492

Pattrick RAD, Mosselmans JFW, Charnock JM (1998) An X-ray absorption study of doped sphalerites. Eur J Mineral 10:239-249

Pattrick RAD, van der Laan G, Henderson CMB (2002) Cation site occupancy in spinel ferrites studied by X-ray magnetic circular dichroism: developing a method for mineralogists. Eur J Miner 14:1095-1102

Pattrick RAD, Coker VS, Pearce CI, Telling ND, van der Laan G (2008) The oxidation state of copper and cobalt in carrolite, $CuCo_2S_4$. Can Mineral 46:1317-1322

Pearce CI, Henderson CMB, Pattrick RAD, van der Laan G, Vaughn DJ (2006) Direct determination of cation site occupancies in natural ferrite spinels by $L_2$, $L_3$ X-ray absorption spectroscopic and X-ray magnetic circular dichroism. Am Mineral 91:880-893.

Petit PE, Farges F, Wilke M, Sole VA (2001) Determination of the iron oxidation state in Earth materials using XANES pre-edge information. J Synchrotron Radiat 8:952-954

Peuget S, Broudic V, Jégou C, Frugier P, Roudil D, Deschanels X, Rabiller H, Noel PY (2007) Effect of alpha radiation on the leaching behaviour of nuclear glass. J Nucl Materials 362:474-479

Peuget S, Cachia JN, Jégou C, Deschanels X, Roudil D, Broudic V, Delaye JM, Bart JM (2006) Irradiation stability of R7T7-type borosilicate glass. J Nucl Materials 354:1-13

Pingitore NE, Lytle FW, Davies BM, Eastman MP, Eller PG, Larson EM (1992) Mode of incorporation of $Sr^{2+}$ in calcite – Determination by X-ray-absorption-spectroscopy. Geochim Cosmochim Acta 56:1531-1538.

Poe B, Romano C, Henderson GS (2004) Raman and XANES spectroscopy of permanently densified vitreous silica. J Non-Cryst Solids 341: 162-169

Poe B, Seifert F, Sharp T, Wu Z (1997) ELNES spectroscopy of mixed Si coordination minerals. Phys Chem Miner 24:477-487

Poumellec B, Cortes R, Tourillon G, Berthon J (1991a) Angular-dependence of the Ti *K*-edge in rutile $TiO_2$. Phys Status Solidi B 164:319-326

Poumellec B, Durham PJ, Guo GY (1991b) Electronic-structure and X-ray-absorption-spectrum of rutile $TiO_2$. J Phys-Condens Mat 3:8195-8204

Povahzynaja NA, Shvejtzer IG, Soldatov AV (1995) Electronic structure of $SmFeO_3$ –X-ray absorption fine-structure analysis. J Phys-Condens Mat 7:4975-4981

Prado RJ, Flank AM (2005) Sodium K edge XANES calculation in 'NaCl' type structures. Phys Scripta T115:165-167

Prietzel J, Thieme J, Paterson D (2010) Phosphorus speciation of forest-soil organic surface layers using P *K*-edge XANES spectroscopy. J Plant Nutr Soil Sci 173:805-807

Quartieri S, Chaboy J, Merli M, Oberti R, Ungaretti L (1995) Local structural environment of calium in garnets – A combined structure-refinement and XANES investigation. Phys Chem Miner 22:159-169

Rehr JJ, Ankudinov A (2005) Progress in the theory and interpretation of XANES. Coord Chem Rev 249:131-140

Reinke P, Knop-Gericke A, Havecker M, Schedel-Niedrig T (2000) Interaction of diamond with water: An in situ XANES investigation. Surf Sci 447:229-236

Riedler M, de Castro ARB, Kolmakov A, Lofken JO, Nowak C, Soldatov AV, Wark A, Yalovega G, Moller T (2001a) Na 1s photoabsorption of free and deposited NaCl clusters: Development of bond length with cluster size. Phys Rev B 64:245419

Riedler M, de Castro ARB, Kolmakov A, Löfken JO, Nowak C, Soldatov AV, Wark A, Yalovega G, Möller T (2001b) Photoabsorption of NaCl clusters at the Na *K*-edge: Development of the bond length with the cluster size. J Chem Phys 115:1319-1323

Rivard C, Montarges-Pelletier E, Vantelon D, Pelletier M, Karunakaran C, Michot LJ, Villieras F, Michau N (2013) Combination of multi-scale and multi-edge X-ray spectroscopy for investigating the products obtained from the interaction between kaolinite and metallic iron in anoxic conditions at 90 °C. Phys Chem Miner 40:115-132

Romano C, Paris E, Poe BT, Giuli G, Dingwell DB, Mottana A (2000) Effect of aluminum on Ti-coordination in silicate glasses: A XANES study. Am Mineral 85:108-117

Rosenberg RA, Love PJ, Rehn V (1986) Polarization-dependent C(K) near-edge X-ray-absorption fine structure of graphite. Phys Rev B 33:4034-4037

Rossetti I, Sordelli L, Ghigna P, Pin S, Scavini M, Forni L (2011) EXAFS-XANES Evidence of in Situ Cesium Reduction in Cs-Ru/C Catalysts for Ammonia Synthesis. Inorg Chem 50:3757-3765

Ruus R, Kikas A, Saar A, Ausmees A, Nommiste E, Aarik J, Aidla A, Uustare T, Martinson I (1997) Ti 2*p* and O 1s X-ray absorption of $TiO_2$ polymorphs. Solid State Commun 104:199-203

Sarret G, Connan J, Kasrai M, Bancroft G, Charrie-Duhaut A, Lemoine S, Adam P, Albrecht P, Eybert-Berard L (1999) Chemical forms of sulfur in geological and archealogical asphaltenes from Middle East, France and Spain determined by sulfur *K* and *L*-edge X-ray absorption near-edge structure spectroscopy. Geochim Cosmochim Acta 63:3767-3779

Sarret G, Mongenot T, Connan J, Derenne S, Kasrai M, Bancroft GM, Largeau C (2002) Sulfur speciation in kerogens of the Orbagnoux deposit (Upper Kimmeridgian, Jura) by XANES spectroscopy and pyrolysis. Org Geochem 33:877-895

Sauer H, Brydson R, Rowley PN, Engel W, Thomas JM (1993) Determination of coordinations and coordination-specific site occupancies by electron energy-loss spectroscopy: An investigation of boron-oxygen compounds. Ultramicroscopy 49:198-209

Schroeder SLM, Moggridge GD, Chabala E, Ormerod RM, Rayment T, Lambert RM (1996) In situ studies of catalysts under reaction conditions by total electron-yield. Farad Disc 105:317-336

Schulman RG, Yafet Y, Eisenberger E, Blumberg WE (1976) Observation and interpretation of X-ray absorption edges in iron compounds and proteins. Proc Natl Acad Sci USA 73:1384-1388

Schwarz WHE, Mensching L, Hallmeier KH, Szargan R (1983) *K* shell excitations of $BF_3$, $CF_4$ and $MBF_4$. Chem Phys 82:57-65

Sharp T, Wu Z, Seifert F, Poe B, Doerr M, Paris E (1996) Distinction between six- and fourfold coordinated silicon in $SiO_2$ polymorphs via electron loss near edge structure (ELNES) spectroscopy. Phys Chem Miner 23:17-24

Shaw SA, Peak D, Hendry MJ (2009) Investigation of acidic dissolution of mixed clays between pH 1.0 and 3.0 using Si and Al X-ray absorption near edge structure. Geochim Cosmochim Acta 73:4151-4165

Shirley EL (2004) Ti ls pre-edge features in rutile: A Bethe-Salpeter calculation. J Electron Spectrosc Relat Phenom 136:77-83

Shukla A, Calandra M, Taguchi M, Kotani A, Vanko G, Cheong SW (2006) Polarized resonant inelastic X-ray scattering as an ultrafine probe of excited states of $La_2CuO_4$. Phys Rev Lett 96:0770006

Simon SB, Sutton SR, Grossman L (2007) Valence of titanium and vanadium in pyroxene in refractory inclusion interiors and rims. Geochim Cosmochim Acta 71:3098-3118

Sipr O, Rocca F (2010) Electronic structure effects on B *K*-edge XANES of minerals. J Synchrotron Radiat 17:367-373

Sipr O, Simunek A, Rocca F (2007) B *K*-edge XANES of superstructural units in borate glasses. AIP conference proceedings 882:446-448

Skytt P, Glans P, Mancini D, Guo JH, Wassdahl N, Nordgren J, Ma Y (1994) Angle-resolved soft-X-ray fluorescence and absorption study of graphite. Phys Rev B 50:10457-10461

Soininen JA, Hamalainen K, Caliebe WA, Kao CC, Shirley EL (2001) Core-hole-electron interaction in X-ray Raman scattering. J Phys-Condens Mat 13:8039-8047

Soldatov AV, Gusatinskii AN (1984) Energy delocalization of the rare-earth F-states in some compounds. Phys Status Solidi B 125:K129-K132

Soldatov AV, Ivanchenko TS, Dellalonga S, Kotani A, Iwamoto Y, Bianconi A (1994) Crystal-structure effects in the Ce $L_3$-edge X-ray-absorption spectrum of $CeO_2$ – Mutiple scattering resonances and many-body final-states. Phys Rev B 50:5074-5080

Soldatov AV, Stekhin IE, Ingalls R (1996) Electronic structure of RbBr during the phase transition: X-ray absorption near-edge structure analysis. J Phys-Condens Mat 8:7829-7835

Soldatov AV, Kasrai M, Bancroft GM (2000) unoccupied electronic states of stishovite: X-ray absorption fine structure theoretical analysis. Solid State Commun 115:687-692

Soldatov AV, Kravtsova AN, Fleet ME, Harmer SL (2004) Electronic structure of MeS (Me = Ni,Co,Fe):X-ray absorption analysis. J Phys-Condens Mat 16:7545-7556

Solomon D, Lehmann J, Harden J, Wang J, Kinyangi J, Heymann K, Karunakaran C, Lu Y, Wirick S, Jacobsen C (2012) Micro- and nano-environments of carbon sequestration:Multi-element STXM–NEXAFS spectromicroscopy assessment of microbial carbon and mineral associations. Chem Geol 329:53-73

Solomon D, Lehmann J, Kinyangi J, Liang BQ, Schafer T (2005) Carbon *K*-edge NEXAFS and FTIR-ATR spectroscopic investigation of organic carbon speciation in soils. Soil Sci Soc Am J 69:107-119

Sowrey FE, Skipper LJ, Pickup DM, Drake KO, Lin Z, Smith ME, Newport RJ (2004) Systematic empirical analysis of calcium-oxygen coordination environment by calcium *K*-edge XANES. Phys Chem Chem Phys 6:188

Stavitski E, de Groot FMF (2010) The CTM4XAS program for EELS and XAS spectral shape analysis of transition metal L edges. Micron 41:687-694

Stepanyuk VS, Szasz A, Farberovich OV, Grigorenko AA, Kozlov AV, Mikhailin VV (1989) An electronic band structure calculation and the optical properties of alkaline-earth sulphides. Phys Status Solidi B 155:215-220

Stöhr J (1992) NEXAFS Spectroscopy. Springer Verlag, Berlin

Suljoti E, de Groot FMF, Nagasono M, Glatzel P, Hennies F, Deppe M, Pietzsch A, Sonntag B, Föhlisch A, Wurth W (2009) Spin-orbit mediated interference in the radiative and nonradiative channels of the La 4d core resonances. Phys Rev Lett 103:137401

Sutton SR, Dyar MD, Delaney JS, Newville M, Rossman GR (2000) Interpretation of Fe *K* XANES Pre-edge spectra of hematite based on cobalt optical spectra. APS Activity report 2000

Sutton SR, Karner J, Papike J, Delaney JS, Shearer C, Newville M, Eng P, Rivers M, Dyar MD (2005) Vanadium *K* edge XANES of synthetic and natural basaltic glasses and application to microscale oxygen barometry. Geochim Cosmochim Acta 69:2333-2348

Taillefumier M, Cabaret D, Flank AM, Mauri F (2002) X-ray absorption near-edge structure calculations with the pseudopotentials: Application to the *K*-edge in diamond and alpha-quartz. Phys Rev B 66:195107

Teodorescu CM, Esteva JM, Womes M, El Afif A, Karnatak RC, Flank AM, Lagarde P (2000) Sodium 1s photoabsorption spectra of Na and NaF clusters deposited in rare gas matrices. J Electron Spectrosc Relat Phenom 106:233-245

Terminello LJ, Shuh DK, Himpsel FJ, Lapianosmith DA, Stohr J, Bethune DS, Meijer G (1991) Unfilled orbitals of C-60 and C-70 from carbon *K*-shell X-ray-absorption fine-structure. Chem Phys Lett 182:491-496

Thole BT, van der Laan G (1988) Branching ratio in X-ray absorption spectroscopy. Phys Rev B 38:3158-3171

Thole BT, van der Laan G, Butler PH (1988) Spin-mixed ground state of Fe Phthalocyanine and the temperature dependent branching ratio in X-ray absorption spectroscopy. Chem Phys Lett 149:295-299

Thompson AC, Vaughan D (2011) X-ray data booklet. Lawrence Berkeley National Laboratory, University of California, Berkeley, CA 94720

Tossell JA (1977) SCF–Xα scattered wave MO studies of the electronic structure of ferrous iron in octahedral coordination with sulfur. J Chem Phys 66:5712

Trcera N, Cabaret D, Rossano S, Farges F, Flank AM, Lagarde P (2009) Experimental and theoretical study of the structural environment of magnesium in minerals and silicate glasses using X-ray absorption near-edge structure. Phys Chem Miner 36:241-257

Trcera N, Rossano S, Madjer K, Cabaret D (2011) Contribution of molecular dynamics simulations and ab initio calculations to the interpretation of Mg *K*-edge experimental XANES in $K_2O$-MgO-3SiO$_2$ glass. J Phys-Condens Mat 23:255401

Tsuji J, Nakamatsu H, Mukoyama T, Kojima K, Ikeda S, Taniguchi K (2002) Lithium *K*-edge XANES spectra for lithium compounds. X-Ray Spectrom 31:319-326

Uozumi T, Okada K, Kotani A, Durmeyer O, Kappler JP, Beaurepaire E, Parlebas JC (1992) Experimental and theoretical investigation of the pre-peaks at the Ti *K*-edge absorption-spectra in $TiO_2$. Europhys Lett 18:85-90

Urquhart SG, Ade H (2002) Trends in the carbonyl core (C 1s, O 1s) → pi*c=o transition in the near-edge X-ray absorption fine structure spectra of organic molecules. J Phys Chem B 106:8531-8538

van Aken PA, Liebscher B (2002), Quantification of ferrous/ferric ratios in minerals. Phys Chem Miner 29:188-200

van Aken PA, Sharp TG, Seifert F (1998) Electron-beam induced amorphization of stishovite:Silicon-coordination change observed using Si *K*-edge extended electron energy-loss fine structure. Phys Chem Miner 25:83-93

van Bockhoven JA, Nabi T, Sambe, Remaker DE, Koningsberger DC (2001) Interpretation of the Al *K*- and $L_{II/III}$-edges of aluminum oxides:differences between tetrahedral and octahedral Al explained by different local symmetries. J Phys-Condens Mat 13:10247-10260

van Bokhoven JA, Sambe H, Ramaker DE, Koningsberger DC (1999) Al *K*-edge near-edge X-ray absorption fine structure (NEXAPS) study on the coordination structure of aluminum in minerals and Y zeolites. J Phys Chem B 103:7557-7564

van Bokhoven JA, van der Eerden AMJ, Koningsberger DC (2003) Three-coordinate aluminum in zeolites observed with in situ X-ray absorption near-edge spectroscopy at the Al *K*-edge: Flexibility of aluminum coordinations in zeolites. J Am Chem Soc 125:7435-7442

Van Elp J, Wieland J, Eskes H, Kuiper P, Sawatzky G, de Groot FMF, Turner T (1991) Electronic-Structure of CoO, Li-Doped CoO, and LiCoO$_2$. Phys Rev B 44:6090-6103

Vankó G, de Groot FMF, Huotari S, Cava RJ, Lorenz T, Reuther M (2008) Intersite 4*p*-3*d* hybridization in cobalt oxides: A resonant X-ray emission spectroscopy study. arXiv:0802.2744

Varlot K, Kasrai M, Bancroft GM, Yamaguchi ES, Ryason PR, Igarashi J (2001) X-ray absorption study of antiwear films generated from ZDDP and borate micelles. Wear 249:1029-1035

Villain O, Calas G, Galoisy L, Cormier L (2007) XANES determination of chromium oxidation states in glasses: Comparison with optical absorption spectroscopy. J Am Ceram Soc 90:3578-3581

Vinson J, Rehr JJ, Kas JJ, Shirley EL (2011) Bethe-Salpeter equation calculations of core excitation spectra. Phys Rev B 83:115106

von Barth U, Grossmann G (1982) Dynamical effects in X-ray spectra and the final-state rule. Phys Rev B 25:5150-5179

Wang HM, Henderson GS (2004) Investigation of coordination number in silicate and germanate glasses using O *K*-edge X-ray absorption spectroscopy. Chem Geol 213:17-30

Wasinger EC, de Groot FMF, Hedman B, Hodgson KO, Solomon EI (2003) *L*-edge X-ray absorption spectroscopy of non-heme iron sites. J Am Chem Soc 125:12894-12906

Waychunas GA (1987) Synchrotron Radiation XANES spectroscopy of Ti in minerals: Effects of Ti bonding distances, Ti valence, and site geometry on adsorption edge structure. Am Mineral 72:89-101

Waychunas GA, Apted MJ, Brown GE Jr (1983) X-ray *K*-edge absorption spectra of Fe minerals and model compounds: Near-edge structure. Phys Chem Miner 10:1-9

Waychunas GA, Fuller CC, Davis JA, Rehr JJ (2003) Surface complexation and precipitate geometry for aqueous Zn(II) sorption on ferrihydrite:II. XANES analysis and simulation. Geochim Cosmochim Acta 67:1031-1043

Weigel C, Calas G, Cormier L, Galoisy L, Henderson GS (2008) High-resolution Al $L_{2,3}$-edge X-ray absorption near edge structure spectra of Al-containing crystals and glasses: Coordination number and bonding information from edge components. J Phys-Condens Mat 20:135219

Westre TE, Kennepohl P, DeWitt JG, Hedman B, Hodgson KO, Solomon EI (1997) A multiplet analysis of Fe *K*-edge 1s → 3*d* pre-edge features of iron complexes. J Am Chem Soc 119:6297-6314

Wilke M, Farges F, Petit PE, Brown GE Jr, Martin F (2001) Oxidation state and coordination of Fe in minerals: An Fe *K*-XANES spectroscopic study. Am Mineral 86:714-730

Wilke M, Partzsch GM, Bernhardt R, Lattard D (2004) Determination of the iron oxidationstate in basaltic glasses using XANES at the K-edge. Chem Geol 213: 71-87

Wilke M, Partzsch GM, Bernhardt R, and Lattard D (2005) Determination of the iron oxidation state in basaltic glasses using XANES at the *K*-edge. Chem Geol 213:71-87

Wilke M, Schmidt C, Farges F, Malavergne V, Gautron L, Simionovici A, Hahn M, Petit P (2006) Structural environment of iron in hydrous aluminosilicate glass and melt-evidence from X-ray absorption spectroscopy. Chem Geol 229:144-161

Wilke M, Farges F, Partzsch GM, Schmidt C, Behrens H (2007) Speciation of Fe in silicate glasses and melts by in-situ XANES spectroscopy. Am Mineral 92:44-56

Wilke M, Jugo PJ, Klimm K, Susini J, Botcharnikov R, Kohn SC, Janousch M (2008) The origin of $S^{4+}$ detected in silicate glasses by XANES. Am Mineral 93:235-240

Wilke M, Hahn O, Woodland AB, Rickers K (2009) The oxidation state of iron determined by Fe K-edge XANES-application to iron gall ink in historical manuscripts. J. Anal At Spectrom 24:1364-1372

Wilke M, Klimm K, Kohn SC (2011) Spectroscopic Studies on Sulfur Speciation in Synthetic and Natural Glasses. Rev Mineral Geochem 73:41-78

Wong J, Lytle FW, Messmer RP, Maylotte DH (1984) K-edge absorption spectra of selected vanadium compounds. Phys Rev B 30:5596-5610

Wu Z, Mottana A, Marcelli A, Natoli CR, Paris E (1996) Theoretical analysis of X-ray absorption near-edge structure in forsterite, $Mg_2SiO_4$-Pbnm, and fayalite, $Fe_2SiO_4$-Pbnm, at room temperature and extreme conditions. Phys Chem Mineral 23:193-204

Wu Z, Marcelli A, Mottana A, Giuli G, Paris E (1997a) Al coordination and local structure in minerals: XAFS determinations and multiple-scattering calculations for K-feldspars. Europhys Lett 38:465-470

Wu ZY, Ouvrard G, Gressier P, Natoli CR (1997b) Ti and O *K* edges for titanium oxides by multiple scattering calculations: Comparison to XAS and EELS spectra. Phys Rev B 55:10382-10391

Wu ZY, Jollet F, Seifert F (1998) Electronic structure analysis of α-$SiO_2$ via X-ray absorption near-edge structure at the Si *K*, $L_{2,3}$ and O *K*-edges. J Phys-Condens Mat 10:8083-8092

Wu Z, Paris E, Langenhorst F, Seifert F. (2002) Oxygen-metal bonding in Ti-bearing compounds from O 1s spectra and ab initio full mutiple scattering calculations. J Synchrotron Radiat 9:394-400

Xiong W, Peng J, Hu Y (2012) Use of X-ray absorption near edge structure (XANES) to identify physisorption and chemisorption of phosphate onto ferrihydrite-modified diatomite. J Colloid Interf Sci 368:528-32

Xu RK, Hu YF, Dynes JJ, Zhao AZ, Blyth RIR, Kozak LM, Huang PM (2010) Coordination nature of aluminum (oxy)hydroxides formed under the influence of low molecular weight organic acids and a soil humic acid studied by X-ray absorption spectroscopy. Geochim Cosmochim Acta 74:6422-6435

Xu W, Chen DL, Chu WS, Wu ZY, Marcelli A, Mottana A, Soldatov A, Brigatti MF (2011) Quantitative local structure determination in mica crystals: ab initio simulations of polarization XANES at the potassium *K*-edge. J Synchrotron Radiat 18:418-426

Xu W, Liu L, Cui M, Zheng L, Hu Y, Marcelli A, Wu Z (2013) Electronic structure and hybridization of CaS by means of X-ray absorption spectroscopy at Ca and S *K*-edges. J Synchrotron Radiat 20:110-115

Yamamoto T, Tanaka T, Suzuki S, Kuma R, Teramura K, Kou Y, Funabiki T, Yoshida S (2002) NO reduction with CO in the presence of $O_2$ over $Cu/Al_2O_3$. Top Catal 18:113-118

Yarker CA, Johnson PAV, Wright AC, Wong J, Greegor RB, Lytle FW, Sinclair RN (1986) Neutron-diffraction and EXAFS evidence for $TiO_5$ units in vitreous $K_2O$-$TiO_2$-$2SiO_2$. J Non-Cryst Solids 79:117-136

Yin ZF, Kasrai M, Bancroft GM, Tan KH, Feng XH (1995) X-ray-absorption spectroscopic studies of sodium polyphosphate glasses. Phys Rev B 51:742-750

Yoshiya M, Tanaka I, Kaneko K, Adachi H (1999) First principles calculations of chemical shifts in ELNES/NEXAFS of titanium oxides. J Phys-Condens Mat 11:3217-3228

Zhang GY, Hu YF, Xu RK, Dynes JJ, Blyth RIR, Huang PM (2009) Carbonate induced structural perturbation of Al hydroxides. Clay Clay Miner 57:795-807

Zhang JY, Xiao ZR, Kuo JL (2010) Calculation of near *K*-edge X-ray absorption spectra and hydrogen bond network in ice XIII under compression. J Chem Phys 132:184506